IMPERIAL COLLEGE LONDON

DEPARTMENT OF PHYSICS

PHOTONICS GROUP

Development of power-scaled tunable Alexandrite lasers

Goronwy Tawy

Thesis submitted in partial fulfilment of the requirements for the degree of Doctor of Philosophy of Imperial College London

April 2021

I declare that the work presented in this thesis is my own. All the information that has been derived from others has been cited at every instance. The full list of the references is provided at the end of this thesis.

Copyright Declaration

Acknowledgements

Firstly I would like to thank my supervisor Prof. Mike Damzen whose guidance and insight has made my PhD possible. I am incredibly grateful for the regular support on an almost daily-basis and will always be thankful for a supervisor that provided the perfect balance of work and rest even if it meant having to attend several karaoke sessions!

I would also like to thank the other members of the group whose paths have crossed with mine and have been kind, welcoming, helpful and most importantly very friendly be it in the lab, on a tea break or at a conference thousands of miles from home. I'd like to thank Ara for his wide-ranging technical abilities in the lab (especially for all his clever little optomechanical inventions!) and always being up for a debate over tea. Will for his seemingly endless insight into all things Alexandrite and more, and for keeping things laid-back when Mike tried to get those project meetings going again. Wim for all the joyful conversations and as an excellent housemate in San Francisco. Xin for helping me get started with the PhD and for introducing karaoke with food. Juna for her brief but friendly appearance in our group, and finally Gabs for introducing me to lasers in the first place way back in 2015. I would like to acknowledge Dr Juna Sathian and Dr Xin Sheng for their co-operation in working on the Alexandrite ring lasers in Chapter 7 which provided an excellent introduction into my PhD.

Within Photonics I am grateful for everyone who have made my work easier such as Simon and Martin for their ability to continue churning out very useful and well made components for the lab in addition to being there to talk about all things running, cycling and swimming. My thanks to Marcia and Judith who have always been on hand to sort all things admin and for a guaranteed friendly chat. To all members of FOG who have made the joint Journal Club a great get-together and for always being there for a friendly chat in the level 2 corridor. For Anita who has

been a great friend, great squash player and fellow revolutionary - despite all the work getting in the way in the end!

A quick thank you also to the Imperial Greats: Jake, Joe and Sophie, as well as the Portland Massive: Alex, Fran, Kieran, Ro ad Tom. You have all kept me smiling over the last year in your own crazy unique way.

To my wife Mayya I am incredibly grateful of the endless love and support over the duration of the PhD. Thanks for putting up with my endless monologues on lasers and for providing the longest proofread that I could ever ask. When revisiting this thesis I will always be reminded of the days we spent together in lockdown London as I wrote this thesis and how I could not have asked for a better companion to share those times with.

Hoffwn hefyd diolch fy nheulu am eu cefnogaeth dros y tair blynedd a hanner diwethaf. Diolch i Gwenllian a Gerallt am yr hwyl a'r chwerthin. Fi wedi mwynhau trio fy nghorau i ateb cwestiynau Gerallt am greu pob math o laser enfawr a chwyno gyda Gwenllian am y problemau yn y byd academaidd. Mae wedi bod yn flwyddyn anodd i ni gyd yn enwedig gan fod ni methu cwrdd lan yn aml. Hoffwn roi fy niolch olaf i mamgu. Does neb arall wedi rhoi cymaint o hwyl mewn i fywyd, ac ohoni hi rydw i wedi dysgu i neud fy nghorau i fwynhau'r ddoethuriaeth yma ac i fwynhau bywyd pob dydd.

Abstract

Alexandrite is a highly attractive laser source in the near-infrared owing to its broad wavelength coverage of around 700-820 nm and strong thermo-mechanical properties. This makes it a suitable laser source for a number of applications including remote sensing, biophotonics and quantum technologies.

Over the last ten years there has been considerable progress in the development of red-diode-pumped Alexandrite lasers, however there remained to be a demonstration of multi-watt Alexandrite lasers with wavelength tuning in fundamental TEM_{00} transverse and single-longitudinal-mode (SLM) operation. The aim of this work is therefore to develop power-scaled Alexandrite lasers with wavelength tuning which will bring it closer to applications outside the laser laboratory.

A novel wavelength-tunable and dual wavelength Alexandrite laser is presented with a continuous wavelength tuning range of 747-768 nm using the crystal as both the gain medium and wavelength tuning element.

For accurate laser cavity design a detailed study of pump-induced lensing in Alexandrite lasers is performed. This includes the development of an analytical theoretical model and direct wavefront measurement under both non-lasing and lasing conditions. New insight into pump-induced lensing in Alexandrite is gained and a combined thermal and population lens postulated.

Utilising this improved understanding, a record power of 8.6 W is demonstrated in diffraction-limited TEM_{00} mode. >1 W over 730-805 nm and >4 W over 755-780 nm narrow-linewidth wavelength tuning is achieved for the very first time from a red-diode-pumped Alexandrite laser. This power is higher than any other directly-diode-pumped vibronic laser in the 700-820 nm region.

SLM operation is demonstrated in two compact ring laser cavities with up to 1 W of output power. Power scaled ring lasers up to the 5 W-level are also presented showing promising signs for >1 W wavelength tunable SLM performance.

Publications

Journal Papers

G. Tawy, A. Minassian and M. J. Damzen, "High-power 7.4W TEM_{00} and wavelength tunable Alexandrite laser with novel cavity design and efficient fibre-coupled diode-pumping," OSA Continuum **3**, 1638-1649 (2020).

G. Tawy, J. Wang and M.J. Damzen, "Pump-induced lensing effects in diode pumped Alexandrite lasers," Opt. Express **27**, 35865-35883 (2019).

G. Tawy and M.J. Damzen, "Tunable, dual wavelength and self-Q-switched Alexandrite laser using crystal birefringence control," Opt. Express **27**, 17507-17520 (2019).

J. Sathian, **G. Tawy**, X. Sheng, A. Minassian and M. J. Damzen, "Non-Astigmatic Alexandrite Ring Laser Design with Wavelength-tunable Single-Longitudinal Mode operation" J. Opt. Soc. Am. B **37**, 2185-2192 (2020).

X. Sheng, **G. Tawy**, J. Sathian, A. Minassian and M.J. Damzen, "Unidirectional single-frequency operation of a continuous-wave Alexandrite ring laser with wavelength tunability," Opt. Express **26**, 31129-31136 (2018).

U. Parali, X. Sheng, A. Minassian, **G. Tawy**, J. Sathian, G.M. Thomas and M.J. Damzen, "Diode-pumped Alexandrite laser with passive SESAM Q-switching and wavelength tunability," Opt. Communications **410** 970-976 (2018).

Conference Presentations

G. Tawy, A. Minassian and M. J. Damzen, "Fibre-delivered red-diode-pumped >7 W TEM_{00} Alexandrite laser," 2020 International Conference Laser Optics pp. 1-1.

G. Tawy, A. Minassian and M. J. Damzen, "High-power, wavelength-tunable red-diode-pumped Alexandrite laser ," in 9th EPS-QEOD Europhoton Conference, We-A3.2 (2020).

G. Tawy, J. Wang and M.J. Damzen, "Thermal and population induced lensing in Alexandrite lasers," Proc. SPIE 11266, Solid State Lasers XXIX: Technology and Devices, 1126616 (2020)

G. Tawy and M.J. Damzen, "Ultra-compact >100 kHz Q-switched Alexandrite lasers," Proc. SPIE 11259, Solid State Lasers XXIX: Technology and Devices, 112590Q (2020)

G. Tawy and M.J. Damzen, "Narrow linewidth tunable and dual wavelength compact Alexandrite laser," Proc. SPIE 11259, Solid State Lasers XXIX: Technology and Devices, 112590J (2020)

J. Sathian, **G. Tawy**, X. Sheng, A. Minassian and M.J. Damzen "Compact Non-Astigmatic Alexandrite Ring Laser with Unidirectional Single-Longitudinal-Mode operation," in 2019 Conference on Lasers and Electro-Optics Europe and European Quantum Electronics Conference, OSA Technical Digest (Optical Society of America, 2019), paper ca_1_3.

Conference Posters

G. Tawy, J. Wang and M.J. Damzen "Population Lensing in Alexandrite Lasers," in 2019 Conference on Lasers and Electro-Optics Europe and European Quantum Electronics Conference, OSA Technical Digest (Optical Society of America, 2019), paper ca_p_11.

G. Tawy and M.J. Damzen "Tunable and Dual Wavelength Alexandrite Laser Using the Crystal Birefringence," in 2019 Conference on Lasers and Electro-Optics Europe and European Quantum Electronics Conference, OSA Technical Digest (Optical Society of America, 2019), paper ca_p_10.

X. Sheng, **G. Tawy**, J. Sathian, A. Minassin and M.J. Damzen, "Unidirectional single-frequency operation of a wavelength-tunable red-diode-pumped Alexandrite ring laser," In: 8th EPS-QEOD Europhoton Conference: Solid State, Fibre, and Waveguide Coherent Light Sources (2018).

Contents

List of Figures

List of Tables

Chapter 1

Introduction

1.1 Background

A laser (light amplification by stimulated emission radiation) is a device that generates a coherent and directional source of electro-magnetic radiation. May 2020 marked the sixtieth anniversary of the laser [1] and in that time it has enabled a wide range of applications such as optical communication, optical trapping, atomic cooling, super-resolution microscopy and gravitational wave detection, as well many others that have led to lasting changes in science, industry and society [2].

A laser is formed of a gain medium, a resonant optical cavity and a source of energy, referred to as the pump. Figure 1.1 shows a diagram of both the very first laser and its modern day counterpart. Though they are configured differently both operate on the same principle. The gain medium, which in both cases is a Ruby (Chromium-doped sapphire) crystal, amplifies radiation through the process of stimulated emission. Placing the gain medium inside the resonant optical cavity provides the feedback. Energy is supplied to the gain medium using a pump source which can be in the form of electrical, chemical or optical energy. Maiman's Ruby laser was pumped by a broadband flashlamp that was helically twisted around the outer surface of the Ruby and placed in a reflecting aluminium cylinder. The Ruby absorbed broadly at the ultra-violet, blue and green wavelengths and emitted monochromatically in the deep red at 694 nm in short bursts. Today's Ruby laser is pumped by a blue laser-diode (LD), which is tightly focused onto the Ruby crystal. This diode-pumped solid-state system provides a significant improvement in optical efficiency, simplicity and robustness.

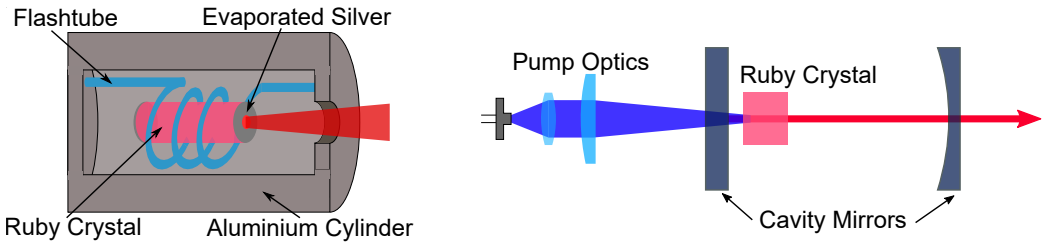

Figure 1.1: (a) Maiman's flashlamp pumped Ruby laser - the first optical laser. Image adapted from [3]. (b) Blue-diode-pumped Ruby - realising highly efficient continuous-wave operation sixty years after the first Ruby laser. Image adapted from [4].

The Ruby lasers of 1960 and 2020 illustrate how the underlying principles of laser operation has not changed and in fact a number of laser techniques used widely in research today were initially developed during the 1960s. These include pulsed operation methods such as Q-switching and mode-locking, second harmonic generation and parametric amplification [5]. The type of laser gain medium had also diversified with gas, liquid dye and semiconductor diodes also enabling laser operation.

The following decades witnessed the wide-spread commercialisation of laser systems which today has a global market value of around $16.6 billion. Today, lasers span all wavelengths from the UV to the mid-infrared, have timescales down to the attosecond, and output powers at beyond the kW-level [6]. At the forefront of laser development today are grand-challenges such as space-borne laser interferometers for gravitational-wave detection [7], laser x-ray sources [8] and laser development for the plethora of applications in the THz region [9]. While commercially available lasers cover almost every wavelength from the UV to the mid-infrared, they are not necessarily the ideal source for a given application. Often, sacrifices in efficiency, overall size, cost and even performance have to be made. Significant attention in laser research is therefore also aimed at improving the performance of lasers, particularly in developing easily transportable systems that take lasers outside of the laboratory and into real-world implementation.

1.2 Thesis Motivation and Overview

The development in blue laser-diode technology over the last decade made efficient continuous-wave (CW) operation of Ruby possible. This concept of using modern pump diodes to realise efficient laser operation using gain media that were believed to be redundant at the time is not only applicable to Ruby. For example, Ytterbium-doped laser material were initially discovered in the 1960s but then cast-aside due to its high-threshold. Only later with the development of high-power laser diodes at Ytterbium's pump wavelength that low quantum defect pumping was possible and with it ultra-high-power laser operation [10].

Similar to Ruby is Chromium-doped Chrysoberyl, commonly referred to as Alexandrite. Like Ruby, Alexandrite was widely used as a high-energy Q-switched laser but with the added benefit of tunable laser operation in the near-infrared. Its wavelength tunability made it an ideal laser source for narrow-linewidth applications [11, 12]. However, the development of laser-pumped Titanium-doped Sapphire at the end of the 1980s limited the applications of Alexandrite lasers.

Over the last two decades there has been considerable progress in the output power of red laser-diodes driven by the demands in the display industry. This realised the potential for watt-level diode-pumped Alexandrite lasers with optical efficiencies over an order magnitude higher than conventional flashlamp pumping [13]. By the start of the 2010s diode-pumped Alexandrite lasers became a highly promising laser source for satellite-based atmospheric remote sensing [14]. Its potential for high-energy Q-switched operation, with stable and reliable diode-pumping and its accessibility to near-infrared absorption lines makes it an attractive alternative to the currently-used Nd:YAG lasers which require multiple frequency conversions to access the near-infrared [15–17].

Motivated by the emergence of diode-pumped Alexandrite lasers the aim of this work is to power-scale CW tunable Alexandrite lasers. In the last five years the rapid growth of quantum technologies has bought a demand for high-precision laser sources for manipulating and probing atoms in various experiments such as laser cooling, atom interferometry and controlling Rydberg atoms - the building block of quantum engineering [18]. These experiments require narrow-linewidth laser sources, typically in the near-infrared where the resonance lines of atoms such as Rubidium at 780 nm [19] are located.

Laser diodes are well suited to these applications with $<$100 kHz linewidth and

low cost but have limited brightness and power. Frequency-doubled Erbium-fibre lasers provide higher brightness but with added complexity [20]. Titanium-doped Sapphire lasers have long been the flagship solid-state laser in a wide range of applications and are well suited to the requirements of quantum technologies. However, due to the lack of high-power diodes at its pump wavelength, it requires laser pumping from frequency-doubled 1 µm lasers. This makes it bulky, expensive and, with the requirement of water-cooling, non-portable. Using diode-pumped Alexandrite lasers offers a simpler and more compact solution with direct diode-pumping, and the potential for lower noise performance due to its low emission cross section. Its unique ability to perform well at elevated temperatures also removes the requirement of bulky water-cooling.

This thesis demonstrates significant progress in the performance of tunable Alexandrite lasers. Previously, progress in tunable Alexandrite lasers has been limited to <1 W of output power with higher power operation at the expense of output mode quality. Here, power-scaled Alexandrite lasers with broad wavelength tuning, diffraction limited beam quality and single-longitudinal-mode performance are presented that bring Alexandrite lasers a step closer to realising its potential as an attractive laser source outside the laser laboratory.

The thesis is formed of eight chapters. Chapter 2 provides an overview on diode-pumped solid-state lasers. Theoretical background is provided on laser resonators, such as cavity stability, Gaussian beams and wavelength selection. Gaussian beam propagation and mode size equations are used throughout the thesis to design and model Alexandrite lasers.

An in-depth overview of Alexandrite is covered in Chapter 3. This forms the basis for the theoretical models used later in the thesis. A brief literature review of Alexandrite lasers is also provided.

Chapter 4 covers the experimental demonstration of a wavelength tunable Alexandrite laser in which wavelength tuning was obtained by simply tilting a Brewster-cut crystal inside the laser cavity. Narrow-linewidth continuous tuning and dual wavelength operation were both obtained without any other wavelength selective element due to the birefringent properties of Alexandrite. This is a simple and novel method of achieving wavelength tuning. A theoretical model was also developed and shown to be in good agreement with the experimental results. It can also be applied to other birefringent gain media.

Chapter 5 describes the first detailed experimental measurement and analytic

model of pump-induced lensing in diode-pumped Alexandrite lasers. Using a Shack-Hartmann wavefront sensor the pump-induced lens for an end-pumped Alexandrite laser is measured under both non-lasing and lasing conditions for the very first time. Surprising results are obtained with the lens dioptric power under lasing conditions found to be up to 60 % of that under non-lasing conditions. A theory of a combined thermal lens and population lens - which arises from an inversion dependent refractive index - is formed and shown to match well with the measured data both qualitatively and quantitatively. This work has furthered the understanding of pump-induced lens effects in end-pumped Alexandrite lasers and the theoretical model can be applied to other laser gain media.

Chapter 6 covers the power-scaling of TEM_{00} Alexandrite lasers utilising the improved understating of the pump-induced lensing in Alexandrite and using a simple convex-plane cavity design. Diode-pumped Alexandrite lasers operating with high optical efficiency (>30 %), record slope efficiencies (54.9 %) and >5 W of laser output in TEM_{00} mode are demonstrated for the very first time. Multi-watt wavelength tuning as well as dual wavelength operation using a birefringent filter is obtained in addition to fixed narrow linewidth operation using a volume Bragg grating. In dual-end-pumped configuration up to 8.6 W of power in TEM_{00} mode is obtained - the world record for the highest powered TEM_{00} diode-pumped Alexandrite laser.

Chapter 7 is an overview of single-longitudinal-mode (SLM) Alexandrite ring lasers. The first two sections describe systems developed based on using focusing optics in an astigmatic and non-astigmatic configuration. These results produced the first diode-pumped Alexandrite laser in CW SLM operation. The third section investigates the power-scaling capabilities of Alexandrite ring lasers with a >5 W TEM_{00} bidirectional ring laser demonstrated. This result shows the potential for multi-watt wavelength tunable SLM operation from Alexandrite.

Chapter 8 is the final chapter. It summarises the results of the thesis and suggests future work. Results presented in this thesis have contributed to developing novel wavelength tuning in birefringent gain media, enhanced understanding of pump-induced lensing and achieved record performance levels in power-scaled tunable Alexandrite lasers.

Chapter 2

Diode Pumped Solid-State Lasers

Diode-pumped solid-state lasers provide the widest versatility in terms of output power, pulse width, repetition rate, wavelength and linewidth compared to any other laser system [5]. Flexibility in material size and shape, wide ranging properties of different host crystals, amplifiers as well as frequency conversion using non-linear optics are all well developed around diode-pumped solid-state laser systems.

Designing an efficient diode-pumped solid-state laser has three key requirements: a host material that has strong thermo-mechanical properties enabling high power laser operation with low risk of crystal fracture; a dopant-ion with well defined fluorescence and absorption lines with low quantum defect and of size comparable to ions in the crystal host; and finally a diode-pump source with an emission wavelength that matches well with the ion absorption.

Though this thesis is entirely devoted to the study of red-diode-pumped Alexandrite lasers, it is worth considering Alexandrite in the wider context of diode-pumped solid-state lasers. In this chapter the basic properties of diodes, solid-state hosts and dopants will be discussed. In addition, the fundamental theoretical basis of laser resonators will be presented as it provides insight into cavity stability, transverse and longitudinal mode profile and by considering thermal effects, its dynamical behaviour. The analytical equations shown here will be used throughout this thesis to model and design Alexandrite lasers and to analyse the obtained results.

2.1 Solid-State Dopants and Hosts

A solid-state lasing material consists of a solid which contains small amounts of an additional element. The solid is referred to as the host material in which the additional element has been doped into. The doped element possesses electronic transitions within inner non-filled electronic shells. Such dopants are typically rare-earth (RE) or transition metals (TM) with transitions occurring on the $4f - 4f$ (RE), $4f - 5d$ (RE) and $3d - 3d$ (TM) electronic levels. These transitions enable direct emission from the ultra-violet to the near-infrared at around 0.3-3 µm [21].

The host material mainly gives rise to the thermo-mechanical properties of the solid-state material, such as its thermal conductivity, birefringence and hardness. The dopant typically determines the optical properties of the material such as the absorption, lasing wavelength, emission cross section and fluorescence lifetime. An awareness of these properties is key in designing efficient diode-pumped solid-state lasers.

It is highly desirable for the solid-state host to have good thermo-mechanical properties (such as high thermal conductivity and hardness), posses lattice sites that can accommodate the dopant ion (i.e. enable the desired spectroscopic properties), be transparent at the lasing wavelength and have easy fabrication. Examples of commonly used hosts include oxides such as sapphire (Al_2O_3), garnets (such as $Y_3Al_5O_{12}$ or YAG), vanadates (such as YVO_4) and fluorides (such as $YLiF_4$ or YLF) - all of which have their own respective advantages depending on the desired dopant ion and application. Most crystals are fabricated using the Czochralski technique which in the case of YAG enables the growth of boules of up to 80 mm in diameter and 200 mm in length [21].

RE ions doped into solid-state hosts typically operate on the $4f - 4f$ levels with strong but narrow emission lines due to the $5s$ and $5p$ electrons shielding the crystal field. The weak probabilities of interaction between the levels give rise to a long fluorescence lifetime and therefore a large emission lifetime product, $\sigma_e \tau_f$, leading to a low threshold. Two examples of such lasers are Nd:YAG and Yb:YAG, where the doped Nd^{3+} and Yb^{3+} ions replace the similarly sized Yttrium atom. Nd:YAG is a four-level laser with a modest emission cross section and fluorescence lifetime of $\sigma_e = 2.8 \times 10^{-19}\,\mathrm{cm}^2$ and $\tau_f = 230\,\mu\mathrm{s}$, respectively [5]. Its thermo-mechanical properties are also respectable with a thermal conductivity of $K_c = 13\,\mathrm{W\,m^{-1}\,K^{-1}}$ and hardness of $H = 1320\,\mathrm{kg\,mm^{-2}}$. All these good properties as well as the avail-

ability of flashlamp pumping and later high efficiency diode pumping at 808 nm made Nd:YAG the industrial standard laser operating in a variety of configurations. These include >100 W continuous-wave (CW) oscillator [22, 23], Joule-level Q-switched master-oscillator power-amplifier [24], $\sim$ 10 ps pulse durations at MHz repetition rate [25] and linewidth down to the kHz-level [26]. These results provide a simple yet effective benchmark for other laser systems without requiring a detailed analysis of laser theory.

Yb:YAG (a three-level laser) also serves as a useful benchmark. Whilst its emission cross section and fluorescence lifetime are lower, its absorption at 978 nm and broad emission at around 1015-1040 nm enable very low quantum defect heating and sub-ps pulse duration in mode-locked operation. Yb:YAG in thin-disk geometry is the industrial flagship in high average power sub-ps laser systems [27].

TM ions, such as Ti^{3+}, Cr^{2+}, Cr^{3+} and Fe^{2+} can also be doped into solid-state hosts. Unlike RE ions, all TM ions have broad emission bandwidths. This arises from their unfilled d shell being unshielded from the crystal field and so enabling phonon broadening of the absorption and emission bandwidths. Their emission cross section and fluorescence lifetime are typically shorter with a $\sigma_e \tau_f$ product of an order of magnitude less than that for RE ions. However, their broad emission bandwidths enable ultrafast operation at <10 fs. Ti:Sapphire is the most well-established TM solid-state laser. Its absorption spectrum is well matched to the frequency doubled wavelength of Nd:YAG at around 532 nm [28], its broad emission bandwidth has enabled mode-locked operation down to 5 fs [29] and the good thermo-mechanical properties of its Sapphire host enable CW output powers at up 5 W in narrow-linewidth wavelength tunable systems [30].

Cr^{2+}:ZnS and Cr^{2+}:ZnSe, referred to as the Ti:Sapphire of the mid-infrared, are other examples of well-established TM solid-state lasers. Their extensive spectral range of 1800-3400 nm enable sub-100 fs mode-locked operation [31] and the availability of high-power Thulium-fibre pumping have recently enabled >1 W <50 fs ultrafast [32] and >100 W CW operation at 2500 nm [33].

2.2 Diode Lasers

Diode lasers are the most compact, reliable and cost-effective laser sources. They're widely used in a number of various applications at a broad wavelength range including optical communication, medicine, gas monitoring, remote sensing and more

recently in automotive lidar. A diode laser is a pn-junction where lasing action is possible with an electrical current generating the population inversion, and electron-hole recombination is the source of stimulated emission. The higher refractive index of the active layer compared to the cladding layer fulfils the condition for a standing wave to oscillate and the laser mode to propagate in a resonator that is formed by a cleaved end-facet [5].

The emission wavelength depends on the size of the band which can be altered either with the composition of the pn-junction material or, to a lesser extent, the temperature. Historically, laser diodes were developed at wavelengths of 0.8 µm, 1.3 µm and 1.55 µm owing to their low loss and/or low dispersion in standard optical fibres [34]. Power scaling was mainly aimed at AlGaAs based laser diodes in the 0.8-1.1 µm range as pump sources for Nd-doped lasers and Er-doped fibre amplifiers. More recent development in InGaN and AlGaInP diodes in the last two decades have extended the spectral coverage of high-power laser diodes into the visible.

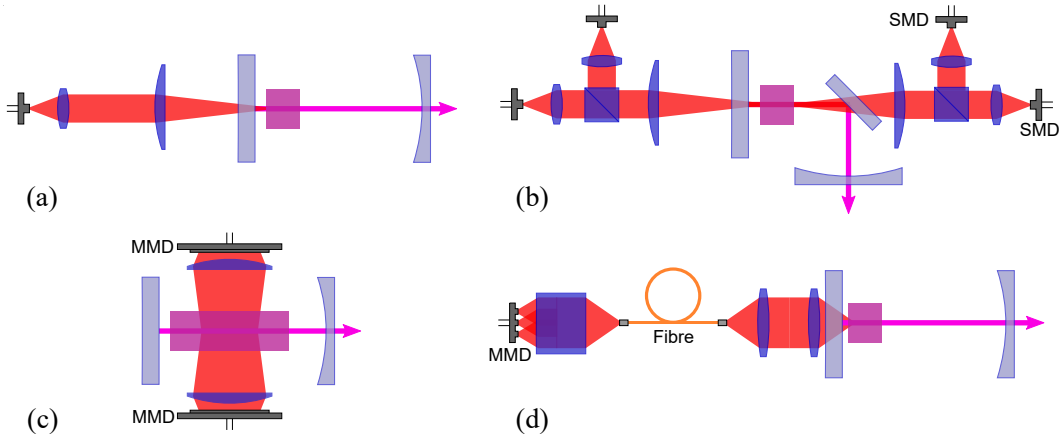

Figure 2.1: Diode-pumping configuration examples: (a) SMD end-pumping. (b) polarisation-combined dual-end-pumping with SMD. (c) MMD side-pumping. (d) Fibre-coupled MMD end-pumping.

A single-stripe, edge-emitting laser diode will typically emit an elliptical transverse mode with a broad laser linewidth owing to the diode geometry and the short cavity lifetime. The output mode can however be easily circularised and brought up to a watt-level of output power with near-diffraction limited beam quality from these single-mode-diodes (SMD). Provided the diode emission is well matched to the absorption of the solid-state material, this provides a simple, compact and highly efficient method of pumping a solid-state gain medium, typically in a longitudinal,

or end-pumped configuration, as shown in Fig. 2.1(a). This provides an efficient overlap between the pump and laser modes inside the laser resonator. Double-end-pumping configurations with polarisation combining (if possible) can increase the pump power further, as shown in Fig. 2.1(b).

For higher power pumping diode arrays, bars and stacks can be formed where larger or multiple single-emitters are used to form multi-mode diodes (MMD). Though this is at the expense of the brightness, coherence and symmetry, a variety of techniques can be used to mitigate the effects, such as fibre-coupling (see Fig. 2.1(d)), using a pair of mirrors [35] or using different pumping geometry such as side-pumping where the power is more evenly distributed in the longitudinal direction and enables multiple pumping sources [34], as shown in Fig. 2.1(c).

2.3 Laser Resonator

A laser resonator consists of a passive resonator (such as a Fabry-Perot resonator) and an active gain medium. A comprehensive mathematical description and derivation of the transverse and longitudinal modes of a laser resonator based on light diffraction using the paraxial wave equation can be found in a number of standard laser textbooks, as shown comprehensively by Siegman in Lasers [36] and more briefly by Svelto in Principles of Lasers [37]. However, in the interest of laying the groundwork for the remainder of this thesis it is worth providing a very brief overview of these works. Expressions for the transverse and longitudinal modes provide a well-rounded description of the laser resonator in its entirety including its intensity distribution, propagation and resonator stability. Key analytical parameters are derived enabling laser cavity modelling and design.

The propagation of an electromagnetic (EM) field inside a passive resonator can be described using the ray-model, where the geometrical propagation is described but not its diffraction. Despite the limitations of the ray model it does provide a simple and accurate description of the stability of the laser cavity and of the propagation of the laser mode.

Ray transfer matrices (RTM) are a very useful way of describing light propagation. A ray of light travelling along the optical axis, z, can be defined according to its displacement above the optical axis, r, and the relative angle between the ray and the optic axis, α, as shown in Fig. 2.2(a), which also shows the propagation of a ray through an optical element such as a lens or an optical system. The output

ray, $\vec{r}_2$, is related to the input ray, $\vec{r}_1$, via the RTM

$$\vec{r}_2 = \mathbf{M}\vec{r}_1 \tag{2.1}$$

where $\mathbf{M}$ is the RTM - a 2×2 matrix representing the optical system between the input and output ray. In component form:

$$\begin{bmatrix} r_2 \\ \alpha_2 \end{bmatrix} = \begin{bmatrix} A & B \\ C & D \end{bmatrix} \times \begin{bmatrix} r_1 \\ \alpha_1 \end{bmatrix}. \tag{2.2}$$

The RTM for a cascaded optical system with n elements is described by the matrix multiplication of each element, i.e. $M = M_n M_{n-1} \ldots M_2 M_1$. For a periodic focusing system, such as a resonator, the RTM at the reference plane is given by a single-round-trip, as shown in Fig. 2.2(b). The resonator is stable when the following condition is satisfied

$$-1 \leq \left(\frac{A+D}{2}\right) \leq 1. \tag{2.3}$$

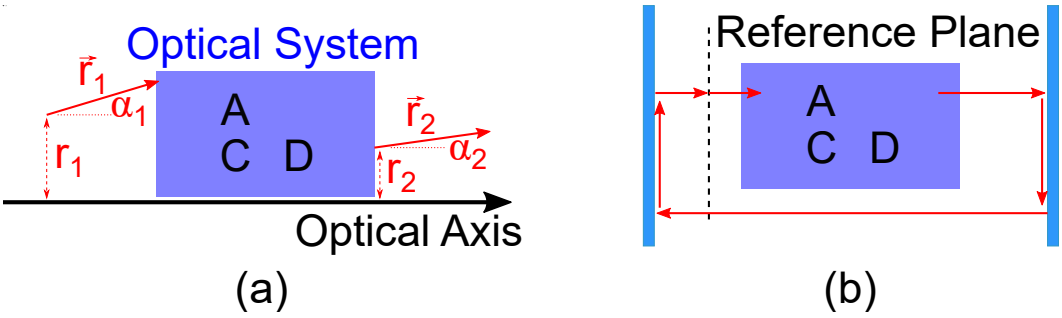

Figure 2.2: (a) Ray propagation through an optical system. (b) Round-trip ray transfer matrix with respect to the reference plane.

A more accurate description of the EM field inside a laser resonator is obtained using a wave description that accounts for the effect of diffraction. Assuming a monochromatic EM wave with uniform polarisation, its electric field, $\tilde{E}$, can be described by the scalar wave equation

$$\left(\nabla^2 + k^2\right) \tilde{E}\left(x, y, z\right) = 0 \tag{2.4}$$

where $k = \omega/c$ is the wavevector. Under the paraxial approximation the change in the electric field in the z direction can be considered to be negligible and the

electric field can be written as $\tilde{E} = u(x, y, z)\exp(-ikz)$. As such Eq. (2.4) reduces to the paraxial wave equation which is given by

$$\nabla_t^2 u - 2ik\frac{\partial u}{\partial z} = 0 \tag{2.5}$$

where $\nabla_t^2 = \partial^2/\partial x^2 + \partial^2/\partial y^2$ is the Laplacian operator in the transverse plane. It can be shown by direct substitution that Eq. (2.5) has a solution of the form

$$u(x, y, z) \propto \exp\left[-ik\left(\frac{x^2 + y^2}{2q}\right)\right] \tag{2.6}$$

where q is the eigensolution to Eq. (2.5). There are several exact solutions however the most applicable solutions in this case are the orthogonal set of Hermite-Gaussian (HG) modes which do not change shape with propagation in free-space and so satisfy the conditions of self-reproduction necessary in a laser cavity. In Cartesian coordinates the electric field of the HG mode is given by

$$u_{n,m}(x, y, z) = \sqrt{\frac{2}{\pi w^2(z)\, 2^{n+m} n! m!}} H_n\left(\frac{\sqrt{2}x}{w(z)}\right) H_m\left(\frac{\sqrt{2}y}{w(z)}\right) \exp\left(-\frac{(x+y)^2}{w^2(z)}\right) \exp\left[-\frac{ik(x+y)^2}{2R(z)} + i(1+n+m)\phi\right] \tag{2.7}$$

where H_n and H_m are Hermite polynomials of the order n and m. The lowest order mode is when $n = m = 0$, and the Hermite polynomial is a constant, $H_0 = 1$. The electric field and the intensity are then simply a Gaussian. This is typically denoted as a TEM_{00} mode, where TEM stands for transverse electro-magnetic mode, and the subscript denotes the order n and m. Figure 2.3 shows the intensity distribution of the TEM_{nm} modes. A notable feature of the higher order modes ($n > 0$ and/or $m > 0$) is the offset maxima and the presence of a minima, where the number of minima in each direction correspond to the order number.

A similar family of modes can be obtained in cylindrical coordinates. These modes are characterised by the Laguerre polynomials of order p and l which give rise to a mode structure consisting of annular rings or petal-type modes. The lowest order Laguerre-Gauss mode, LG_{00}, is identical to the lowest order Hermite-Gaussian mode. A notable feature of these modes is that they possess orbital angular momentum (OAM) due to a spiral phase term in the expression for the electric field.

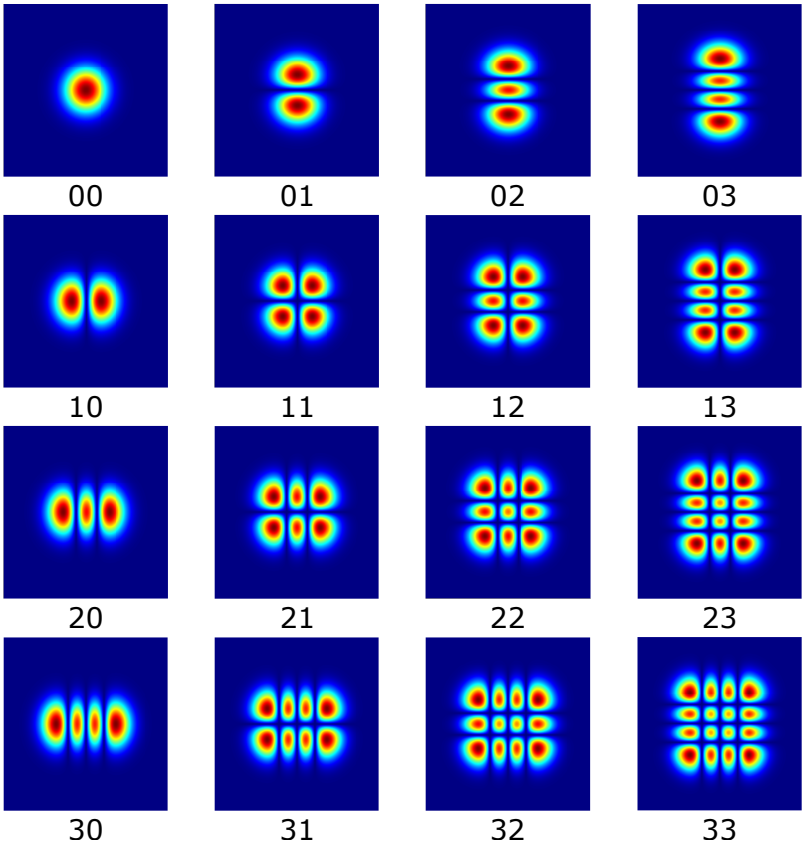

Figure 2.3: Hermite-Gaussian modes of a laser resonator.

The annular intensity and OAM enable a number of specialised applications such as optical tweezers and micro-machining. Recent emergence in their use in optical communications and quantum technologies has led to significant development in the design and development of vortex lasers [38].

Comparing Eqs. (2.6) and (2.7) gives the expression for the eigensolution, or the complex beam parameter

$$\frac{1}{q} = \frac{1}{R} - i\frac{M^2\lambda}{\pi w^2} \tag{2.8}$$

where R is the radius of curvature, w is the beam width and M^2 is the beam quality factor. The complex beam parameter can be used to fully describe the HG mode and its propagation through an optical system using the RTMs. The ABCD law of Gaussian beam propagation is given by

$$q_2 = \frac{Aq_1 + B}{Cq_1 + D} \tag{2.9}$$

where q_1 and q_2 are the initial and final complex beam parameters, respectively.

2.4 Gaussian Beam

The lowest order mode, or TEM_{00} mode, has a Gaussian intensity profile in the radial component, $r = \sqrt{x^2 + y^2}$, given by

$$I(r) = I_0 e^{\left(-2r^2/w^2\right)} \tag{2.10}$$

where w is the beam width and is defined as the radial position at which the intensity falls by a factor of $1/e$. Due to its Gaussian profile the propagation of the TEM_{00} is referred to as a Gaussian beam. A Gaussian beam will propagate with a Gaussian intensity distribution but with a varying width, as illustrated in Fig. 2.4.

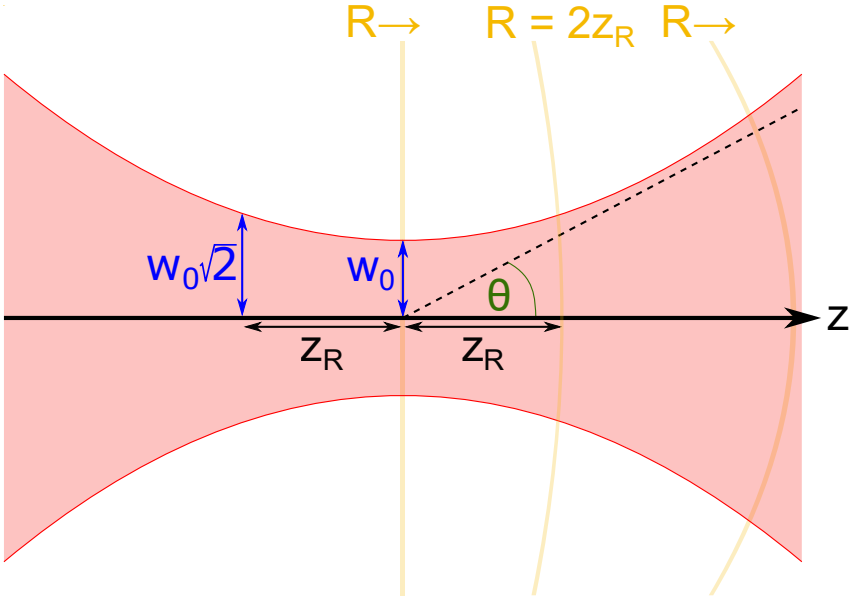

Figure 2.4: Gaussian beam propagation.

The Gaussian beam will focus to a minimum width, or waist, of w_0 at $z = 0$. The beam width varies in the axial position, z, as a hyperbola of the form

$$w(z) = w_0\sqrt{1 + \frac{z^2}{z_R^2}} \tag{2.11}$$

where z_R is the Rayleigh range, the distance from the waist to where the beam area has doubled. Twice the Rayleigh range, $2z_R$, or the confocal parameter, is the distance over which the Gaussian beam is considered to be collimated. The Rayleigh range is simply given by

$$z_R = \frac{\pi w_0^2}{M^2\lambda} \tag{2.12}$$

where M^2 is the beam quality factor. The radius of curvature is given by

$$R(z) = z\left(1 + \frac{z_R^2}{z^2}\right). \tag{2.13}$$

From Eq. (2.13) it can be seen that at $z = 0$, $R \to \infty$ and so the wavefront is plane at the waist. With increasing z, R decreases to a minimum at $z = z_R$. For large z, $R \approx z$ and so the wavefront is again plane as $z \to \infty$. Another useful parameter is the half-angle divergence (shown in Fig. 2.4) which is given by

$$\theta = \frac{M^2\lambda}{\pi w_0}. \tag{2.14}$$

The final expression to consider from Eq. (2.7) is the Gouy phase factor, ϕ, which is given by

$$\phi = \arctan\left(\frac{z}{z_R}\right). \tag{2.15}$$

The Gouy phase factor is an axial phase shift adding a total π phase shift for a fundamental Gaussian beam travelling through the waist where the phase fronts will shift by half a wavelength compared to an ideal plane wavefront. This has two important implications. Firstly it completes the description of a Gaussian beam. A Gaussian beam can be described as a spherical beam travelling in the axial direction with a Gaussian intensity profile. The Guoy shift provides the distinction from a pure spherical beam by accounting for the change in phase around the waist. Secondly, for higher order modes the change in phase wavefront at the waist will be different, and so their oscillation frequency in a stable resonator will also differ.

2.5 M^2 Parameter

The HG modes correspond to an orthonormal set and so any arbitrary field can be decomposed into a sum of these modes. The oscillating EM field inside the resonator is therefore not necessarily defined by a single TEM_{nm} mode but instead as a coherent or incoherent mixture of multiple modes. The most common method of characterising the transverse mode profile is the M^2 parameter. Precise knowledge of the modal composition cannot be obtained with this method, but for most applications, and for this thesis, it is sufficient. The beam quality factor or simply M^2 is the comparison between the measured beam and the ideal TEM_{00} beam [5]. By measuring the beam width as a function of distance through the focus, the M^2 parameter can be calculated using Eq. (2.11) with z_R substituted using Eq. (2.12), this gives

$$w_i(z) = w_{0_i}\sqrt{1+\left(\frac{M_i^2\lambda z}{\pi w_{0_i}^2}\right)^2} \tag{2.16}$$

where $i = x, y$, and so expressions for the beam quality are typically described in the two orthogonal directions. A pure HG mode will have a beam quality given by

$$M_x^2 = 2n+1 \tag{2.17}$$

$$M_y^2 = 2m+1 \tag{2.18}$$

however in most cases it is sufficient to use the beam quality simply as a measure for how near diffraction limited the beam is. Measuring the beam quality is crucial in demonstrating the capabilities of the laser, since most applications require a TEM_{00} mode, as it has the lowest diffraction and smallest focusing size. Measuring the beam quality of the pump system (which for diode pumping $M^2 \gtrsim 50$), enables the achievable pump waist size and confocal parameter to be calculated. Knowledge of this is important for providing high absorption efficiency and in aiming for mode-matching when designing the laser cavity.

2.6 Cavity Stability

It is useful to consider the cavity stability of a passive resonator since it provides a simple description of the stability range without having to include the effects of the gain medium. A passive resonator consists of at least two highly reflective mirrors separated by a length L, as shown in Fig. 2.5. The simplest resonator, shown in Fig. 2.5(a) is the plane-parallel resonator and consists of two plane mirrors. Considering an EM wave travelling inside the resonator, then for the electric-field to be zero at the mirror surface the cavity length must satisfy the condition $L = n\lambda/2$. The resonant frequencies are therefore given by $\nu = n(c/2L)$ and their separation, or longitudinal spacing, is simply $\Delta\nu = c/2L$.

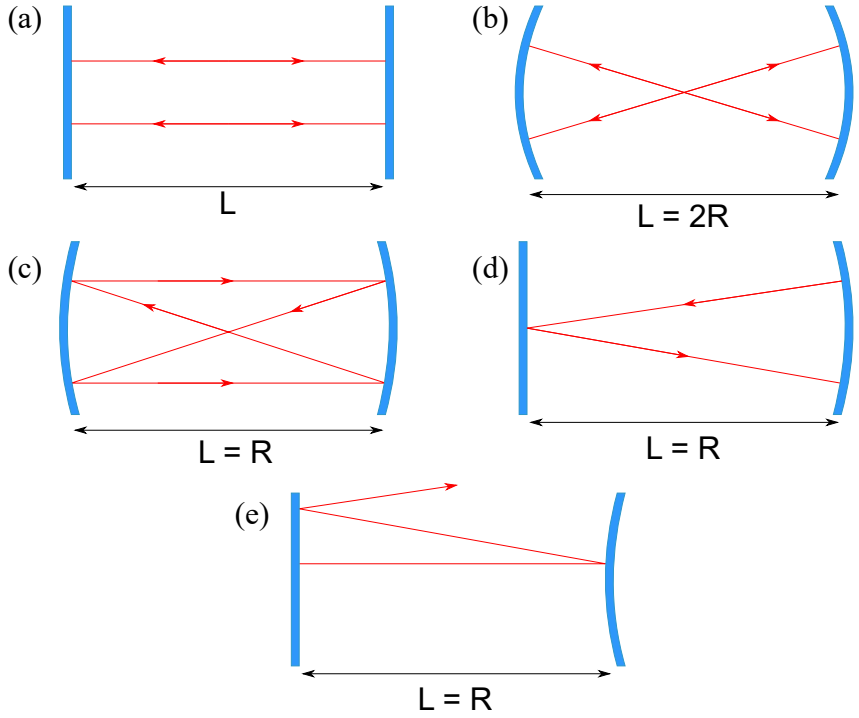

Figure 2.5: Resonator configurations: (a) Plane-parallel (b) Concentric (c) Confocal (d) Hemispherical (e) Unstable.

Alternative resonator configurations with curved mirrors are shown in Figs. 2.5(b)-(e). The red lines indicate the light propagation using the ray model which can be used to distinguish stable and unstable resonators. In a stable resonator (Figs. 2.5(a)-(d)) the rays are well confined inside the resonator, whereas for an unstable resonator, as shown in Fig. 2.5(e), rays cannot be entirely confined and

will eventually escape. However, unstable laser resonators are not without purpose and have been used extensively in high-power laser systems due to their large mode volume and are still of interest to the research community today [39, 40].

For a two mirror resonator the round-trip RTM is given by $M = M_{R1}M_LM_{R2}M_L$ where M_{Ri} is the matrix for a mirror of curvature R_i and M_L is the matrix for free-space propagation over length L. Using Eq. (2.3), the stability condition is

$$-1 \leq 2\left(1 - \frac{L}{R_1}\right)\left(1 - \frac{L}{R_2}\right) - 1 \leq 1. \tag{2.19}$$

It is more convenient to define the stability of the cavity according to the dimensionless g-parameters which are given by $g_1 = 1 - L/R_1$ and $g_2 = 1 - L/R_2$. The stability condition then reduces to a simple form

$$0 \leq g_1 g_2 \leq 1 \tag{2.20}$$

which can be plotted as shown in Fig. 2.6. This provides an effective way of determining the stability of the cavity and the effect of changing the cavity properties with $g_1g_2 = 1$, $g_1 = 0$ and $g_2 = 0$ defining the edges of stability. The region of cavity stability is indicated by the shaded zone in Fig. 2.6. The position of the stable passive resonators in Fig. 2.5 are indicated according to their g-parameters. The plane parallel, concentric and confocal cavities are all on the edge of stability since only specific rays are fully confined to the resonator. The effect of increasing the resonator length for a cavity with two curved mirrors of equal curvature from $L = 0$ to $L = 2R$ is indicated by the red arrow.

2.7 Active Resonator

In an active laser resonator the mode size needs to be maximised at the gain medium for efficient gain extraction. Achieving this requires operating the resonator near to the edge of stability according to the two-mirror resonator model. Near the edge of stability small changes to the mirror alignment and the effect of the gain medium can have a large effect on the mode size and cavity stability. It is therefore essential to understand the effect of the gain medium on the overall cavity stability.

A simple method that provides analytical solutions is to model the gain medium as a thin lens arising from pump-induced lensing effects such as thermal lensing (which will be discussed in greater detail in chapter 5). The properties of a resonator

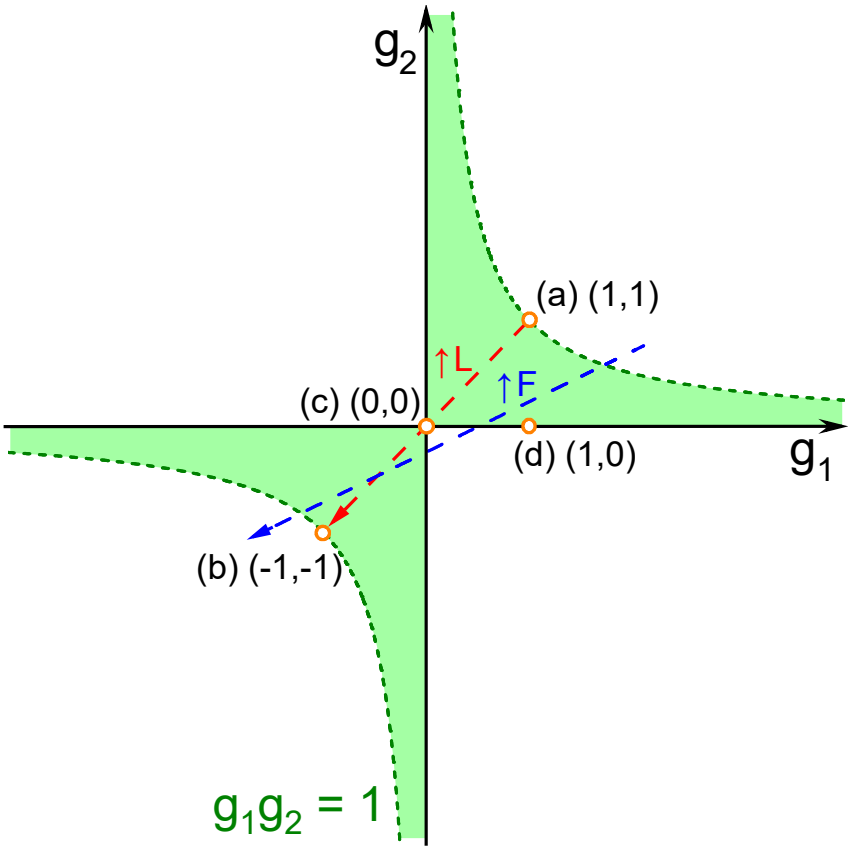

Figure 2.6: Cavity stability diagram. Shaded green region indicates stable region.

with a thin lens have been studied by Magni where the stability g-parameters are adapted to the form [41]

$$g_1 = 1 - \frac{L_2}{f} - \frac{L_0}{R_1} \tag{2.21}$$

$$g_2 = 1 - \frac{L_1}{f} - \frac{L_0}{R_2} \tag{2.22}$$

where f is the focal length of the thin lens, L_1 and L_2 describe the mirror and lens separations as shown in Fig. 2.7(b) and L_0 is an effective length given by

$$L_0 = L_1 + L_2 - \frac{L_1 L_2}{f}. \tag{2.23}$$

Note that for a weak lens Eq. (2.23) reduces to $L = L_1 + L_2$ and Eqs. (2.21)

and (2.22) reduce to those for a two mirror resonator. To illustrate the effect of an increasing lens dioptric power ($F = 1/f$) consider the resonator shown in Fig. 2.7(a) with $R_1 = -100\,\text{mm}$, $R_2 = 500\,\text{mm}$, $L_1 = 50\,\text{mm}$ and $L_2 = 60\,\text{mm}$. Its position on the stability diagram is shown in blue in Fig. 2.6. Initially, with $f = 5000\,\text{mm}$ the cavity is unstable. Increasing the lens dioptric power shifts the resonator into stability before exiting back into the unstable region. Further increase moves the resonator into the second region of stability until at a short focal length of around $f \sim 25\,\text{mm}$ the resonator is unstable.

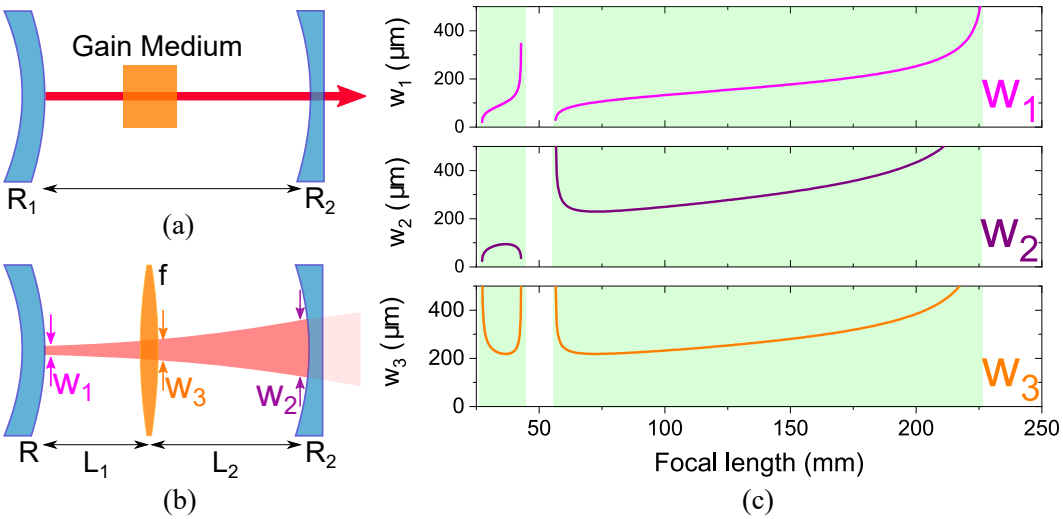

Figure 2.7: (a) Active laser resonator. (b) Resonator model with internal thin lens. (c) Beam width at first mirror (w_1), second mirror (w_2) and lens (w_3) as a function of the focal length, f.

Understanding the dynamic behaviour of the resonator is an important aspect for designing efficient diode-pumped solid-state lasers. With an appropriate cavity design the range of cavity stability can be optimised. Optimisation of the mode size is another essential factor, be it maximising the gain extraction or to minimise damage at the end-mirrors. The mode sizes at the first mirror, second mirror and at the lens are given by [41]

$$w_1 = \sqrt{\frac{\lambda\,|L_0|}{\pi}} \left(\frac{g_2}{g_1\,(1 - g_1 g_2)} \right)^{\frac{1}{4}} \tag{2.24}$$

$$w_2 = \sqrt{\frac{\lambda\,|L_0|}{\pi}} \left(\frac{g_1}{g_2\,(1 - g_1 g_2)} \right)^{\frac{1}{4}} \tag{2.25}$$

$$w_3 = \sqrt{\frac{\lambda}{\pi}} \left(\frac{4u_1 u_2 g_1 g_2 + (u_1 - u_2)^2}{(1 - g_1 g_2)\, g_1 g_2} \right)^{\frac{1}{4}} \tag{2.26}$$

where $u_1 = L_1(1 - L_1/R_1)$ and $u_2 = L_2(1 - L_2/R_2)$. The mode size (beam width radius) for the model cavity is shown as a function of the focal length of the thin lens, f, in Fig. 2.7(c). Comparing these to the position of the resonator on the cavity stability diagram provides useful insight into the behaviour of the laser mode. For a weak lens the mode size at the two mirrors is infinite and no stable mode can oscillate. Increasing the focal length of the lens provides a stable mode size until it reaches a minimum at the first mirror and the resonator is no longer stable at $g_2 = 0$. The resonator then crosses into the second stability region with the waist located at the second mirror. With further reduction in the lens focal length there is a waist at both mirrors and the mode size is maximised at the lens. These analytical expressions therefore provide an effective means of designing and analysing simple laser resonators.

For a more complex laser resonator containing multiple elements numerical solutions are required to determine the mode size. The mode size at a reference plane, as indicated previously in Fig. 2.2(b) is given by

$$w = \sqrt{\frac{|B|\,\lambda}{\pi}} \left(\frac{1}{1 - m^2} \right)^{1/4} \tag{2.27}$$

where $m = (A + D)/2$. The mode size at any location inside the resonator can then be determined using the standard Gaussian propagation formula. The cavity design can be modelled using commercially available software (e.g. LASCAD), or by building custom models, which in this work was done in Matlab.

2.8 Longitudinal Modes

The condition for the phase to be to reproduced after a single round-trip means that the total phase shift must be equal to $2\pi q'$ where q' is the longitudinal mode order. The total phase shift is therefore equal to the difference between the phase shift from free space propagation and the round-trip phase change, ϕ_{nm} [37]:

$$2\pi q' = \frac{2\pi L}{c} \nu_{nmq} - \phi_{nm}. \tag{2.28}$$

Rearranged, this gives the resonant longitudinal frequencies of the cavity

$$\nu_{nmq} = \frac{2c}{L}\left[q' + \frac{\phi_{nm}}{2\pi}\right] \tag{2.29}$$

where q' accounts for the change in phase shift after a single round-trip and n, m account for the Gouy phase change through a focus since the different transverse modes experience different Gouy phase changes. The amount of Gouy phase change depends on the focusing of the cavity and so it depends on the cavity geometry which for a stable cavity without astigmatism is given by [37]

$$\phi_{nm} = 2\,(n+m+1)\cos^{-1}\left(\pm\sqrt{AD}\right) \tag{2.30}$$

where A and D are the round-trip components of the RTM of the cavity. Therefore, the frequencies are given by

$$\nu_{nmq} = \frac{2c}{L}\left[q' + \frac{(n+m+1)}{\pi}\cos^{-1}\left(\pm\sqrt{AD}\right)\right]. \tag{2.31}$$

Compared to the frequencies of a passive resonator ($\nu = 2cn/L$) the longitudinal modes and their spacing remain unchanged only that they are shifted for different transverse modes, as shown in Fig. 2.8(a). Even for a narrow linewidth emission laser such as Nd:YAG the frequency spacing is typically an order of magnitude smaller than the gain bandwidth. For example, a $L = 100\,\text{mm}$ long cavity will have a longitudinal mode spacing $\Delta\nu_q = 1.5\,\text{GHz}$ which compared to the Nd:YAG bandwidth of around $\Delta\nu_0 = 12\,\text{GHz}$ at 1064 nm [5] means that several longitudinal modes will be lasing, as shown in Fig. 2.8(b).

2.8.1 Longitudinal Mode Selection

Longitudinal mode selection for narrow-linewidth or even single-longitudinal-mode (SLM) operation can be obtained using a variety of techniques. One simple approach is to use an intra-cavity etalon at an angle. The etalon will have its own transmission window of $\nu_{et} = cn/(2n_{et}d\cos\theta)$ where n_{et} is the refractive index, d is the thickness and θ is the incidence angle on the etalon. Figure 2.8(c) shows how the laser output will now be formed of longitudinal modes that fall within the transmission of the cavity and the etalon.

While several etalons can be used to provide SLM operation it is often at the expense of overall efficiency and does not guarantee stable operation due to pertur-

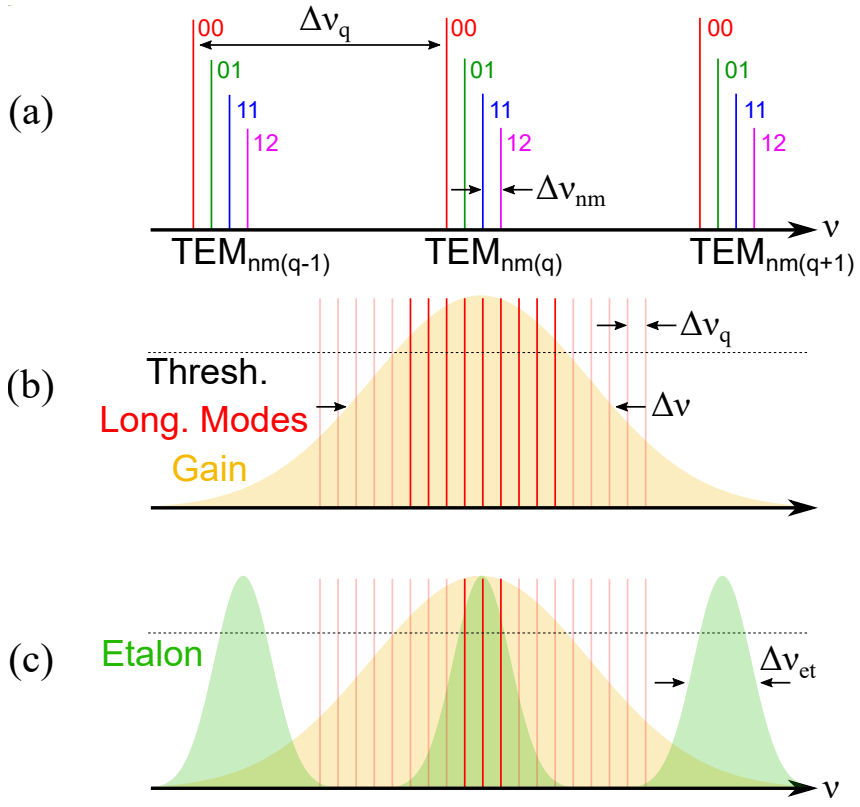

Figure 2.8: (a) Resonant frequencies (b) Gain profile and resonator longitudinal modes. (c) Longitudinal mode selection with etalon.

bations in the cavity length and etalon alignment. There are two common methods for achieving SLM operation in solid-state lasers: microchip lasers and elimination of spatial hole burning.

Microchip lasers are compact lasers with a cavity length that is sufficiently short such that the longitudinal mode spacing is greater than the gain bandwidth. With Nd:YAG this can be achieved with a cavity length of around 1 mm [42], though improved performance can be obtained with higher gain materials such as Nd:YVO_4 [43].

Spatial hole burning is the fundamental limitation of SLM operation in homogeneously broadened gain media. In a standard resonator the longitudinal modes have a standing-wave pattern inside the gain media. A single mode will therefore leave regions of undepleted gain spatially throughout the gain medium. Inversion at these positions may occur through another longitudinal mode giving rise to multiple

longitudinal modes lasing simultaneously.

The most common method of eliminating spatial hole burning in solid-state lasers is using unidirectional ring resonators where the standing-wave pattern is eliminated. Unidirectional propagation is obtained using a Faraday rotator (typically a Terbium gallium garnet crystal with an applied magnetic field) in combination with a half-wave plate and a polarising element such as a Brewster plate or crystal. The principle, which will be explained in greater detail in chapter 7, is that the Faraday rotator in combination with the half-wave plate act to rotate the polarisation for light propagating in one direction and so leading to loss at the Brewster surface. In the opposite direction there is no net polarisation rotation due to the non-reciprocal property of the Faraday rotator and so one direction experiences no loss. Other techniques of eliminating spatial hole burning include the twisted mode technique [44] and using an acousto-optic modulator [45].

2.8.2 Wavelength Tuning

For vibronic gain media such as Ti:Sapphire, Cr:ZnSe or Alexandrite the output wavelength can be tuned over tens if not hundreds of nanometers using various optical elements such as diffraction gratings, prisms or most commonly birefringent filters, which provide minimal insertion loss and flexibility in tuning range and transmission bandwidth. A birefringent filter, when placed at Brewster's angle of incidence, will impart a phase change on an incident p-polarised beam due to the difference in refractive index of the projected polarisation component as it transmits through the filter. The wavelength at which the phase change will be equal to 2π (with no effective change in polarisation) is given by

$$\lambda_m = \frac{\Delta n t}{m} \frac{\sin^2 \gamma}{\cos \theta'_B} \tag{2.32}$$

where $\Delta n = n_e - n_o$ is the refractive index difference between the extraordinary and ordinary refractive indicies, t is the thickness of the filter, m is an integer, γ is the angle between the beam and the optic axis and θ'_B is the internal Brewster angle. By changing γ (by rotating the filter about it's normal axis) it is therefore possible to change λ_m. The free spectral range (separation between successive transmission maxima) is approximated by

$$\Delta\lambda_{\mathrm{FSR}} = \frac{\lambda_m}{\Delta n t} \frac{\cos \theta'_B}{\sin^2 \gamma} \tag{2.33}$$

and is inversely proportional to the filter thickness. Laser operation will occur at λ_m as the polarisation of other wavelengths will be elliptical leading to loss at the Brewster-surface of the filter (and other elements if present). Depending on the gain profile of the laser material and the FSR of the filter it is also possible to generate dual wavelength operation when λ_m and λ_{m+1} (or λ_{m-1}) have the same threshold. Further details on the properties of birefringent filters such as their transmission bandwidth and the variation in the position of the optic axis relative to the surface normal of the filter have been studied by Demirbas et. al [46, 47].

2.9 Summary

The well-developed theory of laser resonators, transverse electronic modes, longitudinal modes and Gaussian beam properties enable accurate laser cavity design for almost any type of laser be it CW, Q-switched, ultrafast or tunable.

Diode-pumped solid-state lasers are a highly versatile type of laser. Decades of research have led to the development of several laser ions doped into a multitude of host crystals. Continuous laser emission at around 0.3-3 µm can be achieved either by direct emission or from otptical-parametric-oscillators (OPO) driven by diode-pumped solid-state lasers.

Research in tunable laser operation from directly-diode-pumped gain media has been growing in recent years owing to the development of laser-diodes. Such lasers are seen as a promising compact, lower cost and simpler alternative to current commercial systems. These include blue-diode-pumped Praseodymium-doped lasers in the visible region [48] and directly-diode-pumped Cr:ZnSe/Cr:ZnS lasers in the mid-infrared [49]. Another is Alexandrite, which due to the emergence of high-power red-diodes over the last decade has seen a renewal in interest.

Chapter 3

Alexandrite

Alexandrite was the first vibronic laser to be demonstrated at room temperature with the earliest journal paper published in 1979 [50]. Like Ruby, the active ion in Alexandrite is Cr^{3+} but doped into Chrysoberyl ($BeAl_2O_4$), this makes it spectrally similar to Ruby but with the distinct difference of tunable operation in the near infra-red with a wavelength range of 701-858 nm [50, 51]. Alexandrite's long fluorescence lifetime and strong mechanical properties made it ideal for high-power continuous-wave (CW) and high-energy Q-switched operation. As such, initial work was predominantly with flashlamp pumping with Joule-level output energy and 60 W CW power reported [11, 12]. Additional techniques such as mode-locking [52] and harmonic generation into the ultra-violet [53] were also reported relatively early on.

Its broad absorption across the visible region has also enabled high efficiency operation by pumping with a Krypton laser [54], red-diode laser [55] and a Dye laser [56], with the latter providing a record slope efficiency of 63.8 %. More recently green laser [57], blue-diode lasers [58], LED-based fluorescent light guide concentrators [59] and even solar pumping have been demonstrated [60].

Flashlamp-pumped Alexandrite lasers were initially applied in scientific and industrial applications as high-precision CW tunable sources before being replaced by the more widely tunable Ti:Sapphire laser. High energy Q-switched operation has also enabled applications in remote sensing [61, 62] and in cosmetic and dermatological applications - an area where it dominates to this day [63].

In recent years Alexandrite has acquired renewed interest primarily due to the availability of commercial high power red-diode lasers [64]. Figure 3.1 shows the number of publications in OSA, SPIE, IEEE, IOP and Elsevier journals related to

Alexandrite (with red-diode pumped Alexandrite shown separately) between 2010 and 2020. It efficiently illustrates the increasing interest in Alexandrite over the previous decade. Of these publications, key results include red-diode-pumped systems with low threshold [65], >26 W CW output power [66], 3 mJ Q-switched oscillator [67], >100 nm wavelength tuning, passive Q-switching [68] and SLM Q-switched operation [69]. Mode-locked operation with red-diode-pumping has yet to be demonstrated though both Kerr-lens [70] and passive [71–73] mode-locking have been obtained with green laser pumping achieving <100 fs pulses.

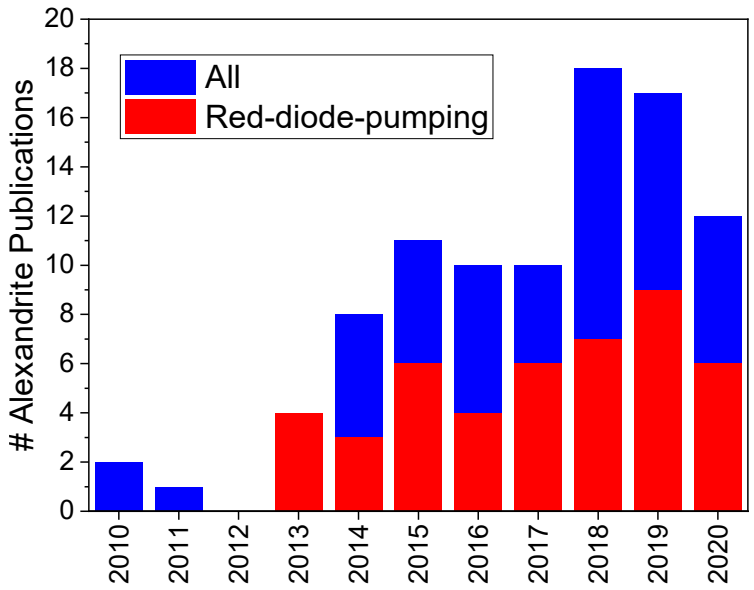

Figure 3.1: Number of publications in OSA, SPIE, IEEE, IOP and Elsevier journals related to Alexandrite.

Altogether these results demonstrate the wide-ranging potential for red-diode-pumped Alexandrite lasers in a number of different applications. Power scaling and wavelength tuning, requires careful consideration of the physical and spectroscopic properties of Alexandrite. Alexandrite is a birefringent material with a complex energy structure with ground state absorption (GSA) and excited state absorption (ESA) at both the pump and laser wavelengths that are temperature and wavelength dependent. These effects determine the lasing characteristics and performance of Alexandrite and so it is important to address these properties. This chapter therefore acts as a review of the material as well as laying the groundwork for modelling wavelength tuning and pump-induced lensing that is explored in future chapters.

3.1 Physical Properties

Alexandrite is a naturally occuring gemstone well known for its trichoism effect. Synthetically, it can be grown via the Czochralski process into large crystals with good optical properties with a nominal Chromium-doping of 0.05-0.3 at.% but with up to 0.5 at.% reported.

Alexandrite has an orthorhombic structure with low crystal symmetry. Its physical anisotropy is reflected in its unit cell dimensions, which in the Pnma terminology are $a = 9.404\,\text{Å}$, $b = 5.476\,\text{Å}$ and $c = 4.727\,\text{Å}$. Figure 3.2 shows the crystal structure of the Chrysoberyl host.

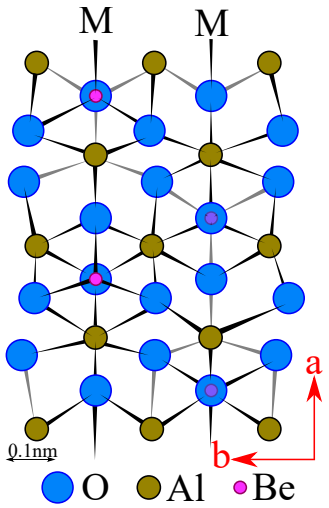

Figure 3.2: Crystal structure of the unit cell of Chrysoberyl along the c-axis. Mirror symmetry planes are denoted by M. Image adapted from [74].

There are two Al^{3+} sites in Alexandrite, the mirror and inversion site. When doped with Cr^{3+} ions around 78 % [75] occupy the mirror site due to its large volume. The physical properties of Alexandrite are shown in Table 3.1 along side those of Ti:Sapphire (Ti^{3+}:Al_2O_3), Nd:YAG (Nd^{3+}:$Y_3Al_5O_{12}$), Ruby (Cr^{3+}:Al_2O_3) and Cr:LiSAF (Cr^{3+}:$LiSrAlF_6$). Ti:Sapphire and Nd:YAG are well established and commercially successful solid-state lasers and so represent the industrial standard. Ruby and Cr:LiSAF are good examples of other Cr-doped media. Ti:Sapphire and Cr:LiSAF are also good examples of other vibronic solid-state materials in the near-infrared. Values are shown at room temperature, the lasing wavelength and along the lasing axis (i.e. for Alexandrite the values are at 755 nm and along the b-axis).

Table 3.1: Key physical properties of Alexandrite, Ti:Sapphire, Nd:YAG, Ruby and Cr:LiSAF.

	Alexandrite	Ti:Sapphire	Nd:YAG	Ruby	Cr:LiSAF
ρ ($\mathrm{g\,cm^{-3}}$)	3.69 [11]	3.98 [76]	4.56 [77]	3.90 [78]	3.45 [79]
T_M (°C)	1870 [11]	2040 [76]	1920 [78]	2040 [78]	750 [79]
Hard. ($\mathrm{kg\,mm^{-2}}$)	2000 [11]	2200 [76]	1215 [78]	2276 [78]	197 [5]
K_c ($\mathrm{W\,m^{-1}\,K^{-1}}$)	23 [11]	33 [80]	10 [77]	42 [78]	3 [81]
dn/dT ($\times 10^{-6}\mathrm{K^{-1}}$)	6.9 [82]	13 [80]	7.3 [77]	12.6 [78]	-9.1 [83]
α_T ($\times 10^{-6}\mathrm{K^{-1}}$)	6.0 [11]	5.3 [76]	7.5 [77]	5.8 [78]	-10 [81]
n	1.74 [84]	1.76 [5]	1.82 [77]	1.76 [78]	1.39 [85]
$\Delta\alpha_p$ ($\times 10^{-25}\mathrm{cm^3}$)	2.7 [86]	-10 [76]	0.4 [77]	1.7 [86]	4.6 [87]
Dop. Conc. (at. %)	0.05-0.2 [78]	0.05-0.3 [88]	1.0 [78]	0.03 [78]	0.5-10 [85]

One of the main advantages of Alexandrite is its thermo-mechanical properties. Its high melting temperature (T_M) and Knopp hardness (Hard.) are around the same as those of Ti:Sapphire and Nd:YAG. Its thermal conductivity (K_c) which determines how easy heat can be extracted from the gain medium is more than twice that of Nd:YAG and only slightly less than that of sapphire. These properties, coupled with a modest expansion coefficient (α_T) and thermo-optic coefficient (dn/dT) enable high energy and high power laser operation in both CW and pulsed operation with low risk of crystal fracture. In comparison, Cr:LiSAF has very poor thermo-mechanical properties with a hardness and thermal conductivity on the order of a magnitude less than that for Alexandrite, therefore limiting its high power capabilities.

Due to its orthorhombic structure, Alexandrite is optically biaxial with refractive indices: $n_b > n_a > n_c$ [11]. Figure 3.3 shows the refractive index dispersion of Alexandrite at $250 - 2500\,\mathrm{nm}$. Measurement of the refractive index was performed by Walling et al. [11] but at large intervals. For an estimate of the refractive index across the entire range Loiko et al. fitted the measured data at $250 - 1000\,\mathrm{nm}$ using a Sellmeier equation of the form [84]

$$n^2 = A_i + \frac{B_i}{1 - C_i/\lambda^2} + D_i\lambda^2 \tag{3.1}$$

where A_i, B_i, C_i and D_i are the fitting coefficients for the refractive index for light polarised to the $i = a, b, c$ axes. Figure 3.3(a) and 3.3 (b) show the fitting over the entire range and over the lasing wavelength range of Alexandrite, respectively.

The inset of Fig. 3.3(a) shows the index ellipsoid for Alexandrite. Using the fitting, the difference between the refractive indicies, Δn_{ij}, and the angle of the Optic axes to the b-axis, γ_b, can be calculated. The two optic axes, O_1 and O_2, lie in the bc-plane at an angle γ_b to the b-axis, which can be calculated according to [89]

$$\sin\gamma_b = \frac{n_a}{n_b}\sqrt{\frac{n_a^2 - n_c^2}{n_b^2 - n_c^2}}. \tag{3.2}$$

Over the lasing wavelength range there is very little dispersion in both the refractive index difference (values shown in Fig. 3.3(b)) and in the angle between the optic axes and the b-axis which is at around $\gamma_b = 30.4°$.

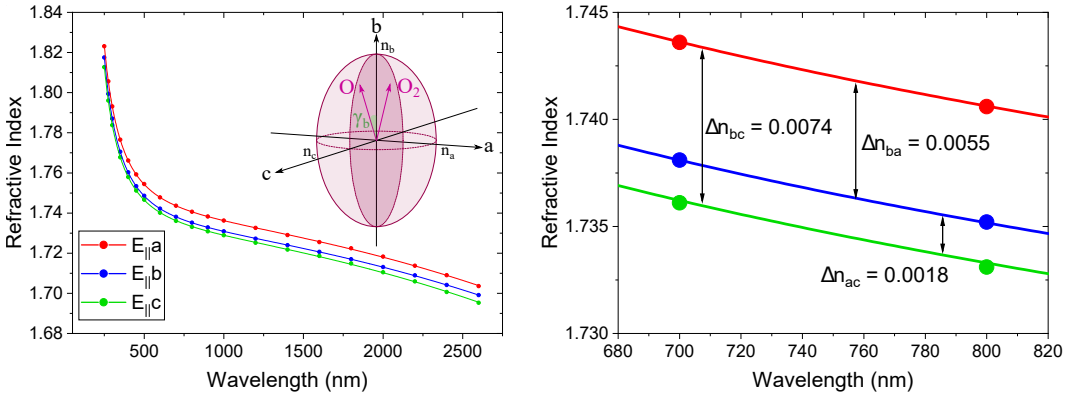

Figure 3.3: (a) Refractive index dispersion at 250-2500 nm. Inset shows index ellipsoid. (b) Refractive index dispersion at 700-820 nm. Refractive index difference also indicated.

3.2 Lasing Mechanism

The lasing energy levels in Cr^{3+}-doped media are characterised by two broad $^4T_2$ and $^4T_1$ absorption states, the $^4A_2$ ground state and the narrow ^2E state. The relative position between the the $^4T_2$ and ^2E states characterises the lasing behaviour of the material.

Figure 3.4 shows the energy level diagram for the Cr^{3+} ion in Alexandrite. The formation of broad absorption bands and their polarisation dependence is discussed in greater detail later in Section 3.3 when the spectroscopic features are included. Here a generalised discussion of the lasing process will be made.

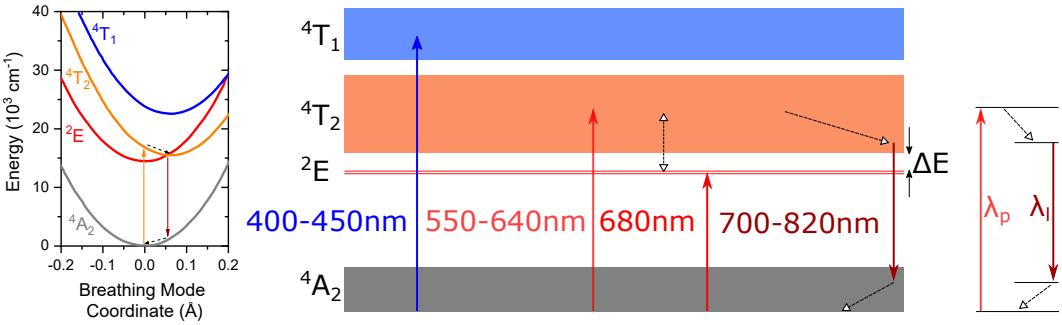

Figure 3.4: (a) Configuration coordindate diagram for the electronics levels. Adapted from [78]. (b) Simplified energy level diagram showing radiative (solid lines) and non-radiative transitions (dashed lines). (c) Four-level vibronic energy scheme.

Four-level and three-level lasing are possible in Alexandrite. In four-level lasing, as shown in Fig. 3.4(a), absorption occurs from the $^4A_2$ band to the $^4T_2$ band. Due to the absorption process being much quicker than the vibrational frequency, absorption may occur to any of the vibrational levels in the $^4T_2$ band. Both the host and the ion are now in an excited state (excited vibrational and excited electronic, respectively). The host loses energy by emitting a phonon (shown as dashed line) and the crystal reaches equilibrium at the minimum vibrational level of the band. The ion then decays via stimulated emission (or spontaneous emission under non-lasing conditions) to an excited vibrational state in the $^4A_2$ band. The host then undergoes another vibrational emission to return to the ground vibrational state. The overall process is equivalent to a four-level laser but with both vibrational and electronic levels, and hence it is referred to as a vibronic system. It's worth noting that discrete transitions are rarely observed due to the broadening of the individual vibrational levels and that the interactions typically involve multiple phonons. Therefore, under four-level lasing, a broad emission is observed. It's worth noting here that this four-level scheme is only strictly valid at around 760-780 nm. Below 760 nm it becomes increasingly quasi-three-level with excited state absorption, and above 780 nm it remains four-level but also with excited state absorption [90] - this will be discussed in greater detail in section 3.3.

The three-level lasing of Alexandrite has pumping from the $^4A_2$ band to the $^4T_2$ band (or $^4T_1$) followed by a fast relaxation to the ^2E level which is the upper laser level. Stimulated emission occurs between the ^2E level and the ground vibrational

state of the $^4A_2$ band. This is an electronic transition producing a narrow linewidth emission.

The lasing mechanism is determined by whichever process has the lowest threshold, which depends on the excited-state occupancy. In the case of Alexandrite the occupancy of the $^4T_2$ band is high enough at room temperature to enable vibronic lasing. This is due to the fact that the energy difference between the two states is relatively small at around $\Delta E = 800\,\mathrm{cm}^{-1}$ which is a few k_BT at room temperature [11]. This allows the $^4T_2$ to have a sufficient population to enable four-level lasing. Ruby on the other hand has an energy difference of $\Delta E = 2350\,\mathrm{cm}^{-1}$ and so the population of the $^4T_2$ state is negligible and far too small to allow four-level lasing, whereas for Cr:LiSAF the ^2E level lies within the $^4T_2$ band and so only vibronic four-level lasing can occur [85].

The temperature dependence of the excited state population can also be visualised by considering the fluorescence lifetime. Due to the thermal coupling between the $^4T_2$ and ^2E states, the fluorescence lifetime depends on the individual lifetimes of each state, their energy separation and the temperature. Using a two-level model, Walling et al. accurately modelled the temperature dependence of the fluorescence lifetime as [11]

$$\tau_f(T) = \tau_E \frac{1 + e^{-\Delta E/k_BT}}{1 + (\tau_E/\tau_T)\, e^{-\Delta E/k_BT}} \tag{3.3}$$

where $\tau_E = 1.54\,\mathrm{ms}$ is the radiative lifetime of the ^2E level, $\tau_T = 6.6\,\mu\mathrm{s}$ is the effective radiative lifetime of the $^4T_2$ band and $\Delta E = 800\,\mathrm{cm}^{-1}$ (0.10 eV) is the energy difference between the ^2E level and the lowest energy level in the $^4T_2$ band [11]. Above $\sim 670\,\mathrm{K}$ non-radiative transitions begin to dominate and the two-level model is no longer valid. Equation (3.3) can be re-written to include the non-radiative lifetime, τ_{NR}, and the activation energy for non-radiative transitions, ΔE_{NR}, this configurational model is given by [91]

$$\tau_f(T) = \frac{1 + e^{-\Delta E/k_BT} + e^{-\Delta E_{NR}/k_BT}}{1 + (\tau_E/\tau_T)\, e^{-\Delta E/k_BT} + (\tau_E/\tau_{NR})\, e^{-\Delta E_{NR}/k_BT}}. \tag{3.4}$$

By fitting Eq. (3.4) to their measured data, Zhang et al. obtained values of $\tau_E = 2.75\,\mathrm{ms}$, $\tau_T = 8.0\,\mu\mathrm{s}$, $\Delta E = 745\,\mathrm{cm}^{-1}$ (0.09 eV), $\tau_{NR} = 6.8\,\mathrm{fs}$ and $\Delta E_{NR} = 12\,400\,\mathrm{cm}^{-1}$ (1.54 eV) [91]. The higher values in comparison to those obtained by Walling et al. were attributed to the higher crystal doping giving rise to increased

radiative trapping. Figure 3.5 shows Eqs. (3.3) and (3.4) plotted as a function of temperature as well as the measured data from literature. Both fittings are performed using the values obtained by Walling et al.

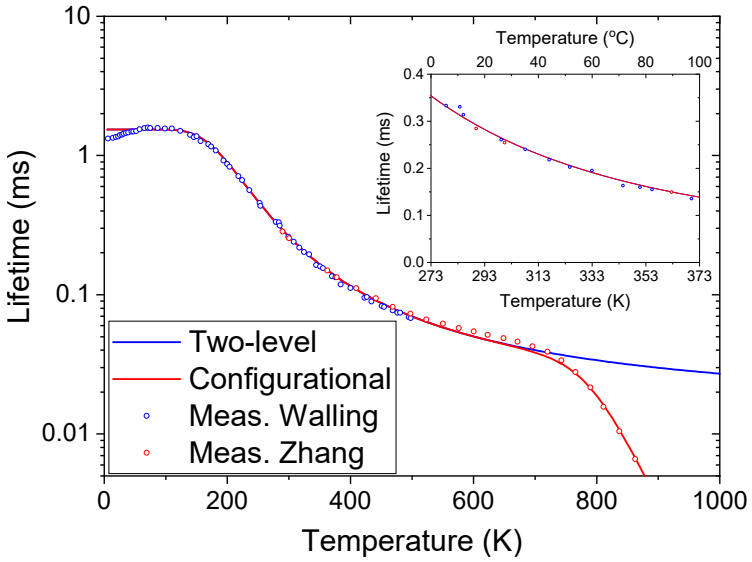

Figure 3.5: Fluorescent lifetime as a function of temperature. Inset shows lifetime over $T = 0 - 100\,^{\circ}\mathrm{C}$ range. Two-level data adapted from [11] and configurational data adapted from [91].

At low temperatures ($T < 200\,\mathrm{K}$) the upper-state population is predominantly in the $^2\mathrm{E}$ level and so the fluorescent lifetime is around 1.54 ms. At high temperatures (500-700 K) the upper state population is now predominantly lying in the $^4\mathrm{T}_2$ band where the shorter lifetime of 6.6 µs is now the dominant contribution to the fluorescent lifetime. In between these two temperature regimes the fluorescent lifetime varies between the two extremes. At 0-100 °C (273-373 K) the lifetime decreases from around 350 µs to 150 µs with a value of $\tau_f = 262\,\mu\mathrm{s}$ at room temperature (300 K), as shown in the inset of Fig. 3.5. The effect of non-radiative transitions (and the difference between the two models) can be clearly seen above 750 K.

The temperature dependent population of Alexandrite allows it to be operated as a vibronic four-level laser at room temperature with a relatively long fluorescent lifetime of $\tau_f = 260\,\mu\mathrm{s}$. As previously mentioned, this makes it highly suitable for Q-switching, especially in comparison to Ti:Sapphire which has a very short lifetime of around 3.2 µs [28]. At cryogenic temperatures it allows Alexandrite to perform as a three-level laser at around 680 nm, the process that is analogous to

Ruby, this cannot be said for Cr:LiSAF which can only operate as a four-level laser. Three-level operation in Alexandrite has been reported using flashlamp pumping (for example [92]) but also recently with blue-diode pumping [58]. This demonstrates the wide ranging performance possible with Alexandrite due to its unique temperature dependent lasing mechanism.

3.3 Spectroscopic Properties

It is also important to address in detail the spectroscopy of Alexandrite including absorption, fluorescence, emission and the effects of ground state absorption (GSA) and excited state absorption (ESA) which play a vital role in determining the overall laser efficiency, wavelength range and the temperature dependence of Alexandrite lasers.

3.3.1 Absorption and Fluorescence

Figure 3.6 shows the GSA cross section of Alexandrite as a function of wavelength for light polarised to the a, b and c-axis over the visible wavelength range. The GSA spectrum consists of two wide bands centred at around 415 nm and 590 nm with a full-width at half-maximum of around 50 nm and 90 nm, respectively, and a narrow band at around 680 nm.

The two wide bands correspond to the vibronic $^4\mathrm{A}_2 \rightarrow {}^4\mathrm{T}_1$ and $^4\mathrm{A}_2 \rightarrow {}^4\mathrm{T}_2$ transitions, as indicated in Fig. 3.4. The GSA transitions can be understood by considering the selection rules. The six oxygens (as shown previously in Fig. 3.2) produce a crystal field, O_h, that distorts the mirror plane but not the inversion plane, hence the lack of lasing action on the inversion plane. The distortion to the mirror plane splits the wavefunction of the $3d$ electrons. Coupled with spin-orbit interaction the $^4\mathrm{T}_1$ and $^4\mathrm{T}_2$ levels are split into finer levels which give rise to a broad absorption [93]. In the case of the $^4\mathrm{T}_2$ level, the finer levels are denoted T_1, T_2 and T_3 with increasing energy. Whilst all transitions are permitted for $\mathrm{E}_{||}b$, for $\mathrm{E}_{||}a$ and $\mathrm{E}_{||}c$ transitions are only permitted to the highest energy T_3 state and so their absorption is weaker and shifted to lower energy. This also bears a significant influence on the fluorescence which will be discussed later. Conversely, for the $^4\mathrm{T}_1$ band, transitions are only permitted to the highest energy level for $\mathrm{E}_{||}b$ whilst all transitions are permitted for $\mathrm{E}_{||}a$ and $\mathrm{E}_{||}c$. Therefore the absorption cross section for $\mathrm{E}_{||}b$ is smaller to the $^4\mathrm{T}_1$ band at 415 nm.

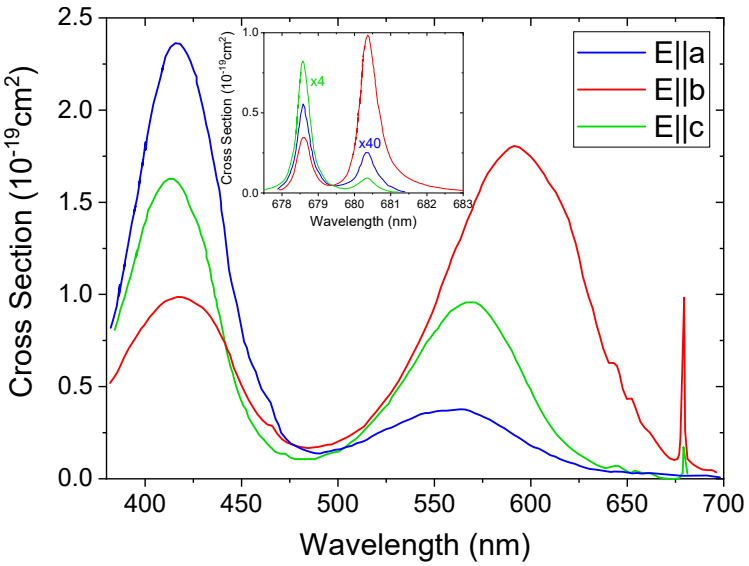

Figure 3.6: Asborption cross section for Alexandrite for light polarised to the a, b and c-axis at room temperature. Image adapted from [11] with Chromium density $N_d = 2.2 \times 10^{19}\,\mathrm{cm}^3$.

The ^{2}E level is also distorted by the crystal field, but not by spin-orbit interaction and so it is split into two narrow lines, denoted R_1 and R_2 (or R-lines), at wavelengths of 678.5 nm and 680.4 nm, respectively. Finer detail of the cross section at this region is shown in the inset of Fig. 3.6. The absorption for $E_{||}b$ is significantly higher than for $E_{||}a$ and $E_{||}c$ due to the selection rules [93]. GSA also extends into the lasing wavelength range and determines the short lasing wavelength cut-off. Its temperature and wavelength dependence are well described using the extended McCumber model [94] that was used for Alexandrite by Walling [11]. It's related to the effective emission cross section and will be discussed in more detail later.

Figure 3.7 shows the fluorescence spectrum for Alexandrite at around 700-850 nm for light polarised to the a, b and c-axis with the inset showing the fluorescence at around 680 nm. The majority of the fluorescence rate occurs at the R-line transitions. Infrared fluorescence at around 700-850 nm corresponds to the phonon-assisted emission as depicted in Fig. 3.4. The fluorescence rate for $E_{||}$b is over an order of magnitude greater than for the other polarisations. As indicated previously, this arises from the reduced occupancy of the $^4T_2$ level for $E_{||}$a and $E_{||}$c polarisations whereas for $E_{||}$b all levels can be occupied and transition is allowed to the ground level. The temperature dependence of fluorescence has been studied by Fibrich et al.

and has found an overall red-shift in fluorescence due to the increasing occupancy of the $^4T_2$ level [95].

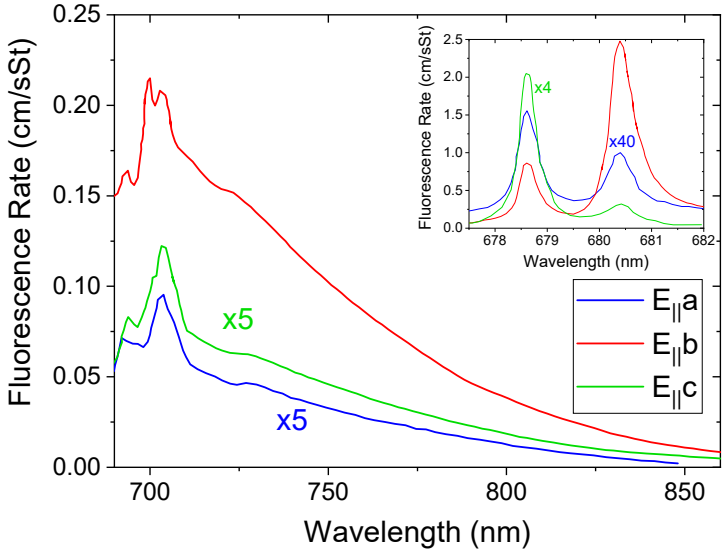

Figure 3.7: Fluorescence spectrum of Alexandrite at room temperature for light polarised to the a, b and c-axis with the inset showing a higher-resolution image at around 680 nm. Image adapted from [11].

Before assessing the spectroscopy of laser emission, laser ESA and GSA as well as pump ESA it is worth discussing all the possible mechanisms that detrimentally effect the upper state population. These mechanisms include thermal quenching, energy transfer upconversion (ETU) and ESA.

Thermal quenching involves the non-radiative decay of the upper-state population. It has been found to occur in Cr:Colquiriites where excited ions tunnel from the $^4T_2$ level to high energy vibronic bands in the $^4A_2$ level [85]. However, this is unlikely to be an issue in Alexandrite where, as mentioned previously, the fluorescence lifetime is well described without taking non-radiative transitions into consideration up to around 750 K. Therefore, with the exception of very high temperatures, thermal quenching can be neglected.

With ETU, ions in the upper state transfer energy via dipole-dipole interaction leading to excitation to higher energy levels with non-radiative relaxations back to the upper state therefore leading to increased heating. Although it has been mentioned previously in work related to Alexandrite [96] and its prominence in

Cr:Colquiriite lasers, there is no other mention in the literature. The effect observed in that work is likely to have been caused by ESA.

Similar to ETU, ESA occurs when an ion in the upper state is excited to higher states by a pump or laser photon that was intended for GSA or stimulated emission. The excited ion then rapidly decays non-radiatively back to the upper state adding further heat to the crystal and acting as an additional loss method. ESA is prominent in Alexandrite at both the pump and laser wavelengths [97]. Since ESA is both wavelength and temperature dependent it is important to carefully examine its spectroscopy and its effect on lasing performance.

3.3.2 Pump ESA

ESA at the pump wavelength was first measured in detail by Shand et al. by using a pulsed pump-probe to measure the difference in transmission with and without pumping [98]. Figure 3.8 shows the measured pump GSA (σ_0) and pump ESA (σ_1) for $E_{||}b$ across the visible wavelength range. Two samples were used at a crystal temperature of 20 °C.

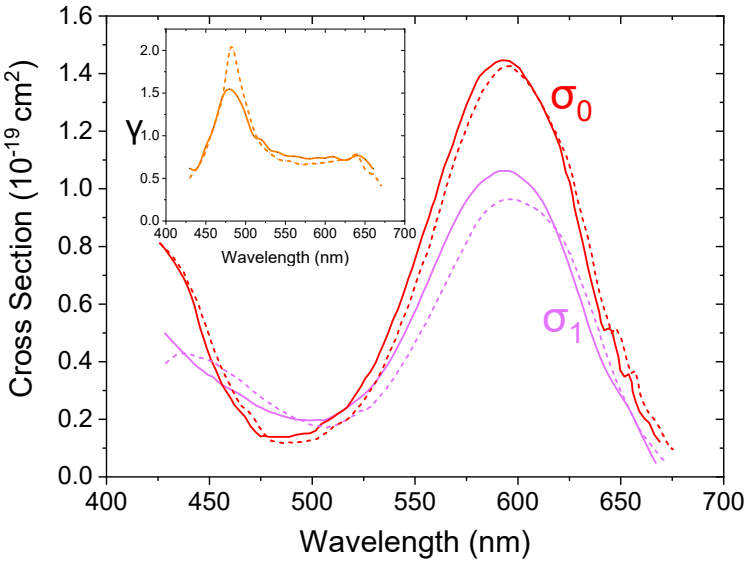

Figure 3.8: Pump GSA and ESA as a function of wavelength with $\gamma = \sigma_1/\sigma_0$ shown in inset for $E_{||}b$. Solid and dashed line represent two different samples. Figure adapted from [98].

It is often convenient to characterise pump ESA by using the ratio $\gamma = \sigma_1/\sigma_0$. The inset of Fig. 3.8 shows γ as a function of wavelength using the measured values

of pump GSA and ESA. The result indicates a high level of pump ESA across the entire visible region. In particular, at the blue-green region $\gamma > 1$ meaning that no population inversion can be achieved (at least for $E_{||}b$), though this is unsurprising given that the pump GSA is so low at this region. Around the peak of pump GSA (including 640 nm for red-diode pumping) $\gamma \approx 0.75$ which is rather significant and leads to an increased threshold, lower efficiency and increased heating [99]. The effect on heating will be discussed in greater detail later in Chapter 5. The temperature dependence of pump ESA was recently studied by Kerridge-Johns et al. and found that it could be reduced by increasing the temperature with $\gamma \approx 0.8$ at 10 °C reducing to $\gamma \approx 0.7$ at 90 °C [90].

3.3.3 Laser Emission, GSA and ESA

When discussing the spectroscopy at the lasing wavelength it is important to carefully distinguish the different processes that are in effect as they are co-dependent and vary with both wavelength and temperature. Figure 3.9 shows a schematic of the energy levels of Alexandrite, as shown in Fig. 3.4(c), but with all the possible transitions included for clarity.

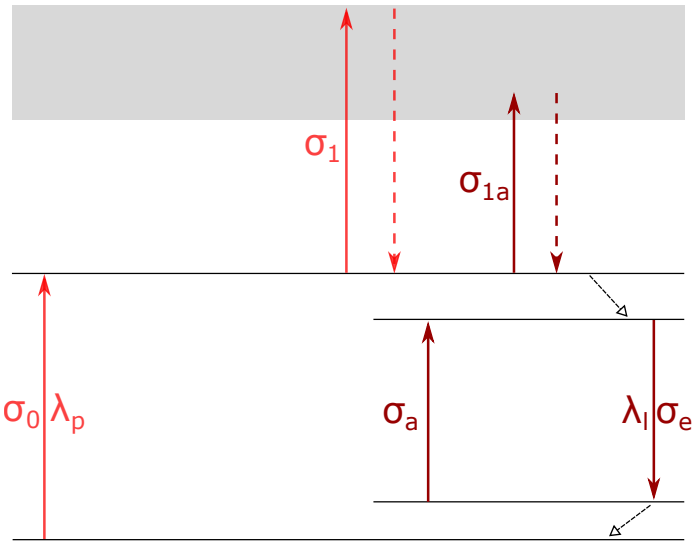

Figure 3.9: Schematic of the lasing energy levels of Cr^{3+} in Alexandrite with pump (λ_p) GSA and ESA, and laser (λ_l) stimulated emission, GSA and ESA. Grey region indicates higher energy levels and dashed lines indicate non-radiative decays.

The effective emission cross section, σ_e, defines the transition from the combined upper lasing level ($^4T_2$ and ^2E) to the ground level ($^4A_2$). It can be calculated from the fluorescence spectrum, fluorescence lifetime data and the extended McCumber theory - details of which can be found in [11]. Its spectral distribution at different temperatures has been calculated both by Shand et al. in 1983 [100] and also recently by Demirbas et al. with more results at higher temperatures [76]. Figure 3.10(a) shows the spectral distribution of σ_e at six different temperatures. At 25 °C, $\sigma_e \approx 0.7 \times 10^{-20}\,\mathrm{cm}^2$ at around 755 nm. The spectral distribution matches well to the fluorescence profile measured by Walling et al. and the values are consistent with those of Shand et al. at 28 °C. Above 25 °C, σ_e in general increases. This arises from the increased vibronic contribution due to the increasing thermal population of the $^4T_2$ band compared to the ^2E level, where the reduced R-line signal can also be observed.

Figure. 3.10(b) shows the theoretical spectral distribution of Laser GSA, σ_a, over the lasing region of Alexandrite. The theoretical expression modelled by Walling et al. [11] based on the extended McCumber theory is given by

$$\sigma_a(E,T) = \sigma_e(E,T)\, e^{-(E-E^*)/k_B T} \tag{3.5}$$

where E is the photon energy, E^* is the effective no-phonon energy, $k_B = 1.38 \times 10^{-23}\,\mathrm{m^2\,kg\,s^{-2}\,K^{-1}}$ is Boltzmann's constant and T is the temperature of the crystal. The effective no-phonon energy is the energy separation between the ground vibrational level of the $^4A_2$ state and the lowest filled state of the combined $^4T_2$ and ^2E upper lasing level. It is a temperature dependent quantity with a corresponding wavelength of 680.3 nm at 300 K and 682.7 nm at 375 K [11] - note that the values used in Fig. 3.5(b) have been extrapolated from these two values.

Laser GSA is effectively an extension of the pump GSA and so increases at shorter wavelengths. It also increases with temperature due to the increased thermal filling of the $^4A_2$ state. This gives rise to two effects, firstly Laser GSA sets the short wavelength lasing limit on Alexandrite by introducing an additional loss factor at around 700 nm. Secondly, it shifts the optimum wavelength for Alexandrite to longer wavelengths at higher temperatures. This can be seen clearer by considering the overall gain, but first the Laser ESA must also be taken into consideration.

Laser ESA is predominantly initiated from the $^4T_2$ level to higher energy levels. It too was measured by Shand et al. [100] by comparing the theoretical effective

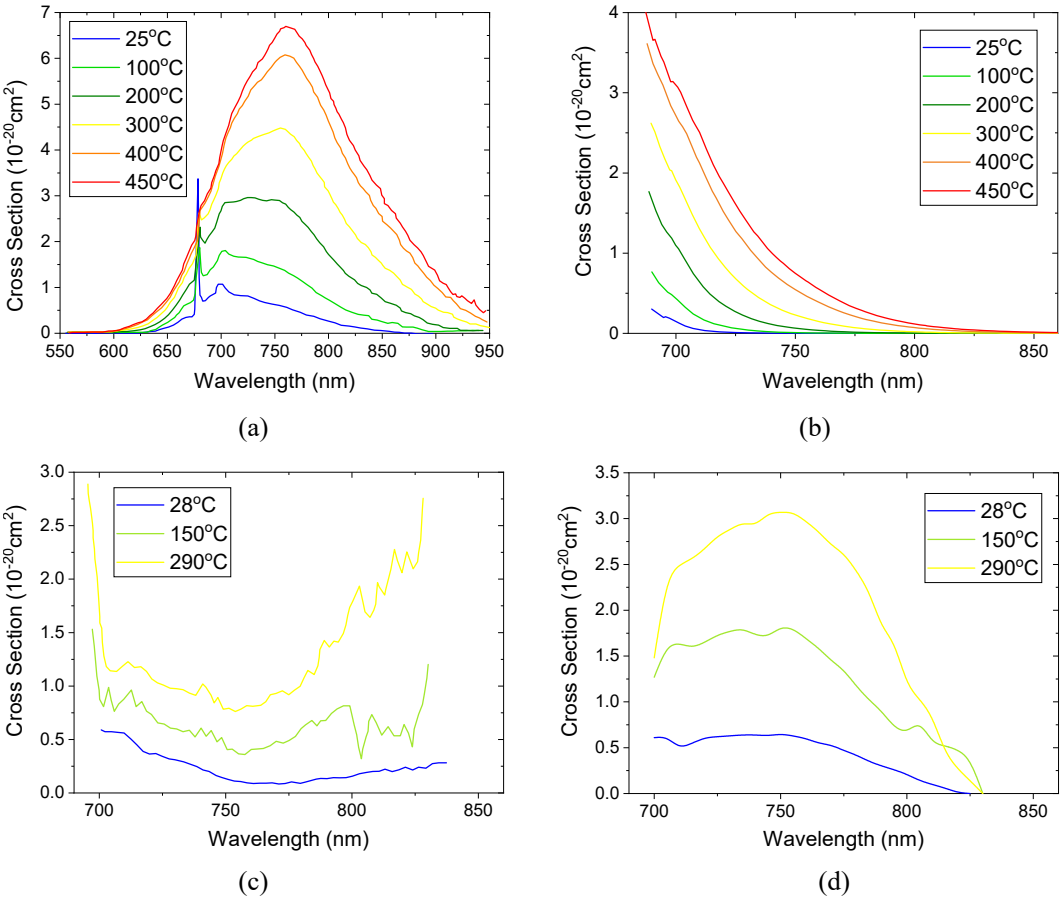

Figure 3.10: (a) Effective emission cross section at six temperatures. Image adpated from [76]. (b) Theoretical laser GSA cross section at six temperatures. (c) Laser ESA cross section at three temperatures. Image adapted from [100]. (d) Difference between effective emission and laser ESA cross section at three temperatures.

emission cross section and the measured effective emission cross section (details of the experimental procedure can be found in [100, 101]). Figure 3.10(c) shows the calculated laser ESA cross section, σ_{1a}, at temperatures of 28, 150 and 290 °C. As with the effective emission cross section, the laser ESA cross section increases with temperature due to the increased thermal filling of the $^4T_2$ level. Laser ESA plays a pivotal role in both the optimum wavelength and the long wavelength limit of Alexandrite lasers. This is best illustrated by considering the difference between the effective and ESA cross section, $\sigma_e^* = \sigma_e - \sigma_{1a}$.

Figure 3.10(d) shows the spectral distribution of σ_e^* at 28, 150 and 290 °C. By

comparing it to σ_e in Fig. 3.10(a) at 25, 150 and 300 °C the effects of laser ESA can be clearly seen. At room temperature the optimum wavelength is shifted to around 755 nm with a roughly constant profile. Increasing the temperature still corresponds to an increase in cross section and to an increase in the long wavelength lasing limit of Alexandrite which occurs at the point where laser ESA and effective emission cross sections are equal. Increasing laser ESA at shorter wavelengths also acts to reduced the cross section at shorter wavelengths.

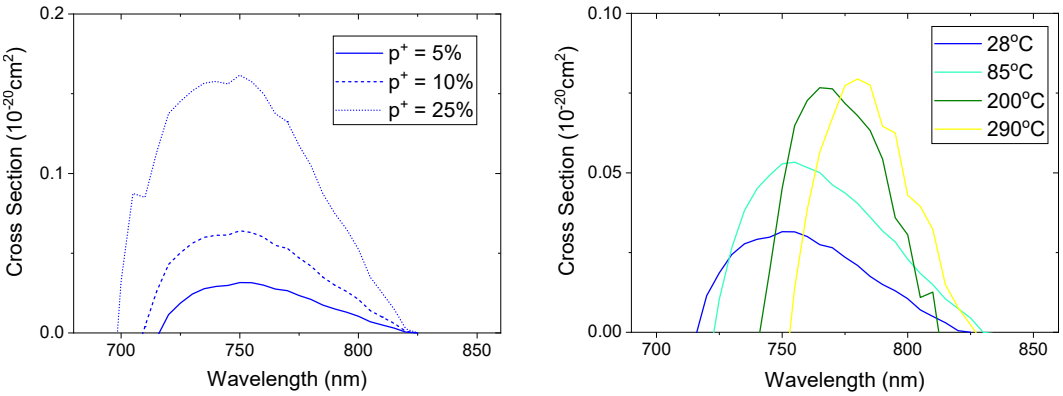

Figure 3.11: (a) Spectral distribution of $\sigma_t(E,T)$ at 28 °C. (b) Spectral distribution of $\sigma_t(E,T)$ at $\mathrm{p}^+ = 5\,\%$. Data from [100].

The total gain cross section, $\sigma_t(E,T)$, can be used to show the overall wavelength range and optimal wavelength for Alexandrite with all effects accounted for. It is expressed as

$$\sigma_t(E,T) = \mathrm{p}^+\sigma_e^*(E,T) - \left(1-\mathrm{p}^+\right)\sigma_a(E,T) \tag{3.6}$$

where p^+ is the fraction of laser inversion. Figure 3.11(a) shows the spectral distribution of $\sigma_t(E,T)$ at a fixed temperature of $T = 28$ °C with inversion level $\mathrm{p}^+ = 5$, 10 and 25 %. At an inversion level of $\mathrm{p}^+ = 5\,\%$ there is positive gain at around 720-820 nm with a peak at 750 nm. This matches relatively well with the experimetal wavelength tuning range obtained by Beyatli et al. [96] with a red-diode-pumped CW Alexandrite (0.2 at.% Cr-doping) laser which achieved a tuning range of 724-816 nm with an optimum wavelength of 755 nm at 25 °C. Losses from GSA can be minimised at higher inversion which was achieved by Walling et al. using flashlamp pumping and a low Cr-doping of 0.043 at.%. A tuning range of

701-816 nm was achieved, matching well to the higher inversion level cross section in Fig. 3.11(a).

Figure 3.11(b) shows $\sigma_t(E,T)$ at temperatures of 28, 85, 200 and 290 °C with $p^+ = 5\,\%$. With increased temperature $\sigma_t(E,T)$ shifts to longer wavelengths. The cross section at 85 °C matches relatively well to the tuning curve of 714-818 nm obtained at 60 °C by Kerridge-Johns et al. [90]. Laser operation beyond 830 nm requires very high temperature and high inversion. A long wavelength record of 858 nm was achieved with flashlamp pumping at 513 °C and >100 J of pumping [51]. The shift in wavelength with increased temperature has been recently demonstrated in diode-pumped systems by Yorulmaz et al. [65] where tuning curves were obtained at 25 °C (736-795 nm), 100 °C (745-810 nm) and 200 °C (776-823 nm).

3.4 Summary

This chapter has provided a thorough overview of the physical, lasing and spectroscopic properties of Alexandrite lasers. Alexandrite is a birefringent material with strong thermo-mechanical properties enabling high power continuous-wave operation. Its four-level vibronic lasing enable broad wavelength tuning at around 700-850 nm and a long fluorescence lifetime of around 240 µs at room temperature makes it suitable for high-energy Q-switched operation.

A variety of pump sources can be used due to the broad absorption spectrum across the visible region. Over the last decade the emergence of high power red-diode lasers has enabled high absorption and low quantum defect pumping of Alexandrite lasers. This in addition to the nominal benefits of low-cost, compactness and reliability from diode-pumping make red-diode-pumped Alexandrite lasers a highly promising wavelength tunable laser source with key examples shown in this chapter.

Despite the major advancement in Alexandrite laser technology, the output power of tunable Alexandrite lasers (with the exception of flashlamp-pumped systems) has been limited to <1 W. Power scaling requires careful consideration of the impact of pump-induced lensing and the cavity design required to provide high-power laser operation. This chapter has provided the fundamental groundwork of the birefringent wavelength tuning model of Alexandrite lasers covered in Chapter 4, the thermal lens model shown in Chapter 5 and the power-scaled tunable Alexandrite lasers in Chapters 6 and 7.

Chapter 4

Birefringent Tuning of Alexandrite Lasers

Tunable Alexandrite lasers have typically used birefringent filters (see for example [65, 90, 102]) or diffraction gratings [66] as wavelength selective devices. Birefringent filters have also been used in generating dual wavelength operation [103] which realises other applications such as THz generation. TEM_{00} operation with wavelength tuning is usually accomplished with the birefringent filter in an extended cavity with intra-cavity lenses or curved mirrors for mode size control. However, it is generally found that there is a significant loss of efficiency in extended cavities compared to compact cavities due to the insertion losses and the influence of thermal aberrations [102].

In this chapter a novel tuning method is demonstrated where the birefringent properties of Alexandrite are utilised by using the crystal itself as both the gain medium and the wavelength selective element in an ultra-compact cavity. This realises a simple, efficient and stable system providing both tunable and dual wavelength operation. This work has been published in Optics Express [104] and presented at Photonics West 2020 [105].

4.1 Experimental System

4.1.1 Fibre-coupled Diode Module

Figure 4.1 shows the pump delivery and laser cavity used in this experiment. The pump module was a 5 W-level fibre-coupled diode module which has been extensively

used in other work (e.g. [68, 90, 102]) as it offers a compact ($10 \times 20\,\mathrm{mm}^2$ module footprint) and low-cost pump-source. Fibre-coupling provides further flexibility in beam delivery and in ensuring a symmetrical beam profile. A collimator with a 35 mm focal length was used to collimate the fibre output to an output beam radius of around 7 mm.

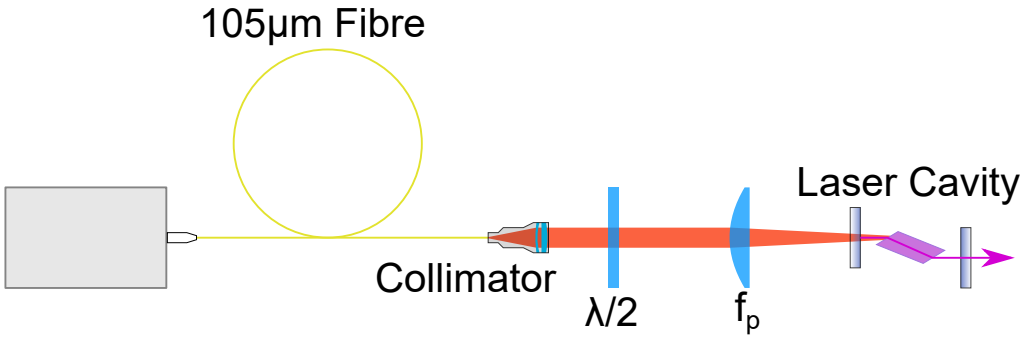

Figure 4.1: Pump delivery and laser cavity for tunable birefrigent Alexandrite laser.

The diode module was mounted onto a water-cooled copper heat sink for temperature control. Figure 4.2(a) shows the output power as a function of the drive current at 16, 20 and 25 °C. Reducing the temperature increased the output power and blue-shifted the wavelength, but also increased the risk of condensation on the emitters. Therefore to maximise the power but minimise any condensation, the temperature was fixed at 16 °C and not taken any lower. Figure 4.2(b) shows the wavelength as a function of current at 16 °C. At a maximum current of 0.75 A the total output power and wavelength were 5.9 W and 637.5 nm, respectively, with a linewidth (FWHM) of 1.2 nm. Information on the laser diagnostics used here and throughout the experimental work in this thesis can be found in Appendix A.

The pump polarisation and beam quality were also measured as they give an indication of the useful pump power. The polarisation was measured by measuring the maximum transmission through a cube polariser. It was found that the fraction of linear polarisation could be varied by adjusting the fibre configuration, however at best this was limited to 73 %. This suggests light from the linearly polarised diodes are partially rotated due to the multi-mode fibre. The beam quality was measured and found to be $M^2 = 50$ which is in line with that measured for this diode module in other work. At focus the pump intensity profile was roughly Gaussian, further verifying the partial spatial mixing in the fibre. Previous work has found a waist

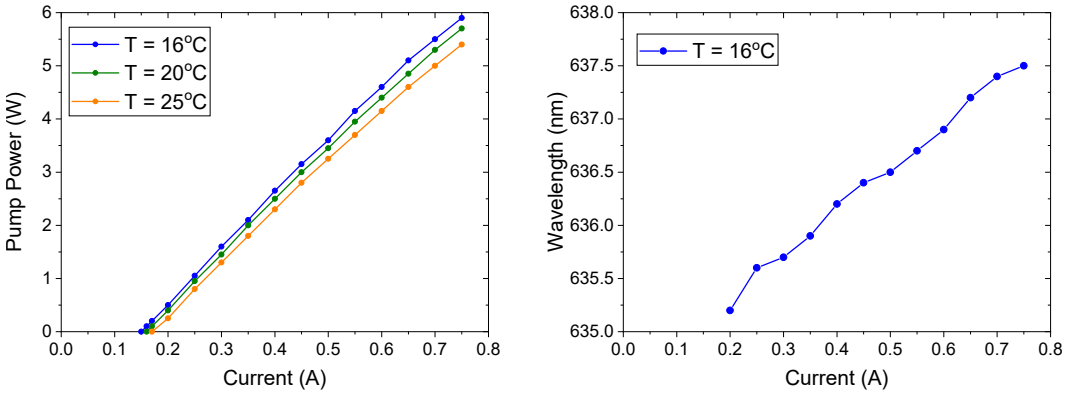

Figure 4.2: (a) Pump power as a function of drive current. (b) Pump wavelength as a function of drive current.

size of $w_p = 75\,\mu\text{m}$ and a Rayleigh range of around 1.0 mm as optimal for a compact cavity with Cr^{3+}-doping of ~ 0.2at.% [102]. Given the large beam size at the pump lens (~ 7 mm) this meant using an aspheric lens of focal length $f_p = 50$ mm.

4.1.2 Ultra-compact Diode-pumped Alexandrite Laser

Figure 4.3 shows a more detailed diagram of the laser cavity. The cavity is formed of an Alexandrite crystal, dichroic back mirror (BM) that was highly transmissive at the pump wavelength (~ 638 nm) and highly reflective at the laser wavelength (700-820 nm) and an output coupler (OC). The Alexandrite crystal is a Brewster-cut crystal. The cut is in the bc-plane, enabling low-loss transimission at the crystal surface for light polarised to the high gain b-axis. Cavity stability is provided with the onset of a pump-induced lens at the crystal. Given the compact size of the cavity any changes to the cavity stability can be assumed to be negligible.

The experiment was run twice using two crystals from different suppliers to check consistency. Table 4.1 shows an overview of the experimental system using Crystal 1 and Crystal 2. The optical path length of the cavity mode in both cases was ~ 24 mm. The Cr^{3+} concentration and output coupler reflectivity (R_{OC}) were chosen in line with that used in previous work where high efficiency operation was demonstrated [66, 102]. The crystals were mounted on copper-heatsinks with water cooling for temperature control. For Crystal 1 the temperature was set to $T = 50\,^{\circ}\text{C}$ since it roughly corresponds to the optimum temperature for continuous-wave

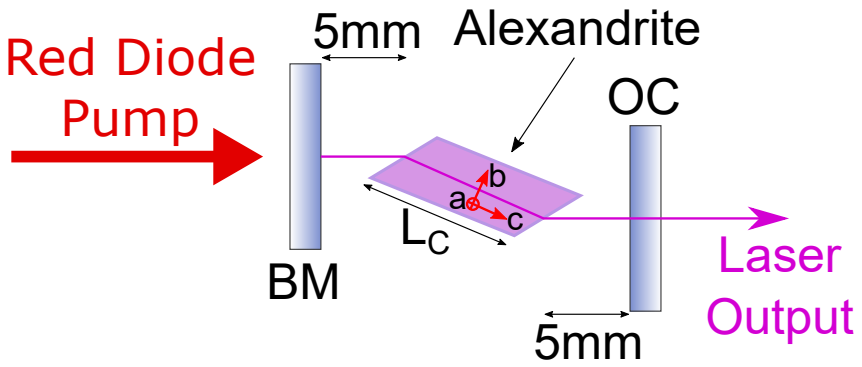

Figure 4.3: Ultra-compact Alexandrite laser cavity.

Alexandrite [90]. However, for Crystal 2 no secondary water chiller was initially available and so the same chiller was used for both the diode module and crystal and set to $T = 16\,^{\circ}\mathrm{C}$. Note that though both crystals had a nominal crystal length of $L_C = 8\,\mathrm{mm}$, manufacturing tolerances in the length and Brewster-cut angle mean that this value could be different in the two crystals.

Table 4.1: Overview of different cavity parameters.

	Dimensions	Cr^{3+} conc. (at.%)	R_{OC} (%)	T (°C)
Crystal 1	$4\,\mathrm{mm}\varnothing \times 8\,\mathrm{mm}$	0.22	99.0	50
Crystal 2	$4 \times 4 \times 8\,\mathrm{mm}$	0.24	99.5	16

At maximum drive current the crystal absorbed around 75 % of the total incident pump power which roughly corresponds to the major linearly polarised component that is rotated to the crystal b-axis using a halfwave plate (see Fig. 4.1), the remainder is either reflected off the surface or transmitted through the crystal. With the incident pump polarised using a cube polariser almost all (>99 %) of the pump power was absorbed.

Figure 4.4(a) shows the laser power as a function of the absorbed pump power for Crystal 1. At maximum pump power the output power was 1.03 W. The threshold and slope efficiency were 1.3 W and 36 %, respectively. The beam quality was measured to be $M^2 = 1.1$ in both directions though the beam was slightly elliptical due to the astigmatism caused by the Brewster cut crystal (see inset of Fig. 4.4(a)). The spectrum had a main peak at $\sim 758\,\mathrm{nm}$ with additional smaller peaks separated by around 1-1.5 nm with an overall linewidth of $\sim 5\,\mathrm{nm}$.

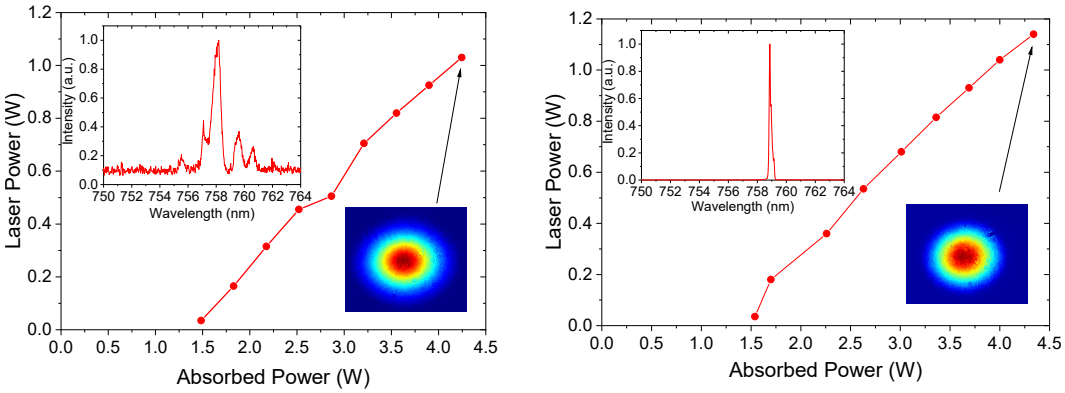

Figure 4.4: Laser power as a function of absorbed pump power for: (a) Crystal 1 (b) Crystal 2

Crystal 2 performed marginally better, as shown in Fig. 4.4(b). The maximum output power was 1.14 W, and the threshold and slope efficiency were 1.5 W and 39 %, respectively. The output spatial mode was similar to that of Crystal 1 with $M^2 = 1.1$. The laser operated at a wavelength of 758.9 nm with a single peak with spectral width limited by the resolving power of the spectrometer (~ 0.2 nm).

The results for both crystals are comparable to that achieved in previous work using a similar pump diode module but with an AR-coated cylindrical rod in a compact cavity. Arbabzadah et al. demonstrated a maximum output power and slope efficiency of 1 W and 44.2 %, respectively [102]. Later Kerridge-Johns et al. obtained up to 1.2 W with a 54 % slope efficiency [90], therefore suggesting that even higher efficiencies can be obtained in this system, however since the primary interest here is in developing a compact tunable source no further optimising was made.

Birefringent wavelength tuning was obtained by tilting the Brewster-cut Alexandrite crystal. A simple analysis of this tuning method can be made by considering the beam travelling through the crystal. Due to the birefringent properties of Alexandrite, there are two refractive indices associated to two orthogonal polarisation states. The phase difference between the two states is given by

$$\Delta\phi = \frac{2\pi}{\lambda}\Delta n L \tag{4.1}$$

where λ is the laser wavelength, Δn is the difference between the two refractive indices (not neccessarily the principal refractive indicies) and L is the geometrical

path length travelled in the crystal. The condition for low-loss of the crystal in the laser cavity is for its birefringence to act as a full waveplate, i.e.

$$\Delta\phi = 2\pi m \tag{4.2}$$

where m is an integer. Substituting for $\Delta\phi$ in Eqs. (4.1) and (4.2) gives the wavelengths at low-loss transmission

$$\lambda_m = \frac{\Delta nL}{m}. \tag{4.3}$$

The separation of the wavelengths ($\Delta m = \pm 1$) is the free-spectral-range (FSR) which is approximately given by

$$\Delta\lambda_{\mathrm{FSR}} = \frac{\lambda^2}{\Delta nL}. \tag{4.4}$$

Therefore, according to Eq. (4.3) changing L and Δn by tilting the crystal provides wavelength tunability provided m is unchanged. When m changes dual wavelength operation is possible as the low-loss transmission wavelengths are accessing regions of equal gain. The separation of the dual-wavelengths is given by Eq. (4.4). Further detail on the theory of birefringent wavelength tuning will be provided later in Section 4.3.

4.2 Birefringent Wavelength Tuning Results

4.2.1 Angle Tuning

Wavelength tuning was obtained by tilting the Brewster-cut crystal with the cavity mirrors fixed. This was done in two ways, as shown schematically in Fig. 4.5. Firstly by varying the horizontal angle of incidence, θ_H, with fixed vertical angle of incidence, $\theta_V = 0°$, as shown in the upper image. Secondly, as shown in the lower image, the vertical angle of incidence, θ_V, was varied with the horizontal angle of incidence fixed at Brewster's angle $\theta_H = \theta_B$.

Figures 4.6 and 4.7 show the measured wavelength and laser power as a function of the angle of incidence for Crystal 1 and Crystal 2, respectively. Tuning the horizontal angle of incidence (Figs. 4.6(a) and 4.7(a)) away from Brewster's angle ($\theta_H = \theta_B$) with fixed vertical angle of incidence ($\theta_V = 0°$) provided a roughly linear change in wavelength with respect to the horizontal angle of incidence. A blue-shift

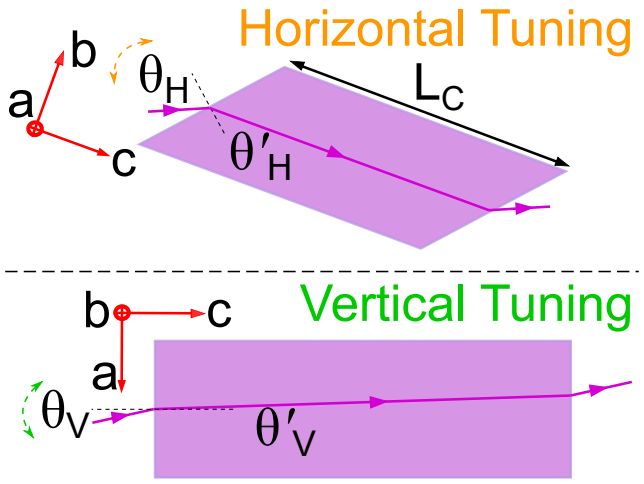

Figure 4.5: Tilting the Alexandrite crystal with horizontal tuning and vertical tuning.

in wavelength was obtained with a decreased horizontal angle of incidence and a red-shift in wavelength with an increased angle. Tunable operation was maintained until dual wavelength operation (indicated by yellow region) with a peak-to-peak separation of around 12 nm for Crystal 1 and 13 nm for Crystal 2. The dual wavelength regions are where the two low loss transmissions (λ_m and λ_{m+1} or λ_{m-1}) coincide with regions of equal gain. Changing the horizontal angle of incidence further shifted the transmission such that the new wavelength (λ_{m+1} or λ_{m-1}) occupied the region of higher gain. The maximum continuous tuning range obtained was from 746 to 768 nm (Fig. 4.7(a)).

The corresponding laser power is shown in Figs. 4.6 and 4.7 for Crystal 1 and Crystal 2, respectively. Near Brewster's angle the laser power is relatively unchanged at around 1 W. Larger changes to the angle leads to a reduction in the laser power due to the increased loss from the Brewster surface. Despite this, over the maximum tuning range of 746-768 nm the laser power remained over 0.1 W and the maximum dual wavelength power was 0.89 W.

Varying the vertical angle of incidence (Figs. 4.6(b) and 4.7(b)), with fixed horizontal angle of incidence $\theta_H = \theta_B$, increased the wavelength roughly quadratically. The laser power as a function of vertical angle of incidence is shown in Figs. 4.6 and 4.7. Wavelength tuning from around 758 nm to 764 nm for Crystal 1 and to 766 nm for Crystal 2 was obtained with > 0.6 W of output power. Dual wavelength operation was obtained at around $\theta_V = 9-10°$ and then single wavelength operation

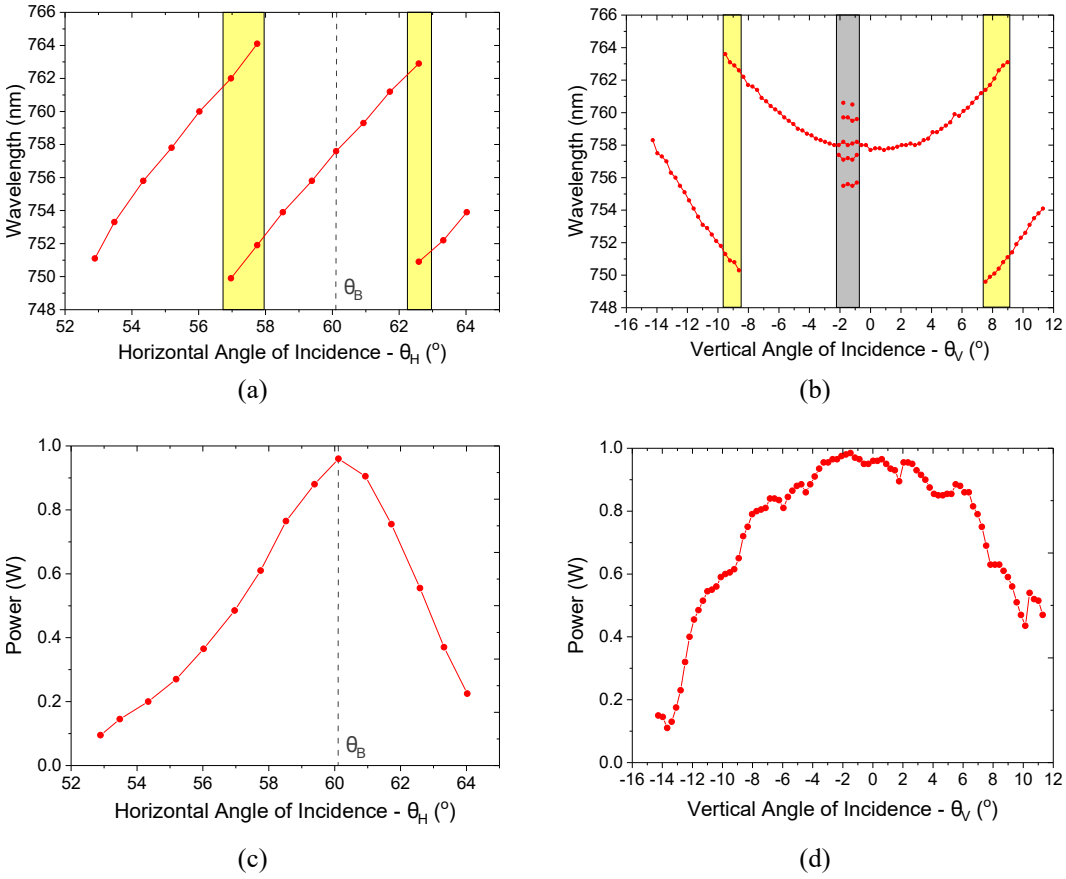

Figure 4.6: Tuning results for Crystal 1: (a) Measured wavelength as a function of horizontal angle of incidence. (b) Measured wavelength as a function of vertical angle of incidence. Yellow region denotes region where dual wavelength operation occurred. Grey region denotes region where spectrum was modulated. (c) Power as a function of horizontal angle of incidence. (d) Power as a function of vertical angle of incidence.

at $\sim 750\,\text{nm}$ at a larger vertical angle of incidence.

The wavelength tuning range was primarily limited by the FSR of the crystal and hence for Crystal 1 the tuning range was limited to around 750-764 nm with the peak of the gain curve at around 758 nm. For Crystal 1, the range of tuning was mainly limited by the tilting range of the crystal mount except at negative θ_V where losses exceeded the gain. The tilting range was improved for Crystal 2. This provided an additional tuning order to be obtained with tilting in the horizontal

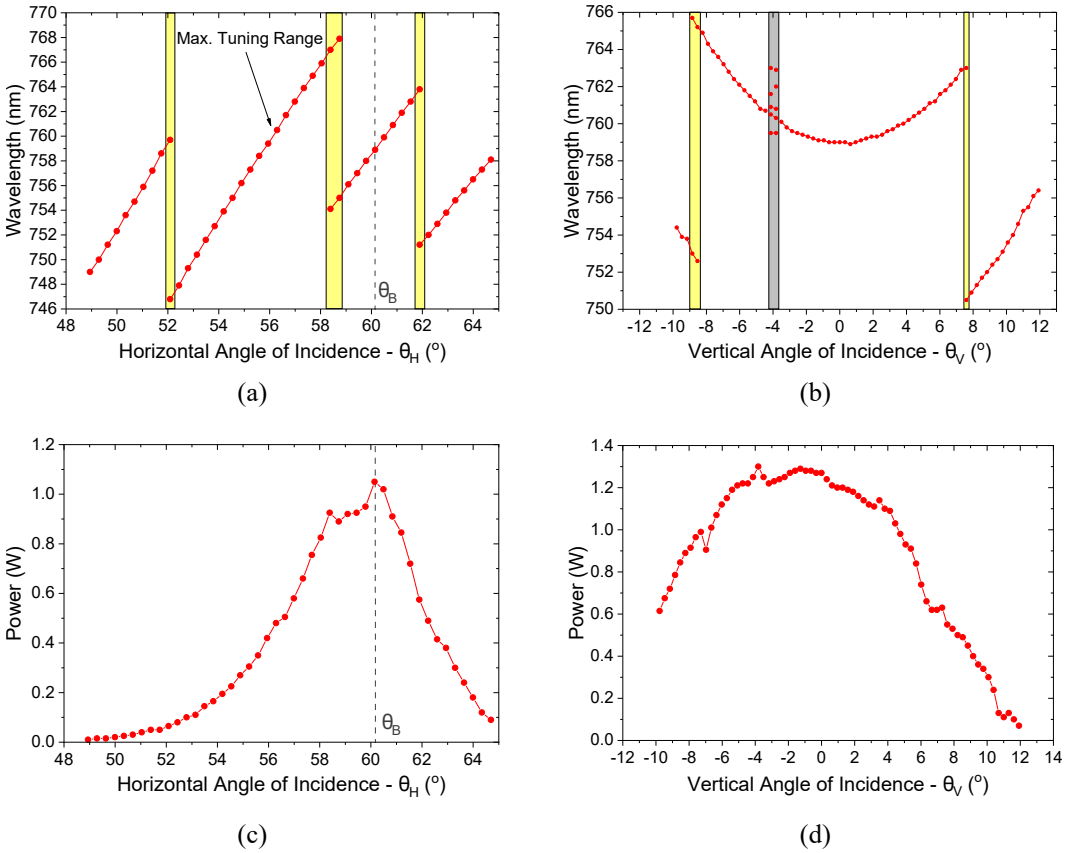

Figure 4.7: Tuning results for Crystal 2: (a) Measured wavelength as a function of horizontal angle of incidence. (b) Measured wavelength as a function of vertical angle of incidence. Yellow region denotes region where dual wavelength operation occurred. Grey region denotes region where spectrum was modulated. (c) Power as a function of horizontal angle of incidence. (d) Power as a function of vertical angle of incidence

plane. Only tilting in negative θ_V was limited by the actual mount. Whereas the tuning orders for Crystal 1 are relatively unchanged in terms of wavelength range the same is not the case for Crystal 2. For example, the maximum tuning range does not stop at 754 nm, but instead shifts down to 746 nm. This suggests that the gain at this region is now higher than at longer wavelengths. The cause of this is not immediately clear but illustrates the complex gain dynamics of Alexandrite with the gain of Alexandrite changing due to the dependence on the crystal temperature (which may be lowered due to the higher reflecting pump) or laser inversion level

due to the increased reflection loss.

Figure 4.8 shows some examples of the measured wavelength spectrum. The spectrum was measured by directly coupling a low powered leakage beam from an external mirror onto a fibre-coupled grating spectrometer. This provided an effective way to measure the central wavelength but with limited information on the spectral linewidth. Figure 4.8(a) shows the spectrum at $\theta_H = \theta_B$ and $\theta_V = 0°$ for Crystal 2 where the central wavelength was measured to be $\lambda = 758.9\,\text{nm}$. The linewidth was measured using a free-space Fabry-Perot (FP) etalon with a FSR of 50 GHz. The low power leakage beam was coupled into the FP etalon via a negative lens of focal length $f_- = -50\,\text{mm}$ and then focused with a positive lens of focal length $f_+ = 150\,\text{mm}$ onto a CMOS camera (this technique was repeated throughout this thesis and further information can be found in Appendix A). This produces a series of maxima circular patterns for each longitudinal mode that is then repeated at larger radii with the separation of each group of maxima related to the FSR of the FP etalon. Knowing the longitudinal-mode-spacing allows the linewidth (width of all the longitudinal modes) to be determined. The inset in Fig. 4.8(a) shows the interference pattern measured on the CMOS camera with five longitudinal modes clearly visible. Given the longitudinal-mode-spacing to be around 6.5 GHz gives an overall linewidth of $\sim 15\,\text{GHz}$ - a good result for a compact cavity without any other wavelength selective devices or stabilisation.

The laser spectrum and linewidth were measured at other angles of incidences. Figure 4.8(b) shows the laser spectra at $\theta_V = 0°$ and with θ_H varying from 52.1° to 58.7° which corresponds to the maximum tuning range. The results show the relative intensity of the spectra compared to that at $\theta_H = 58.4°$ where the power was 0.93 W. The dual wavelength regions are also indicated here by the yellow region but with the secondary peak omitted. Across the entire tuning range the spectrum was narrow with around 4-5 longitudinal modes visible and with the linewidth relatively constant at around 15 GHz.

Figures 4.8(c) and 4.8(d) show the wavelength spectra at dual wavelength operation for Crystal 1 (at $\theta_H = \theta_B$ and $\theta_V = 8.3°$) and Crystal 2 (at $\theta_H = 52.1°$ and $\theta_V = 0°$), respectively. The laser operated well in dual wavelength operation with little variation in the relative intensity of the two peaks. Equal intensity for the two peaks was also easily obtainable with careful control of the crystal tilt. Despite both crystals having the same nominal length of $L_C = 8\,\text{mm}$ the peak-to-peak separation at dual wavelength operation was different for the two crystals with around 12 nm

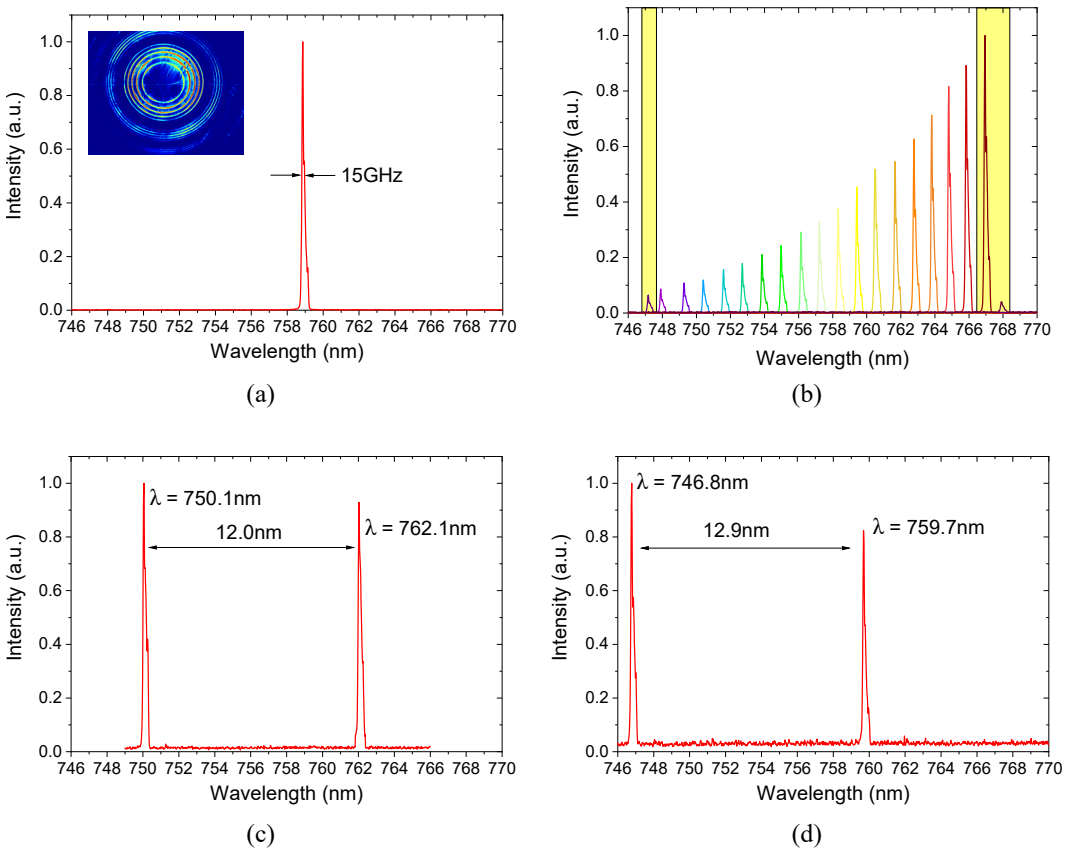

Figure 4.8: (a) Spectra at single wavelength operation for Crystal 2. Inset shows measured Fabry-Perot interference pattern. (b) Superposition of spectra measured over maximum tuning range. Yellow region indicates dual wavelength region where secondary peak has been omitted. (c) Dual wavelength spectra for Crystal 1. (d) Dual wavelength spectra for Crystal 2.

and 13 nm measured for Crystal 1 and Crystal 2, respectively at all dual wavelength regions.

A broad and modulated spectrum (similar to the spectrum in the inset of Fig. 4.4(a)) was observed for both crystals when tuning the vertical angle of incidence, as indicated by the grey region in Figs. 4.6(b) and 4.7(b). Temporal measurements of the laser output showed that the laser was self-Q-switching at this tuning region with a pulse duration of $<1\,\mu s$ at $>100\,kHz$ repetition rate. Since the focus of this chapter is on the birefringent wavelength tuning, further details of the results and mechanism of the self-Q-switching will be provided in chapter 5.

4.2.2 Temperature Tuning

The temperature dependence of the wavelength was also investigated for both crystals. Figure 4.9 shows the laser wavelength as a function of crystal temperature at $\theta_V = 0°$ and $\theta_H = \theta_B$ for the two crystals. In both cases it was found that the laser wavelength gradually blue-shifted with increasing temperature at a rate of around $-0.07\,\mathrm{nm\,K^{-1}}$ but with an overall shift (comparing minimum and maximum temperature) towards longer wavelengths. Dual-wavelength operation was obtained at 10-16 °C for Crystal 1 and at 28-30 °C for Crystal 2. Elsewhere single-wavelength operation occurred with a spectrum similar to that obtained with angular tuning (see Fig. 4.8(a)). Therefore, temperature tuning provides an additional control of the laser wavelength but with finer precision.

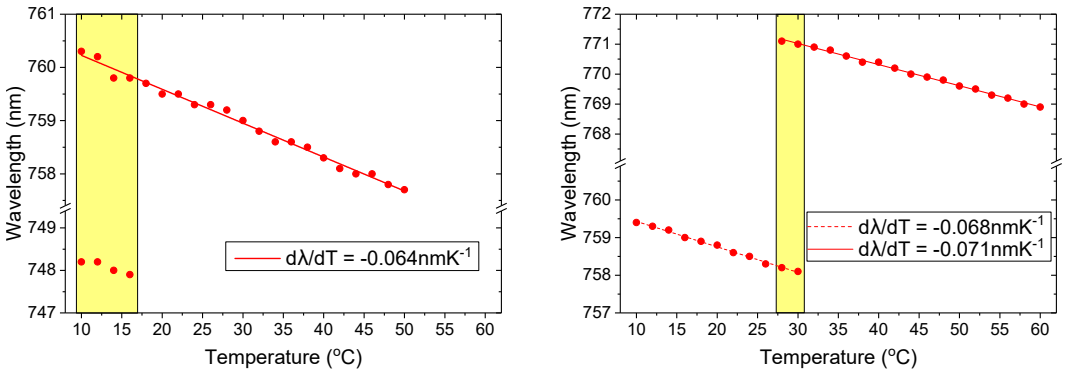

Figure 4.9: Temperature tuning of wavelength for: (a) Crystal 1 (b) Crystal 2.

This effect has been previously observed by Yorulmaz et al. where the laser wavelength was measured between 25 °C and 200 °C [65]. They found an overall red-shift with increased temperature but at discrete steps of around 10 nm and with a gradual blue-shift in wavelength also observed. The blue-shift effect was attributed to the crystal acting as a wavelength filter due to a temperature dependent refractive index which is not strictly true as the birefringent effect is always present regardless of the change in temperature. The crystal does act as a wavelength filter, as shown in this work, and its FSR is determined by its length (see Eq. (4.4)). The blue-shift in wavelength is due to the temperature dependence of the refractive index. A simple analysis can be made by taking the derivative of Eq. (4.3) with respect to temperature

$$\frac{d\lambda_m}{dT} = \frac{L}{m}\frac{d\Delta n}{dT} + \frac{\Delta n}{m}\frac{dL}{dT}. \tag{4.5}$$

Substituting for m using Eq. (4.3) and rearring gives

$$\frac{\Delta n L}{\lambda_m}\frac{d\lambda_m}{dT} = L\frac{d\Delta n}{dT} + \Delta n\frac{dL}{dT}. \tag{4.6}$$

The change in path length with respect to temperature can be written in terms of the expansion coefficient, α_T, according to $dL/dT = \alpha_T L$. Substituting this expression and rearranging in terms of the temperature dependence of the refractive index difference gives

$$\frac{d\Delta n}{dT} = \Delta n\left(\frac{1}{\lambda_m}\frac{d\lambda_m}{dT} - \alpha_T\right). \tag{4.7}$$

At $\theta_V = 0°$ and $\theta_H = \theta_B$, $\Delta n \approx \Delta n_{ba} = 0.0055$. Setting $\lambda_m = 755\,\text{nm}$, $d\lambda_m/dT = -0.07\,\text{nm}\,\text{K}^{-1}$ and $\alpha_T = 6 \times 10^{-6}\,\text{K}^{-1}$ [11] gives a value of $d\Delta n_{ba}/dT = -0.6 \times 10^{-6}\,\text{K}^{-1}$ which is consistent with a value of $-1.1 \times 10^{-6}\,\text{K}^{-1}$ measured by Walling et al. at 1150 nm [12]. However, the dispersion formula of Loiko et al. gives a positive value of $+1.0 \times 10^{-6}\,\text{K}^{-1}$ at 750 nm [82]. Given that it also disagrees with Walling's value in sign suggests there may be an additional refractive index component giving rise to the difference between the sign of the values obtained.

4.3 Birefingent Tuning Theoretical Model

To gain insight into the basic underlying mechanism as well as providing validation of the wavelength tuning and dual wavelength operation the wavelength selection can be modelled on the geometry of the crystal and its birefringence. Furthermore, by understanding the key parameters and their effect on the tuning range and dual wavelength separation it can provide a guide for future work, and in general to any other tunable birefringent gain medium.

4.3.1 Wavelength Selection

Figure 4.10 shows a detailed schematic of the parameters of the crystal and of Alexandrite that are necessary in describing the wavelength selection in this model. For a Brewster-cut crystal the physical path length travelled when at an angle θ'_H

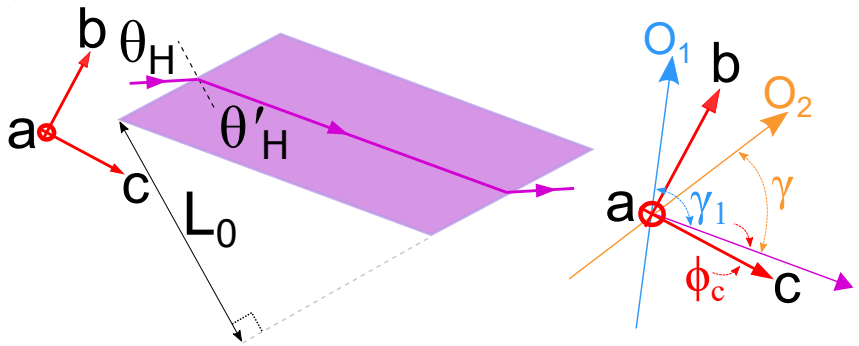

Figure 4.10: Birefringent tuning model. Angles between beam direction and optics axes and c-axis are shown.

in the horizontal plane (bc-plane) and θ'_V in vertical plane (ac-plane), where the angles are with respect to the surface normal, is given by

$$L = \frac{L_0}{\cos\theta'_H \cos\theta'_V}, \tag{4.8}$$

where L_0 is the perpendicular distance between the two end-face surfaces (see Fig. 4.10). For a birefringent material Δn is given by [89]

$$\Delta n = (n_b - n_c)\sin\gamma_1 \sin\gamma_2 = \Delta n_{bc} \sin\gamma_1 \sin\gamma_2, \tag{4.9}$$

where γ_1 and γ_2 are the angles between the beam propagation and the optic axes O_1 and O_2, respectively. Substituting Eqs. (4.8) and (4.9) into Eq. (4.3) gives

$$\lambda_m = \frac{\Delta n_{bc} L_0}{m} \frac{\sin\gamma_1 \sin\gamma_2}{\cos\theta'_H \cos\theta'_V}. \tag{4.10}$$

For a perfectly cut crystal at optimal conditions, the laser operates at Brewster's angle in the horizontal plane, $\theta_H = \theta_B = \tan^{-1} n_b = 60.1°$, and at normal incidence in the vertical plane, $\theta_V = 0°$. The beam travels along the c-axis, therefore, $\gamma_1 = \gamma_b + 90°$ and $\gamma_2 = \gamma_c$. Using Eq. (4.10), the wavelength under optimal conditions, λ_{m_0}, is given by

$$\lambda_{m_0} = \frac{\Delta n_{bc} L_0}{m} \frac{\cos\gamma_b^2}{\cos\theta'_B} \tag{4.11}$$

which reduces to $\lambda_{m_0} = \Delta n_{ba} L_C / m$ since $L_0/\cos\theta'_B = L_C$ and $\Delta n_{bc}\cos\gamma_b^2 = n_b - n_a$. By substituting for m in Eqs. (4.10) and (4.11) (provided m is unchanged)

λ_m can be expressed in terms of λ_{m_0}

$$\lambda_m\left(\theta'_H,\theta'_V\right)=\lambda_{m_0}\left(\frac{\cos\theta'_B}{\cos\theta'_H\cos\theta'_V}\right)\left(\frac{\sin\gamma_1\sin\gamma_2}{\cos^2\gamma_b}\right). \tag{4.12}$$

The first bracketed term in Eq. (4.12) represents the fractional change in wavelength due to the change in the geometrical path length. The second term, which depends on the angle between the beam and the optic axes represents the fractional change in the refractive index difference.

Equation (4.12) can be simplified further by considering changes in the horizontal angle of incidence, θ_H, with a fixed vertical angle of incidence $\theta_V = 0°$. In this case $\gamma_1 = \gamma_c - \phi_c$ and $\gamma_2 = \gamma_b + \pi/2 - \phi_c$ where ϕ_c is the angle between the beam direction and the c-axis in the horizontal plane (see Fig. 4.10). The wavelength for horizontal tuning is therefore given by

$$\lambda_m\left(\theta'_H\right)=\lambda_{m_0}\left(\frac{\cos\theta'_B}{\cos\theta'_H}\right)\left(\frac{\cos\left(\gamma_b+\phi_c\right)\cos\left(\gamma_b-\phi_c\right)}{\cos^2\gamma_b}\right). \tag{4.13}$$

For vertical tuning the relationship between γ_1, γ_2 and θ'_V is slightly more complex: $\cos\gamma_1 = \cos\theta'_V\cos\gamma_c$ and $\cos\gamma_2 = \cos\theta'_V\cos\left(\gamma_b+\pi/2\right)$. With these changes the wavelength as a function of the vertical angle of incidence with the horizontal angle of incidence fixed at $\theta_H = \theta_B$ is given by

$$\lambda_m\left(\theta'_V\right)=\lambda_{m_0}\left(\frac{1}{\cos\theta'_V}\right)\left(\frac{1-\cos^2\theta'_V\cos^2\gamma_c}{\cos^2\gamma_b}\right). \tag{4.14}$$

Wavelength tuning is limited by the FSR of the crystal at which point dual wavelength operation occurs. Substituting Eqs. (4.8) and (4.9) into Eq. (4.4) gives

$$\Delta\lambda_{\mathrm{FSR}}\approx\frac{\lambda_m^2}{\Delta n_{bc}L_0}\frac{\cos\theta'_V\cos\theta'_H}{\sin\gamma_1\sin\gamma_2}. \tag{4.15}$$

4.3.2 Model Comparison to Experimental Results

The theoretical equations describing the wavelength as a function of angle of incidence can be compared to the experimental results by shifting the tuning orders. Figure 4.11(a) shows the measured wavelength (dotted green, red and orange lines) as a function of the horizontal angle of incidence for Crystal 1 except with the $m+1$ and $m-1$ orders shifted by $+12\,\mathrm{nm}$ and $-12\,\mathrm{nm}$, respectively, which corresponds to the measured FSR. The theoretical wavelength (shown in blue) is calculated using

Eq. (4.13) with $\lambda_0 = 758.0\,\text{nm}$. Good agreement is obtained between the theory and the experiment with some deviation at larger angles that may be due to unwanted changes in the vertical angle of incidence.

Figure 4.11(b) shows the measured and theoretical wavelength as a function of the vertical angle of incidence for Crystal 1. The measured wavelength is the same as that shown in Fig. 4.6(b) with the order m unchanged (dotted red line) and the order $m+1$ shifted by $+12\,\text{nm}$ (dotted orange line). The theoretical wavelength is calculated using Eq. (4.14) with $\lambda_0 = 758.0\,\text{nm}$ and shows excellent agreement with the measured result.

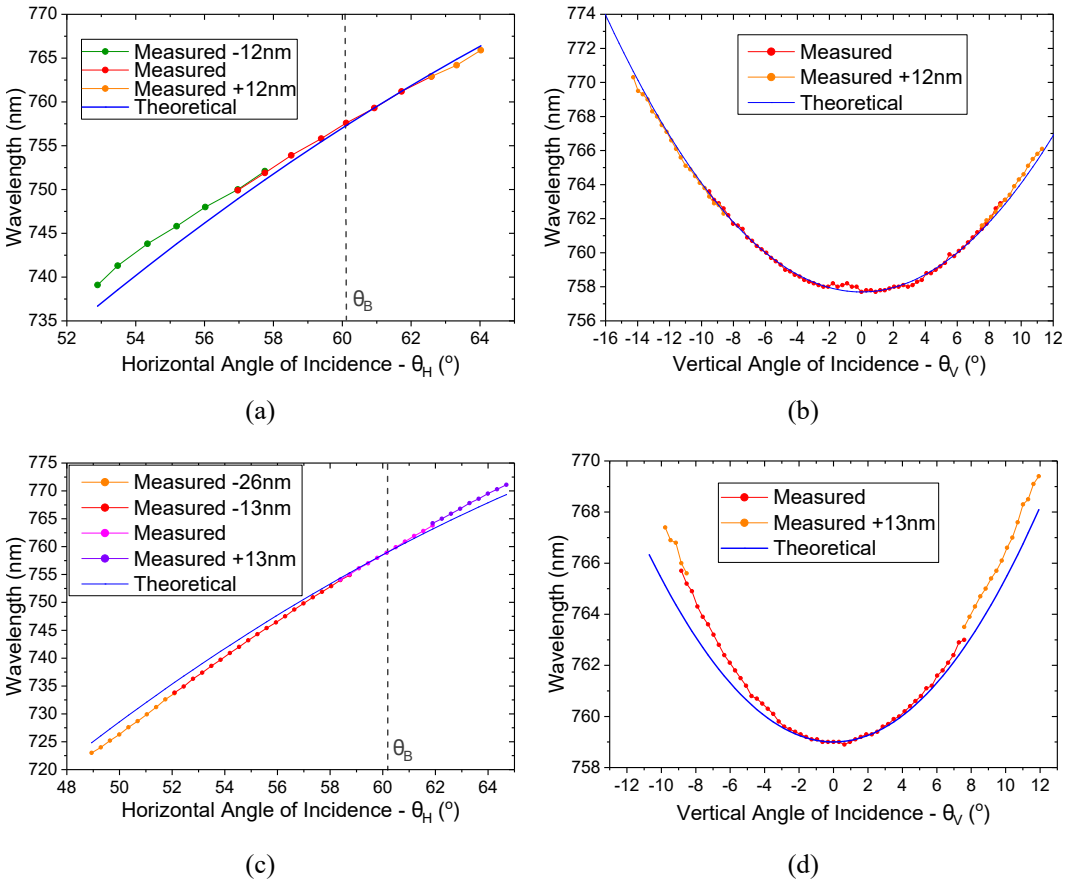

Figure 4.11: Comparison of measured and theoretical wavelength for Crystal 1: (a) and (b); and for Crystal 2: (c) and (d).

The measured and theoretical results for Crystal 2 are shown in Figs. 4.11(c) and 4.11(d) with $\lambda_0 = 758.9\,\text{nm}$ used in the theoretical equations. These too show good agreement between the measured and theoretical results with a slight difference at

the tuning extremes.

Figure 4.11(c) demonstrates the potential wide tuning range of around 723-771 nm were it not limited by the FSR of the crystal. The FSR of the crystal, given previously by Eq. (4.15), is inversely proportional to L_C. Therefore broad tuning of this extent could be achieved with a sufficiently short crystal ($L_C \sim 2\,\text{mm}$). Equation (4.15) can be used to determine L_C using the measured FSR. Using $\Delta\lambda_{\text{FSR}} = 12\,\text{nm}$ gives a length of around $L_C \approx 8.5\,\text{mm}$ for Crystal 1 and with $\Delta\lambda_{\text{FSR}} = 13\,\text{nm}$, $L_C \approx 8.0\,\text{mm}$ for Crystal 2. Both results are consistent with the manufacturers quoted length of 8 mm when accounting for the tolerance in manufacturing and post-processing such as end-face polishing.

4.4 Summary

In this chapter a novel and alternative wavelength tuning method has been experimentally demonstrated, modelled and analysed. A continuously wavelength tunable and dual wavelength red-diode-pumped Alexandrite laser formed of a plane-plane cavity and a Brewster-cut Alexandrite crystal has been shown. Two crystals were investigated to ensure consistency with both demonstrating similar results. With the first crystal, tuning between 750 nm and 764 nm with a linewidth of $\sim 15\,\text{GHz}$ was obtained by tilting the crystal inside the cavity. Temperature tuning provided finer wavelength tuning at a rate of $-0.07\,\text{nm}\,\text{K}^{-1}$. Stable dual wavelength emission was also obtained with a peak-to-peak separation 12 nm - corresponding to the FSR of the crystal. All results were obtained with an excellent TEM_{00} mode profile. Similar results were obtained with the second crystal including a broader continuous tuning range of 747-768 nm as well as dual wavelength operation with a 13 nm at up to 0.9 W of output power.

The theoretical model was found to be in good agreement with the wavelength tuning results and dual wavelength separation. The wavelength tuning and dual wavelength operation reported in this work are not limited to Alexandrite and can be applied to other birefringent gain media. The theoretical model is general for any biaxial material and only needs small adaptation for uniaxial material. The analytical expressions can then be used to determine the wavelength and free spectral range given the material properties, in particular with shorter crystal length giving a wider tuning range.

Chapter 5

Thermal and Population lensing in Alexandrite Lasers

Power scaling and maintaining TEM_{00} spatial quality in solid-state lasers is primarily limited by pump-induced lensing and refractive index aberration effects. Understanding, measuring and theoretical modelling of pump-induced lensing effects in diode-pumped solid-states are essential in designing high efficiency laser resonators with TEM_{00} beam quality at high pump power [5, 106].

The depositing of energy in the gain medium due to the quantum defect between the pump and laser wavelengths is the primary lensing effect in solid-state material. Analytical expressions for the lens power as a function of the pump power can be obtained by solving the heat diffusion equation under various simplifications [5, 106–108]. Experimental methods based on a number of techniques have been used to directly measure the pump-induced lens including passing a probe beam through the gain medium and finding its focus distance [109]; mode size measurement combined with cavity ABCD analysis [110]; and wavefront analysis using Shack-Hartmann wavefront sensors [111].

For the power-scaling development of Alexandrite lasers, fundamental understanding of the underlying mechanisms and the material properties relevant to pump-induced lensing and aberration effects are of significant importance. Up till now however, there had been only one study of the pump-induced lensing effects in a green-laser-pumped Alexandrite laser by Loiko et al. [82]. In that study the lensing was calculated based on indirect ABCD propagation analysis with a number of simplified assumptions without a detailed consideration of the underlying mechanism

or any prediction that could be used in other work.

This chapter provides an in-depth study of pump-induced lensing effects in diode-pumped Alexandrite lasers for the very first time. This includes direct wavefront measurement of the Alexandrite crystal using a Shack-Hartmann wavefront sensor (SH-WFS) which provides accurate and direct 2D mapping of the pump-induced refractive index change to determine the lens dioptric power. This removes any indirect interpretation, provides high measurement sensitivity ($\sim 1/100$th wavelength) as well as providing information on the lensing aberration. Furthermore, it enables measurement of the lens dioptric power under both lasing and non-lasing conditions.

The key results of this chapter are: that under non-lasing conditions the measured dioptric power is found to be linear with respect to the absorbed pump power - contrary to that expected theoretically due to the nonlinear excited state absorption heating factor which should lead to a non-linear dependency; the dioptric power is up to 60 % weaker under lasing conditions; and that an analytical model based on a combined thermal lens and a population lens (arising from difference in polarizability of excited and ground state) gives both a qualitative explanation of the pump power dependence of the dioptric power under non-lasing conditions, and a quantitative solution to the difference measured between the dioptric power under non-lasing and lasing conditions. The final section of this chapter provides an in-depth analysis of a self-Q-switched Alexandrite laser where the population lens is suggested as a possible loss-mechanism.

These results are of vital importance in further understanding the material properties of Alexandrite, in designing efficient power-scaled diode-pumped Alexandrite lasers (investigated later in Chapter 6) and in demonstrating a robust measurement technique and analytical model that can be used for other gain media. This work has been published in Optics Express [112] and presented at Photonics West 2020.

5.1 Thermal Lensing

Heat deposited in solid-state gain medium under optical pumping causes a temperature distribution that leads to temperature dependent refractive index changes, thermal expansion causing surface deformation and stress-induced photo-elastic refractive changes and birefringence [5, 106, 108]. The temperature distribution, $T(r, z)$, under continuous-wave (CW) pumping in end-pumped configuration is given by [108]

$$\frac{1}{r}\frac{\partial}{\partial r}\left(r\frac{\partial T}{\partial r}\right)+\frac{\partial^2 T}{\partial z^2}=-\frac{Q\left(r,z\right)}{K_c} \tag{5.1}$$

where K_c is the thermal conductivity of the gain medium, $Q\left(r,z\right)=\alpha_0\eta_h I\left(r,z\right)$ is the heat power per unit volume generated by absorption of pump intensity $I\left(r,z\right)$, α_0 is the pump absorption coefficient and η_h is the fraction of absorbed pump radiation converted to heat.

Assuming a non-diffracting, exponentially-absorbed pump intensity $I(r,z)=I(r,0)\exp(-\alpha_0 z)$ with purely radial heat flow (neglecting axial heat flow), Eq. (5.1) can be solved analytically. Two examples of pump distributions are the top-hat and Gaussian beam. The top-hat pump beam has an incident pump power P_0, radius w_p and a uniform intensity profile $I(r,0)=P_0/\pi w_p^2$ for $r\leq w_p$ and $I(r,0)=0$ for $r>w_p$. The dioptric lens power for a top-hat pump beam gives an aberration-free lens (within $r\leq w_p$)

$$D_T=\frac{P_{abs}\chi\eta_h}{2\pi w_p^2 K_c} \tag{5.2}$$

where $P_{abs}=P_0[1-\exp(-\alpha_0 l)]$ is the absorbed pump power over a crystal length l. For the Gaussian pump beam with equal power and radius, the intensity profile has a Gaussian profile of the form $I(r,0)=(2P_0/\pi w_p^2)\exp(-2r^2/w_p^2)$. The temperature distribution is not a simple quadratic function and so the on-axis dioptric power is twice as strong and the thermal lens has a dioptric power which varies radially where the radially-varying lensing introduces stronger aberrations as the transverse size of an interacting laser beam increases which can lead to spatial mode degradation in a laser system. The radial dioptric lens power is given by

$$D_T\left(r\right)=\frac{P_{abs}\chi\eta_h}{\pi w_p^2 K_c}\frac{\left[1-\exp\left(-2r^2/w_p^2\right)\right]}{2r^2/w_p^2}. \tag{5.3}$$

χ is the thermo-optic coefficient and is often given by $\chi=dn/dT$, however, in general it describes an effective thermo-optic coefficient that comprises three contributions $\chi=\chi_n+\chi_{SB}+\chi_{PE}$ [108]. The first term $\chi_n=dn/dT$ is the temperature-dependent refractive index and is often the dominant term. The second term χ_{SB} is the surface end bulging term. For an infinitesimally thin crystal it is given by $\chi_{SB}=(n-1)(1+\nu)$ where n is the unperturbed refractive index, ν is the Poisson's ratio, and α_T is the thermal expansion coefficient. The "thin-crystal" approximation should be treated as an upper limit and its contribution in a real crystal can

be much less. The final term $\chi_{PE} = 2n_0^3\alpha_T C'_{r,\theta}$ is a stress-induced refractive index contribution with cylindrical-symmetry induced birefringent principle axes [5, 108]. This birefringence can cause depolarisation losses especially in isotropic gain media such as Nd:YAG [113] but is less problematic in naturally birefringent gain media such as Alexandrite.

η_h is the fractional heating factor. In an ideal four-level optically pumped laser the fractional heating factor is equal to the quantum defect $\eta_h = 1 - \eta_s$ where $\eta_s = \lambda_o/\lambda_p$ is the Stokes efficiency - the ratio of the emitted optical to pump photon energies where each absorbed pump photon at wavelength λ_p results in an emitted optical photon with wavelength λ_o. Under strong lasing, stimulated emission dominates and $\lambda_o = \lambda_l$ is the lasing wavelength; under non-lasing conditions the spontaneous emission photon $\lambda_o = \lambda_f$ is the average fluorescence wavelength which can differ to that of the lasing wavelength as is the case for Alexandrite where $\lambda_f = 732\,\text{nm}$ [11].

In an ideal four-level laser therefore, the dioptric lens power of the thermal lens is directly proportional to the absorbed pump power. Plotting the lens dioptric power as a function of the absorbed pump power would give a linear relationship with an intercept at zero and a slope that depends on the material properties and the square of the pump radius. While there can be some complexity in regard to the exact values of these parameters their independence to the pump should not alter the linear relationship. One factor that could alter the linear dependence however is the fractional heating factor. When discussing the spectroscopic properties of Alexandrite in Chapter 3, it was shown that the excited state absorption at the pump and laser wavelength and ground state absorption at the laser wavelength are prevalent and are not negligible. It is therefore vital to include their contribution to the fractional heating factor to better model thermal lensing in Alexandrite.

5.2 Thermal Lensing with ESA Heating

Figure 5.1 shows the energy level diagram of Alexandrite including excited state absorption (ESA) and ground state absorption (GSA) at both the pump and laser wavelength using the same notation as that used in Chapter 3. The contribution of pump and laser ESA and laser GSA to the overall heating can be included to obtain a more general form for the heating factor via a modified pump quantum efficiency term η_p which is the probability that an absorbed pump photon generates

an upper-laser level population

$$\eta_h = 1 - \eta_s \eta_p. \tag{5.4}$$

It is important to lay the distinction between non-lasing and lasing conditions as there is a considerable difference in the effect of ESA and GSA. Analysing the effects under non-lasing offers two major advantages. Firstly the formalism is much simpler since the effects of ESA and GSA at the laser wavelength, which are quite complex, do not need to be included. Secondly, it also provides an additional means of comparing the theory to the experiment by looking at the difference between that under non-lasing and lasing conditions.

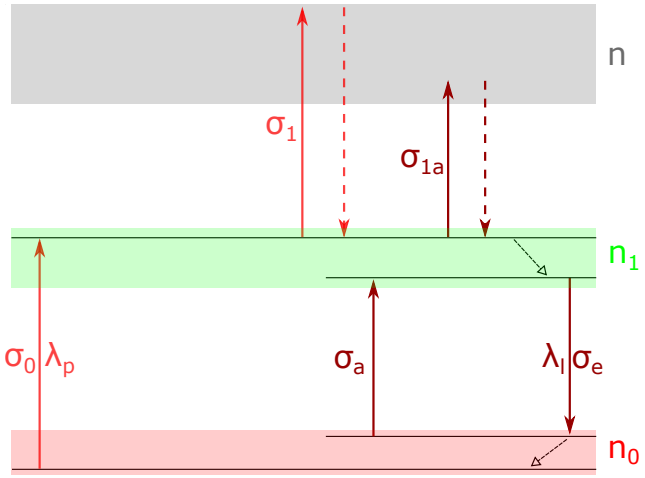

Figure 5.1: Schematic of the lasing energy levels of Cr^{3+} in Alexandrite with pump (λ_p) GSA and ESA, and laser (λ_l) stimulated emission, GSA and ESA. Grey region indicates higher energy levels and dashed lines indicate non-radiative decays. Ground, upper and excited-state populations are denoted n_0, n_1 and n_2, respectively.

5.2.1 Non-Lasing Conditions

Under non-lasing conditions the pump quantum efficiency $\eta_p = \eta_{p0}\eta_{p,esa}$ is a product of the intrinsic quantum efficiency η_{p0} and a pump efficiency $\eta_{p,esa}$ [99]. The intrinsic pump quantum efficiency is the branching probability of a pump-excited ion reaching the upper-state laser level leading to radiative spontaneous or stimulated emission compared to other non-radiative emissions, where in the latter all the energy is

dissipated in the gain medium as heat. In Alexandrite η_{p0} can be taken as unity since non-radiative emissions only occur at very high temperatures ($T > 670\,\mathrm{K}$). The pump ESA efficiency $\eta_{p,esa}$ is the ratio of the useful pump GSA that leads to inversion generation to the total pump GSA plus ESA. The pump ESA efficiency can therefore be defined as

$$\eta_{p,esa} = \frac{\sigma_0 n_0}{\sigma_0 n_0 + \sigma_1 n_1} = \frac{1-f}{1+(\gamma-1)\,f} \tag{5.5}$$

where n_0 is the ground state population and n_1 is the upper-state population as denoted in Fig. 5.1. $N = n_0 + n_1$, $f = n_1/N$ is the fractional inversion and $\gamma = \sigma_1/\sigma_0$ is the ratio of the pump ESA cross-section to the pump GSA cross-section. Since $\gamma \neq 0$, $\eta_{p,esa}$ will decrease from unity with increasing fractional inversion f. The pump power absorbed from pump ESA is directly transferred to heat. It is assumed that the pump ESA that takes the excited state ion to a higher-lying level (n_2) is rapidly returned back to the excited upper-laser level in a non-radiative transition. As such, pump ESA does not deplete the inversion but any pump ESA photons lost make no net contribution to increasing the population inversion.

The full mathematical derivation of $\eta_{p,esa}$ in terms of the absorbed pump power requires solving the coupled pump absorption and material rate equations. Under non-lasing conditions with pump ESA these expressions are given by [99]

$$\eta_{p,esa} = \frac{1 - Te^{\sigma_1 NF}}{1-T}\frac{\sigma_1 NF}{e^{\sigma_1 NF}-1} \tag{5.6}$$

$$\frac{I}{I_s} = \frac{1}{1 - Te^{\sigma_1 NF}}\frac{e^{\sigma_1 NF}-1}{\gamma} \tag{5.7}$$

where T is the pump transmission through the laser crystal, $I_s = h\nu_p/\sigma_0\tau_f$ is the pump saturation intensity and $F = \int_0^l f(z)\,dz$ is the integrated inversion factor. Determining $\eta_{p,esa}$ in terms of the absorbed pump power P_{abs} (from the intensity I) can only be solved numerically using Eqs. (5.6) and (5.7), however under the approximation that the the pump is strongly absorbed ($T << 1$) and it is not excessive ($T\exp(\sigma_1 NF) << 1$), then $\eta_{p,esa}$ and F can be approximated to

$$\eta_{p,esa} \approx 1 - \frac{1}{2}\sigma_1 NF, \tag{5.8}$$

$$F \approx \frac{1}{\sigma_0 N}\left[\frac{I}{I_s} - \frac{\gamma}{2}\left(\frac{I}{I_s}\right)^2\right]. \tag{5.9}$$

The heating factor can be written in terms of the incident intensity by substituting Eqs. (5.9) and (5.8) into Eq. (5.4)

$$\eta_h = 1 - \eta_s\left(1 - \frac{\gamma}{2}\left[\frac{I}{I_s} - \frac{\gamma}{2}\left(\frac{I}{I_s}\right)^2\right]\right). \tag{5.10}$$

It is more convenient to write the fractional heating factor in terms of the pump power so that it can be compared to the experimental results. This can be done by setting $P_0 = I(\pi w_p^2/2)$ as the absorbed pump power and $P_s = I_s(\pi w_p^2/2)$ as the pump saturation power. This gives

$$\eta_h = 1 - \eta_s\left(1 - \frac{\gamma}{2}\left[\frac{P_0}{P_s} - \frac{\gamma}{2}\left(\frac{P_0}{P_s}\right)^2\right]\right). \tag{5.11}$$

An analytical expression for the thermal lens dioptric power on axis ($r = 0$) with pump ESA included can therefore be determined by substituting Eq. (5.11) into Eq. (5.3)

$$D_T(0) = \frac{\chi}{\pi w_p^2 K_c}\left[\eta_{h0} P_{abs} + \eta_s \frac{\gamma}{2}\frac{P_{abs}^2}{P_s}\right] \tag{5.12}$$

where terms proportional to P_0^3 have been neglected (as they are negligible), and under the assumption that $T << 1$ the absorbed pump power is equal to the incident pump power $P_{abs} = P_0$ and $\eta_{h0} = 1 - \eta_s = 1 - \lambda_p/\lambda_f$. Equation (5.12) shows that under non-lasing conditions, pump ESA provides a quadratic power term and leads to a non-linear relationship between the thermal lens dioptric power and the absorbed pump power.

5.2.2 Lasing Conditions

Under lasing conditions the inversion is clamped at threshold and so pump ESA is fixed at its threshold value, however above threshold the effects of laser GSA and laser ESA have to be included. It can be included through the term $\gamma_l = \sigma_{1a}/(\sigma_e + \sigma_a)$ where σ_{1a}, σ_e and σ_a are the laser ESA, emission and GSA cross sections, respectively. The transition from non-lasing to strong lasing is included by

using a lasing efficiency factor η_l that is equal to the ratio of stimulated emission to the total radiative emission (sum of spontaneous and stimulated emission). The thermal lens under lasing conditions is given by

$$D_T(0) = \frac{P_{abs}\chi}{\pi w_p^2 K_c}\left[\eta_{h0} + \eta_s'\frac{\gamma}{2}\frac{P_{th}}{P_s}\right]\left(1-\gamma_l'\right) \tag{5.13}$$

where $\eta_s' = (1-\eta_l)\lambda_p/\lambda_f + \eta_l\lambda_p/\lambda_l$ and $\gamma_l' = \eta_l\gamma_l$. Hence under lasing conditions the thermal lens is also non-linearly proportional to the absorbed pump power due to the power dependence of η_l.

5.3 Population Lensing

An additional form of pump-induced lensing that needs consideration is the electronic or population lens. The difference in polarizability between the ground and excited state $\Delta\alpha_p = \alpha_e - \alpha_g$ leads to a refractive index change Δn_e. Population lensing has been observed in a number of Chromium-doped media [114, 115] as well as in Yb and Nd-doped media where it can be comparable or even stronger than the thermally-induced lens [77, 116]. When pumping with a spatially varying intensity profile such as a Gaussian beam the spatial variation of the refractive index change is given by [114]

$$\Delta n_e(r,z) = \frac{2\pi}{n} f_L^2 N \Delta\alpha_p \frac{n_1(r,z)}{N} = C\frac{n_1(r,z)}{N} \tag{5.14}$$

where n is the unperturbed refractive index, $f_L = \left(n^2+2\right)/3$ is the Lorentz factor, N is the total active population density and $n_1(r,z)$ is the spatial profile of the excited state population density. The optical path wavefront due to Δn_e is given by

$$W(r) = \int_0^l \Delta n_e(r,z)\,dz = C\int_0^l \frac{n_1(r,z)}{N}dz = CF(r) \tag{5.15}$$

where $F(r)$ is the integrated inversion factor over the gain medium of length l. The dioptric power of the population lens due to this change in wavefront is given by

$$D_P = \frac{2}{r^2}\Delta W = \frac{2}{r^2}\left(W(0) - W(r)\right) = \frac{2}{r^2}C\left(F(0) - F(r)\right). \tag{5.16}$$

By taking the radial form of the integrated inversion factor (Eq. (5.9)) the dioptric power of the population lens in terms of the absorbed pump power (derivation shown in Appendix B) to second order is given by

$$D_P = \frac{4C}{\alpha_0 w_p^2}\left[\frac{P_{abs}}{P_s} - \gamma\left(\frac{P_{abs}^2}{P_s}\right)^2\right]. \tag{5.17}$$

The population lens is non-linearly proportional to the absorbed pump power but with a negative quadratic term P_{abs}^2. Under lasing conditions the inversion and therefore the lens dioptric power is clamped at $P_{abs} = P_{th}$.

5.4 Experimental System and Wavefront Measurement

Figure 5.2 shows the experimental setup used to measure the pump-induced lensing effects of an Alexandrite laser rod using the wavefront measuring approach with a Shack-Hartmann wavefront sensor (SH-WFS). The SH-WFS (Thorlabs, WFS20-7AR/M) measures the wavefront curvature enabling both the lens dioptric power and aberrations to be determined. These were measured using a continuous-wave (CW) green probe beam ($\lambda_{pr} = 532\,\text{nm}$) that was transmitted through the crystal and imaged onto the SH-WFS using an afocal magnifying telescope.

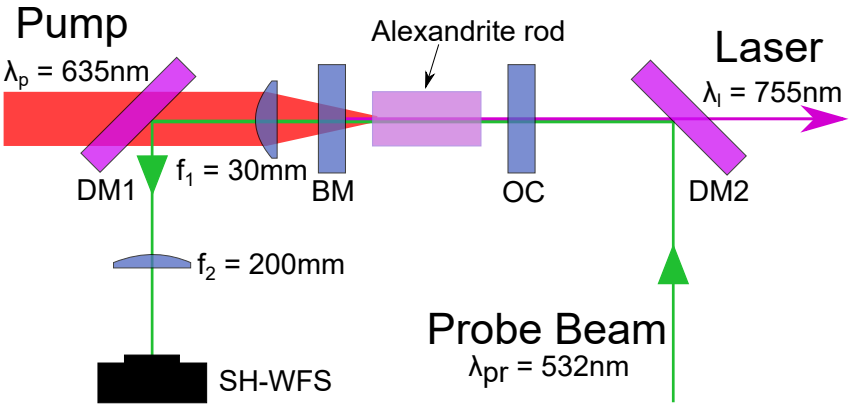

Figure 5.2: Schematic of the experimental pump-induced lensing measurement system of the end-pumped Alexandrite rod in a laser cavity (formed by mirrors BM and OC). f_1 and f_2 form an afocal magnifying telescope to relay-image a probe beam wavefront at the Alexandrite crystal onto a Shack-Hartmann wavefront sensor (SH-WFS). DM1 and DM2 are dichroic mirrors to separate pump, probe and laser wavelengths.

The laser cavity was formed of a dichroic back mirror (BM) that was highly reflective (HR) at the laser wavelength ($\lambda_l \sim 755\,\text{nm}$) and highly transmissive (HT) at the pump wavelength ($\lambda_p = 635\,\text{nm}$), and a plane mirror output coupler (OC) with a reflectivity $R_{\text{OC}} = 98.5\,\%$ at the laser wavelength. The Alexandrite crystal was 10 mm long, 4 mm diameter rod with a Chromium-doping of 0.2 at.%. The crystal was held in a water-cooled copper heat sink at 16 °C. The physical cavity length was 20 mm. This setup allowed the measurement of the pump-induced dioptric lens power under both lasing and non-lasing conditions (by misaligning the OC).

The laser was pumped by a CW fibre-delivered red diode laser ($M^2 = 100$) operating at 635 nm - full characterisation will be provided in Chapter 6. The output of the fibre was collimated and polarised using a polarising beam splitter such that the output was linearly polarised. A half-waveplate was used to rotate the polarisation to the crystal b-axis. The absorption coefficient at the pump wavelength was measured to be $\alpha_0 = 480\,\text{m}^{-1}$. The pump beam was focused near the input face of the laser rod with a 30 mm aspheric lens (f_1) to give a waist radius of $w_p = 200\,\mu\text{m}$ ($z_R = 2\,\text{mm}$). The intensity profile of the pump beam at focus was also measured and a best fit was performed with different Super-Gaussian functions $\exp(-2r^n/w_p^n)$ with the $n = 2$ order found to describe the intensity profile most accurately.

The probe beam was linearly polarised to the crystal b-axis and collimated to a beam radius of 500 µm so that the beam overfilled the pump region. It was imaged at the pump face of the crystal using the combination of the 30 mm aspheric pump lens (f_1) and a 200 mm lens (f_2) onto the SH-WFS. A dichroic mirror (DM1) that was HR at the probe wavelength and HT at the pump wavelength was placed between the two lenses to separate the probe beam from the pump. An additional 532 nm bandpass filter (FWHM=10 nm) was placed on the SH-WFS to further eliminate back scattered pump light and laser fluorescence/laser leakage.

The two lens arrangement enabled the relay image of the wavefront aberration caused at the vicinity of the pump focal region onto the SH-WFS sensor plane. Furthermore, by using lenses of different focal length it provided a magnification factor $m = f_2/f_1$ of the lateral size of the pump beam region (diameter = 400 µm), to fill a suitable aperture size of the SH-WFS CMOS array. The $f_2 = 200\,\text{mm}$ lens in combination with the $f_1 = 30\,\text{mm}$ lens provided a magnification of $m = 200/30 = 6.67$, therefore producing a magnified pump region of $0.40\,\text{mm} \times 6.67 \approx 2.7\,\text{mm}$. This fitted comfortably inside the SH-WFS aperture ($7.2 \times 5.4\,\text{mm}$) and provided good lateral resolution across the discrete microlens array (SH-WFS pixel pitch

150 µm). The pupil size in the SH-WFS measurement software was fixed at 2.5 mm, corresponding to just within the magnified pump region (~ 2.7 mm).

In measuring the wavefront curvature, the relay image system with a magnification of m, produces an increase in the radius of curvature measured at the conjugate sensor plane of m^2. The measured wavefront was therefore rescaled by dividing with a scaling factor $m^2 = 44.5$ to obtain the focal length of the pump induced lens. The SH-WFS was initially calibrated by removing the laser rod and measuring the probe wavefront curvature after passing through five lenses of known focal lengths placed at the focal point of the pump lens coincident with the Alexandrite thermal lens region. The measured dioptric power was in excellent agreement with the actual lens dioptric power with the measurement coming to within 5 % of the actual value across the range of $D_{lens} = 0.5 - 20\,\mathrm{m}^{-1}$ ($f_{lens} = 2000 - 50$ mm).

5.5 Experimental Results

Figure 5.3 shows the dioptric power as a function of the absorbed pump power as well as the laser output power. It is clear that there is a very pronounced difference between the dioptric power under non-lasing and lasing conditions.

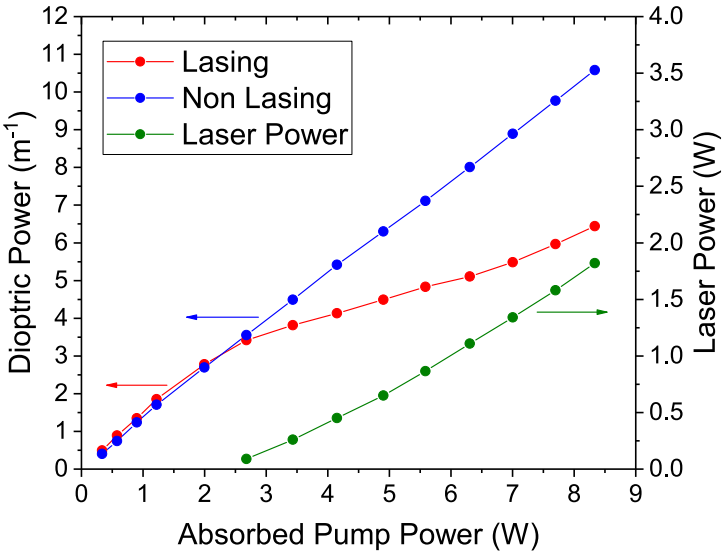

Figure 5.3: Measured lens dioptric power under non-lasing conditions (blue), lasing conditions (red) and laser power (green) as a function of the absorbed pump power.

The non-lasing lens dioptric power increases nearly linearly with absorbed pump power. This pump dependence of the lens dioptric power is contrary to that expected from the nonlinear pump ESA contribution as shown by Eq. (5.12). Under lasing conditions, the lens dioptric power is noticeably different, diverging away from that under non-lasing conditions above laser threshold. At a maximum absorbed pump power of 8.3 W the dioptric power was 10.5 m^{-1} and 6.5 m^{-1} under non-lasing and lasing conditions, respectively, and hence the lasing dioptric power was $\sim 60\,\%$ of the non-lasing lens dioptric power.

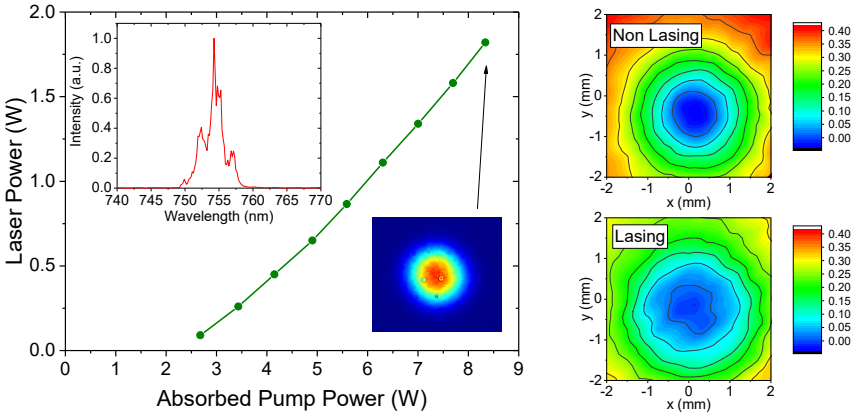

Figure 5.4: (a) Laser power as a function of the absorbed pump power. Inset shows laser wavelength spectrum and beam profile at maximum power. (b) 2D wavefront at maximum pump power under non-lasing and lasing conditions.

A plot of the laser power as a function of the absorbed pump power alone is shown in Fig. 5.4(a). Laser threshold was at an absorbed pump power of $P_{th} = 2.24\,\mathrm{W}$, this corresponds to the point where the lens dioptric power under lasing conditions deviates from that under non-lasing conditions as shown in Fig. 5.3. At a maximum pump power of 8.3 W the laser power was 1.82 W and an overall slope efficiency of $\eta_s = 30.8\,\%$ was determined from a linear fit. The beam quality was measured to be $M^2 = 1.1$ near threshold and at full pump power $M^2 = 1.5$. The laser spectrum (shown in inset of Fig. 5.4(a)) was centred at $\lambda_l = 755\,\mathrm{nm}$ with a linewidth of FWHM $\approx 3\,\mathrm{nm}$. Figure 5.4(b) shows the 2D wavefront acquired by the SH-WFS under non-lasing and lasing conditions at maximum pump power. This demonstrates the noticeably stronger curvature measured under non-lasing conditions compared to that under lasing conditions.

5.6 Analytical Model Fitting

The measured lens dioptric power under non-lasing and lasing conditions can be compared to the analytical expressions covered in Sections 5.2 and 5.3 to characterise the impact of pump ESA and the population lens. It also serves as a means of verifying a theoretical model that could be used to predict the pump-induced lens in other work which has so far yet to be demonstrated for diode-end-pumped Alexandrite lasers.

5.6.1 Non-Lasing Conditions

The simplest initial approach is to consider the results under non-lasing conditions. If initially it is assumed that the measured lens dioptric power is due to a thermal lens with pump ESA then the measured data can be fitted with an equation of the form

$$D_{NL} = a_1 P_{abs} + a_2 P_{abs}^2 \tag{5.18}$$

where a_1 and a_2 are the coefficients calculated from the fitting (note that the intercept of the fitting is set to zero since the dioptric power can only tend to zero when the absorbed pump power is zero). The fitting performed using Eq. (5.18) gives $a_1 = 1.34\,\mathrm{m^{-1}\,W^{-1}}$ and $a_2 = -0.01\,\mathrm{m^{-1}\,W^{-2}}$. To compare these values to the theoretical thermal lens with pump ESA it's worth considering the material and pump parameters in Eq. (5.20). Table 5.1 shows the known parameters. Though most are well known there is some ambiguity in the value of the thermo-optic coefficient χ. Although the value of dn/dT is well known, the contribution of the surface bulge and stress-induced birefringence is less clear. Another ambiguity is the pump waist w_p which due to the divergence of the pump is not necessarily the value of the waist at focus. Here an effective waist size w_p' will be taken instead, which is given by [111, 117]

$$w_p'^2 = \frac{\int_0^l \alpha_0 e^{-\alpha_0 z} w^2(z)\, dz}{\int_0^l \alpha_0 e^{-\alpha_0 z} dz} \tag{5.19}$$

which when solved gives $w_p' = 265\,\mu\mathrm{m}$. Using the values in Table 5.1 and Eq. (5.12) the fitted a_1 coefficient gives a thermo-optic coefficient of $\chi = a_1 \pi w_p'^2 Kc/\eta_{h0} = 5.2 \times 10^{-5}\,\mathrm{K^{-1}}$ which at around 5 times greater than dn/dT (which is the greatest

contributor to χ) suggests the thermal lens model is not accurate. Furthermore, and perhaps more significantly is that the a_2 coefficient is negative and not positive as expected from Eq. (5.12).

Table 5.1: Alexandrite and pump parameters used in model fitting. Temperature dependent parameters have been evaluated at $T = 16\,^{\circ}\mathrm{C}$.

Parameter	Value	Source
K_c	$23\,\mathrm{W\,m^{-1}\,K^{-1}}$	[11]
dn/dT	$9.1 \times 10^{-6}\,\mathrm{K^{-1}}$	[82]
n	1.7518	[84]
w_p (w_p')	200 µm (265 µm)	measured
α_0	$480\,\mathrm{m^{-1}}$	measured
λ_p	635 nm	measured
λ_f	732 nm	[11]
λ_l	755 nm	measured
σ_0	$70 \times 10^{-25}\,\mathrm{m^2}$	[11]
σ_e	$5.0 \times 10^{-25}\,\mathrm{m^2}$	[100]
σ_1	$55 \times 10^{-25}\,\mathrm{m^2}$	[90]
σ_{1a}	$0.6 \times 10^{-25}\,\mathrm{m^2}$	[100]
γ (γ_l)	0.78 (0.12)	calculated
τ_f	290 µs	[11]
I_s	$154\,\mathrm{MW\,m^{-2}}$	calculated
P_s	17.0 W	calculated

It is therefore clear that the contribution from the population lens must be included. Here it is assumed that the measured dioptric lens power corresponds to the sum of the thermal and population lens given by Eqs. (5.12) and (5.16), respectively, which gives

$$D_{NL} = \left[\frac{\chi\eta_{h_0}}{\pi {w_p'}^2 K_c} + \frac{4C}{\alpha_0 {w_p'}^2 P_s}\right] P_0 + \left[\frac{\chi}{\pi {w_p'}^2 K_c}\frac{\gamma}{2}\frac{\eta_s}{P_s} - \gamma\frac{4C}{\alpha_0 {w_p'}^2 P_s^2}\right] P_0^2. \tag{5.20}$$

Fitting Eq. (5.20) to the measured data is shown in Fig. 5.5 as well as the contribution of the thermal lens (shown in orange) and population lens (shown in green). Using the fitted values of a_1 and a_2 gives $\chi = 1.1 \times 10^{-5}\,\mathrm{K^{-1}}$ and a polarizability difference (through $C = 2\pi f_L^2 N \Delta\alpha_p/N$) of $\Delta\alpha_p = 2.3 \times 10^{-31}\,\mathrm{m^3}$. This thermo-optic coefficient corresponds to an 80 % contribution from the temperature dependent refractive (dn/dT) and the remaining 20 % contribution from surface bulging and

the stress-induced birefringence. An FEA model (using LASCAD software) of the experiment (which includes surface bulging but not stress-induced birefringence) found that surface bulging contributed to 10 % of the total thermo-optic coefficient. This suggests another 10 % contribution from the stress-induced biregfringence. Further confirmation of the combined thermal and population lens is shown with the value of the polarizability difference which is relatively consistent to a previously measured value of $2.7 \times 10^{-31}\,\mathrm{m}^3$ [86] and the range of values measured for other Chromium-doped media at around 1-5 $\times\, 10^{-31}\,\mathrm{m}^3$ [87, 114].

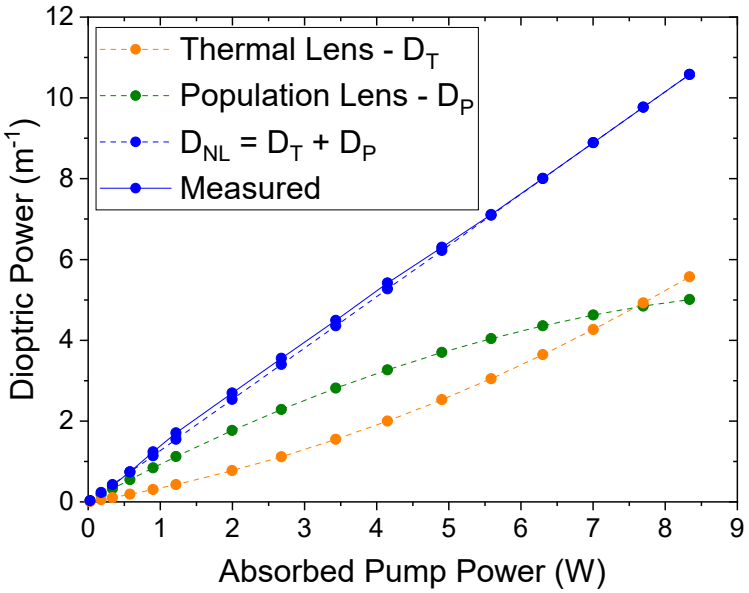

Figure 5.5: Measured (blue-solid) and fitted (blue-dashed) lens dioptric power as function of the absorbed pump power under non-lasing conditions. Thermal (orange-dashed) and population (green-dashed) lens components of the total lens are also shown.

5.6.2 Lasing Conditions

Under lasing conditions the combined pump-induced lens is described by Eq. (5.20) up to threshold and by the sum of Eq (5.13) and Eq. (5.17) with $P_{abs} = P_{th}$ above threshold which gives

$$D_L = \frac{P_{abs}\chi}{\pi w_p^2 K_c}\left[\eta_{h0} + \eta_s'\frac{\gamma}{2}\frac{P_{th}}{P_s}\right](1-\gamma_l') + \frac{4C}{\alpha_0 w_p^2}\left[\frac{P_{th}}{P_s} - \gamma\left(\frac{P_{th}^2}{P_s}\right)^2\right]. \qquad (5.21)$$

This describes a pump-induced lens varying near linearly with absorbed pump power (with slight non-linearity due to η_s' and γ_l' terms) with a fixed offset term. Using $\chi = 1.1 \times 10^{-5}\,\mathrm{K}^{-1}$, $\Delta\alpha_p = 2.3 \times 10^{-31}\,\mathrm{m}^3$, the parameters in Table 5.1 and varying η_l linearly from $\eta_l = 0$ at $P_{abs} = P_{th} = 2.2\,\mathrm{W}$ to $\eta_l = 1$ at $P_{abs} = 8.3\,\mathrm{W}$, Eq. (5.21) is plotted as a function of the absorbed pump power and compared to the measured dioptric power under lasing conditions as shown in Fig. 5.6.

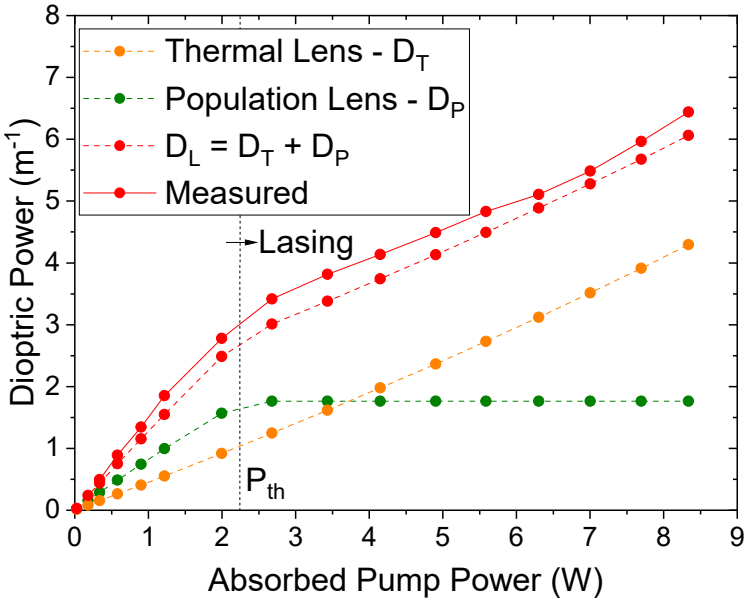

Figure 5.6: Measured (red-solid) and theoretical (red-dashed) lens dioptric power as function of the absorbed pump power under lasing conditions. Thermal (orange-dashed) and population (green-dashed) lens components of the total lens are also shown.

The results under lasing conditions with the thermal lens under lasing conditions and the population lens clamped at threshold are in very good agreement with the measured result. In this case there was no re-adjustment of the fitting parameters, so it provides further independent support of the underlying hypothesis of a combined thermal and population lens.

The population lens has been identified as a mechanism to provide explanation of the experimental non-lasing and lasing lensing results. A population lens is not unexpected for Chromium-doped materials [87, 114] and has been postulated as the mechanism of self-Q-switching in Cr:LiCAF [115] and in Alexandrite [65]. In Chapter 4 self-Q-switching was also observed in Alexandrite.

5.7 Self-Q-Switched Alexandrite Laser

Figure 5.7 shows the diode-pumped Alexandrite laser as demonstrated in Chapter 4. A fibre-coupled diode module collimated with a $f_C = 35\,\text{mm}$ lens was used as the pump source. The module had a maximum output power of 5.5 W with $\sim 70\,\%$ of the power in its major polarisation axis. The major polarisation axis was rotated to the high absorbing crystal b-axis using a half-wave plate. The pump was focused by an aspheric lens with focal length $f = 50\,\text{mm}$ to a waist radius of $w_p = 75\,\mu\text{m}$. The Rayleigh range was $z_R = 1.0\,\text{mm}$, and the beam quality was measured to be $M^2 = 50$.

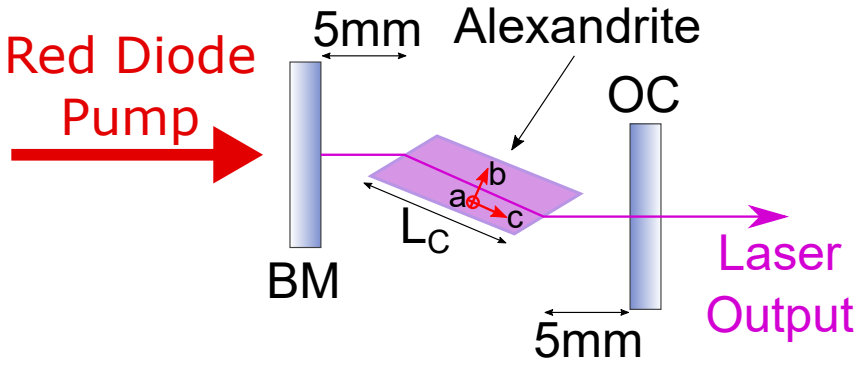

Figure 5.7: Ultra-compact Alexandrite laser cavity.

The Alexandrite resonator was a simple and compact (cavity length $\sim 20\,\text{mm}$) plane-plane resonator with a back mirror (BM) as one end mirror with dichroic coating that was HT at the pump wavelength and HR at the laser wavelength. The output coupler had reflectivity $R_{\text{OC}} = 99.5\,\%$ at the laser wavelength. The Brewster-cut crystal was an 8 mm long and $4 \times 4\,\text{mm}$ cross section slab with ~ 0.24 at.% Chromium-doping. It was mounted on a copper heat sink with water cooling over a 10-60 °C temperature range.

Stable and reproducible self-Q-switching (SQS) was obtained by optimising the cavity for output power by adjusting the angle of incidence of the Brewster-cut crystal and cooling the temperature of the crystal to below 20 °C. Further details of the SQS stability will be discussed later.

The maximum power was obtained at a water temperature of 10 °C. Figure 5.8 shows the laser power as a function of the absorbed pump power. The maximum laser power was 1.46 W with a slope efficiency of 49 %. The beam quality was $M^2 \leq 1.2$ in both directions. Figures 5.9(a) and 5.9(b) show the output pulse and

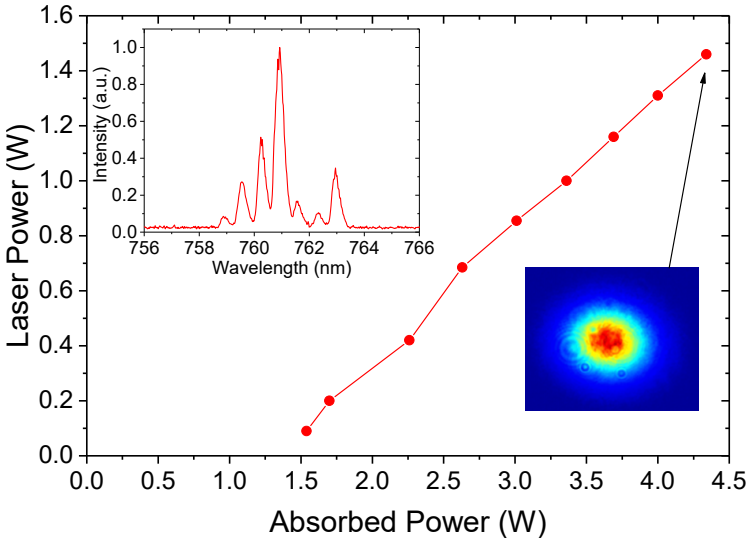

Figure 5.8: Laser power as a function of absorbed pump power at 10 °C. Inset shows beam profile and spectrum at maximum power.

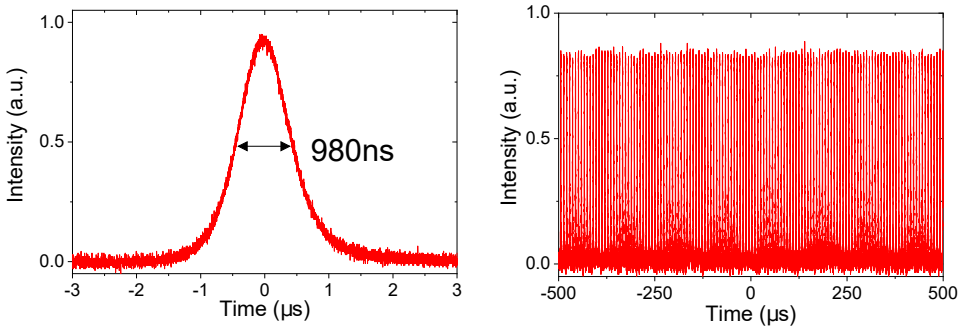

Figure 5.9: Temporal output of laser at maximum power with: (a) 980 ns Q-switched pulse; (b) 1 ms capture of stable Q-switched pulse train.

pulse train, respectively, at maximum power. The pulse duration was 980 ns at 135 kHz. SQS operation was highly stable as can be seen in the pulse train in Fig. 5.9(b). At maximum pump power, the pulse energy and peak power were 10.8 µJ and 11.0 W, respectively.

To ensure that the results were reproducible, the laser cavity was realigned and optimised with the pump focused at a different region of the crystal. Stable SQS was obtained with the average power, pulse duration and repetition rate measured

as a function of the absorbed pump power at a temperature of 16 °C. However, as was observed previously, stable SQS only occurred at 10-20 °C, as indicated in Fig. 5.10(b). Stable SQS was qualitatively assessed on the variations in the pulse height over a long time period as illustrated in Fig. 5.10(a). It shows the laser power as a function of the absorbed pump power with the long pulse train shown at the onset of Q-switching and at higher pump power where it was stable. Quantitatively, stable SQS was defined as that where the standard deviation of the repetition rate was <1 % and of the pulse energy was <4 %.

Similar observations were made when varying the crystal temperature. At 10-20 °C the pulse train was stable, similar to that shown in the inset in Fig. 5.10(a) for stable SQS. Above 20 °C SQS persisted but with large variations in pulse height and repetition rate. It was also found that the laser power decreased with increasing temperature, contrary to that typically observed in Alexandrite, though the actual temperature of the crystal and the temperature of the water may be quite different, especially with only a single side of the crystal attached to the copper mount.

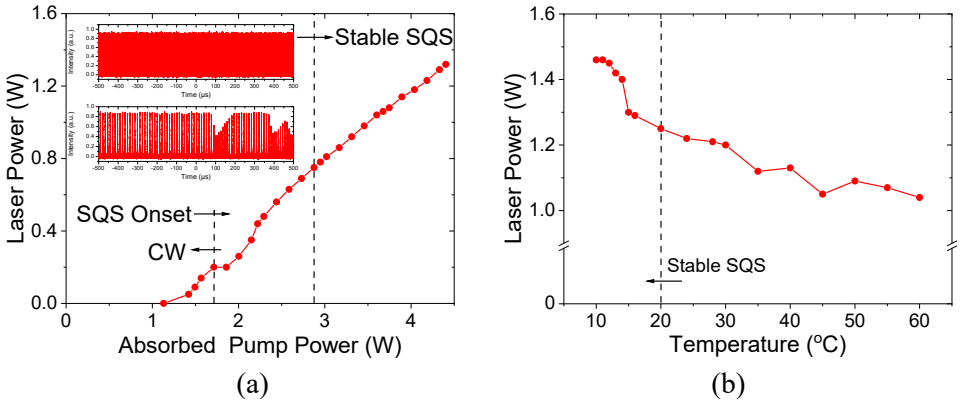

Figure 5.10: (a) Laser power as a function of absorbed pump power at 16 °C. Three regions are shown: CW operation, SQS onset and stable SQS. Stable SQS occurred above around 3 W of absorbed pump power. (b) Laser power as a function of crystal temperature at maximum pump power. Stable SQS occurred at 10-20 °C.

For the new setup, at maximum pump power the laser power was 1.32 W with a slope efficiency of 43 %. The pulse duration increased linearly with absorbed pump power from 643 ns at 3 W to 657 ns at maximum pump power. The repetition rate increased from 121 kHz at 3 W to 138 kHz at maximum pump power. At lower pump powers the repetition rate was lower and the standard deviation higher at > 10 %

compared to $< 1\,\%$ above 3 W. The sudden change in the standard deviation at 3 W of absorbed pump power matches well to the stable SQS region shown in Fig. 5.10(a). At maximum pump power the pulse energy and peak power were 9.6 µJ and 14.6 W, respectively. Compared to previous work on passively Q-switched (SESAM) Alexandrite, the pulse energy is higher by a factor of 1.4 with over a tenfold increase in the repetition rate [68].

Since Q-switching of any form in a solid-state laser requires the modulation of cavity losses, it is not immediately clear as to the origin of the time-dependent loss mechanism here. SQS in Chromium-doped gain media such as Alexandrite, Cr:LiCAF, Cr:LiSAF and Ruby have been previously reported in literature [65, 87, 96]. While several mechanisms for the time-dependent loss have been reported, recently the time-dependent lens has been seen as the most probable cause. A time-dependent variation in the refractive index to cause a time-dependent lens in combination with a soft or hard aperture would result in an intensity dependent loss. The manifestation of this effect is as of yet unclear and no systematic study has been carried out. Of note here however is the high repetition rate of >100 kHz. The time constant for thermal gradients to appear is around [37]

$$\tau = \frac{w_p^2 \rho C_p}{K_c} \tag{5.22}$$

where $C_p = 1.05\,\mathrm{J\,g^{-1}\,K^{-1}}$ [76] is the specific heat capacity and $\rho = 3.69\,\mathrm{g\,cm^{-3}}$ [11] is the density of Alexandrite. For a pump size of $w_p = 75\,\mu\mathrm{m}$ the time constant is $\tau \approx 1\,\mathrm{ms}$. This rate is substantially slower than the oscillation period of around 10 µs and so a time-dependent thermal lens is unlikely to be the cause. However, a time-dependent lens based on an electronic time constant is far more agreeable with the measured oscillation period. The population lens therefore provides a possible "fast" modulation mechanism for the SQS effect observed here and in other Chromium-doped materials.

5.8 Summary

This chapter provides an in-depth investigation of pump-induced lensing effects in diode-end-pumped Alexandrite using a direct experimental measurement approach together with an analytical model. This is the first direct wavefront measurement of pump-induced lensing in Alexandrite using a Shack-Hartmann wavefront sensor

(SH-WFS) performed as a function of absorbed pump power under both lasing and non-lasing conditions.

Under non-lasing conditions the lens dioptric power was found to grow almost linearly with absorbed pump power, a surprising result when assuming thermal lensing which due to excited state absorption (ESA) should give rise to a dioptric power that is non-linearly proportional to the absorbed pump power. Another surprising result was that the lens dioptric power under lasing conditions was significantly different and reduced to 60 % of the value of the lens dioptric power under non-lasing conditions. These results together are hard to reconcile by a simple thermally-induced lens model, even if account is taken for some uncertainties in material values and experimental errors. However, it has been previously shown that Chromium-doped laser materials have an electronic component to their refractive index due to a difference in the polarizability of ions in the excited state to ions in the ground state. A refractive index distribution produced by a Gaussian pump beam leads to a positive population lens. An analytical model based on a combined thermal and population lens is able to qualitatively describe the measured lens dioptric power and quantitatively provide a polarizability difference of $\Delta\alpha_p = 2.3 \times 10^{-31}\,\mathrm{m}^3$ which matched well to other Chromium-doped laser materials. With the population lens clamped at threshold the reduced lens dioptric power measured under lasing conditions also matches well to the combined thermal and population lens theory, providing further independent support for the hypothesis of the population lens.

The results of this chapter provide new insight into the pump-induced lensing in Alexandrite that help to support future laser design for power scaling with high beam quality - the content for the next chapter. Population lensing is as a possible mechanism to provide explanation of the experimental lensing results. This is not unexpected for Chromium-doped materials and also provides a “fast” electronic modulation mechanism for self-Q-switching that was shown in Section 5.7. Further corroborating experiment(s) is required to directly observe the population lens, such as its temporal response compared to the build-up or decay of the thermal lens. The SH-WFS slow response time is not very suitable but with pulsed probe and/or pump or other experiments might be devised to make this temporal response measurement. Population dynamics is another possible mechanism where a time-dependent rate equation model could indicate the switching times. The methodologies applied in this chapter such as the measurement technique, model of thermal lens (with ESA heating) and population lens can also be extended to other laser materials.

Chapter 6

Power Scaled TEM_{00} Alexandrite Lasers

The availability of commercial high power red laser diodes has enabled diode-pumped Alexandrite lasers to reach continuous-wave powers of >10 W. The current world-records for highest power are 26.2 W demonstrated by Teppitaksak et al. [66] in end-pumped configuration and 12.6 W demonstrated by Damzen et al. [118] in side-pumped configuration. In both cases diffraction limited beam quality was sacrificed for high output power and efficiency. High spatial quality (TEM_{00}) and high efficiency has typically been limited to the 1 W level using lower powered fibre-coupled pump units (see for example [90]) where weaker pump-induced lensing does not hinder the mode quality. These fibre-coupled units at the 5 W-level have enabled up to 2.1 W of output laser power in TEM_{00} operation [119].

Pumping with free space diode bars and stacks typically requires reshaping techniques to overcome the pump beam asymmetry adding further complexity and overall size to the pump delivery system. TEM_{00} operation can be achieved from such systems as demonstrated by Damzen et al. where 4 W was achieved with a Gaussian output mode profile but with a severe reduction in optical efficiency ($\sim 10\,\%$) [118]. Pumping with multimode free-space diodes in Q-switched operation as shown by Munk et al. and Coney et al. have also required pump reshaping optics and often complex cavity design for TEM_{00} operation [69, 120].

High power multi-mode fibre-coupled diodes offer an attractive alternative to free space diode systems. Fibre-coupling provides a more robust and adaptable pump delivery - pump modules can be easily replaced with little to no realignment

required. Direct imaging of the fibre output provides symmetrical circular output beams which allows more uniform heating and therefore a less aberrated lens [106]. Better modelling of the lens dioptric power and its effect on the laser mode size can then be made.

In this chapter the world-record highest power diode-pumped TEM_{00} Alexandrite laser is presented as well as the first demonstration of a TEM_{00} multi-watt tunable diode-pumped vibronic laser in the near-infrared. This is achieved using fibre-coupled pumping and a novel compact cavity design incorporating a convex mirror for laser mode size control and with accurate understanding of the pump induced lens strength using a Shack-Hartmann wavefront sensor as discussed in Chapter 5. The results from this work have been published in OSA Continuum [121] and presented at two international conferences.

6.1 High Power Fibre-Coupled Diode Module

For higher power pumping a 200 µm diameter fibre-coupled diode module was used. The diode is a commercially available module with internal water-cooling for temperature control - the temperature was fixed at 16 °C. The fibre output was collimated with a $f_c = 35$ mm focal length collimator. Figure 6.1(a) shows the total unpolarised pump power measured at the fibre output with the collimator. At a maximum drive current of 14 A the total output power was 35.7 W. Figure 6.1(b) shows the laser wavelength as a function of the drive current demonstrating the typical red-shift in wavelength at higher drive current due to the increased diode temperature. At 14 A the laser wavelength and linewidth were 638.0 nm and 1.2 nm, respectively.

Figure 6.3 shows a schematic of the pump delivery setup. Using a plate polariser (PP), the pump beam was transmitted and reflected into horizontal and vertical polarised components. The transmitted horizontal component was focused with an aspheric lens of focal length f_p. A half-wave plate ($\lambda/2$) was used to rotate the horizontal component to the b-axis of the Alexandrite crystal (which was mounted in the vertical direction). The reflected vertical component of the pump was steered to the opposite end of the laser cavity for dual-end-pumping using three highly reflective (HR) mirrors at the pump wavelength (~ 640 nm).

The pump delivery was arranged in two ways. Firstly the collimator-lens distance, d, was set such that $d >> f_c + f_p$ and no lenses were used in the second pump arm. This setup provided a Gaussian pump profile as shown in Fig. 6.2(a). In the

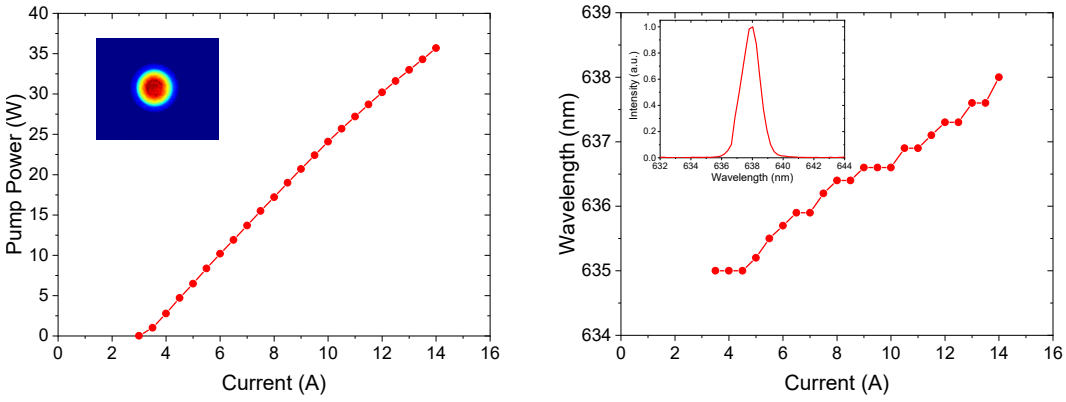

(a) (b)

Figure 6.1: (a) Pump power as a function of drive current. (b) Pump wavelength as a function of drive current.

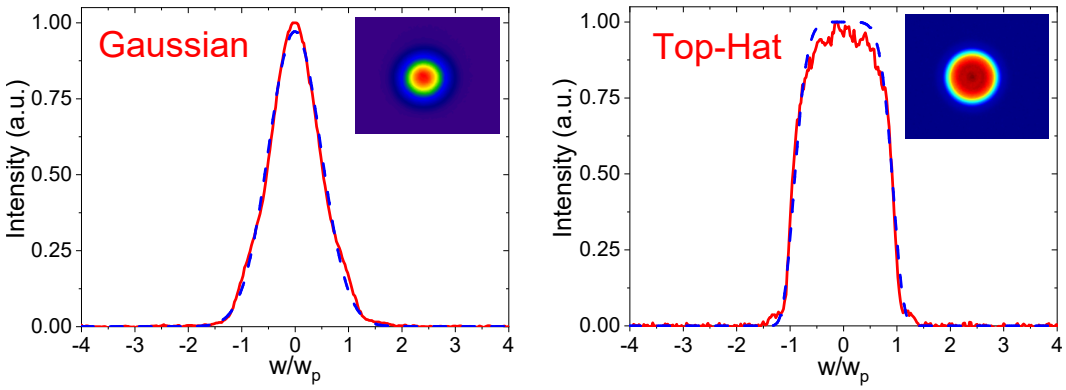

(a) (b)

Figure 6.2: Measured (shown in red) and theoretical fitting (shown in blue) pump profile for (a) Gaussian pump (b) Top-Hat pump ($n = 6$ Super Gaussian).

second pump delivery setup $d = f_c + f_p$ and a relay-lens pair of focal length f_r was used to directly image the fibre-output to give a 'top-hat' pump profile as shown in Fig. 6.2(b). The 'top-hat' profile matches well to a Super-Gaussian profile with $n = 6$.

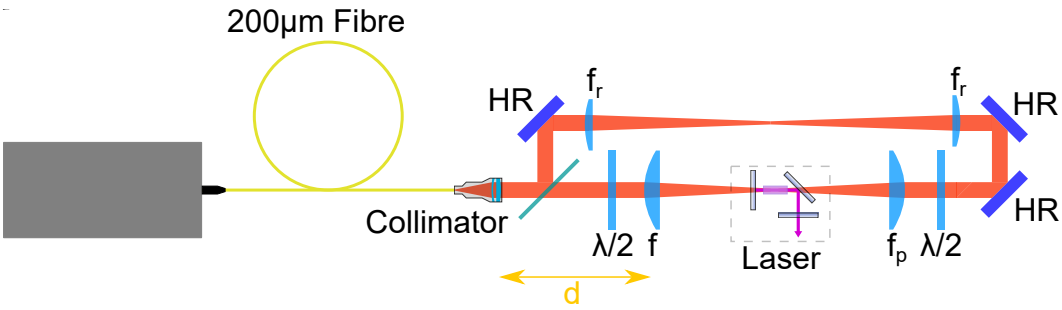

Figure 6.3: Pump delivery for double-end-pumping.

6.2 Plane-Plane Compact Alexandrite Laser

Figure 6.4 shows the experimental setup for the dual-end-pumped Alexandrite laser. An L-shaped laser cavity was used with three plane mirrors: a back mirror (BM) that was highly reflective (HR) at the laser wavelength and highly transmissive (HT) at the pump wavelength at 0°; a dichroic turning mirror (DM) used at 45° that was HR at the laser wavelength and HT at the pump wavelength; and an output coupler (OC) with partial transmission at the laser wavelength. The overall physical cavity length was $\sim 20\,\text{mm}$. The Alexandrite crystal was a $4 \times 4\,\text{mm}$ square aperture, 6 mm long c-cut slab with 0.20 at.% Chromium-doping and anti-reflection coated end faces at the laser and pump wavelengths. The crystal was mounted in a water-cooled copper heat sink for temperature control.

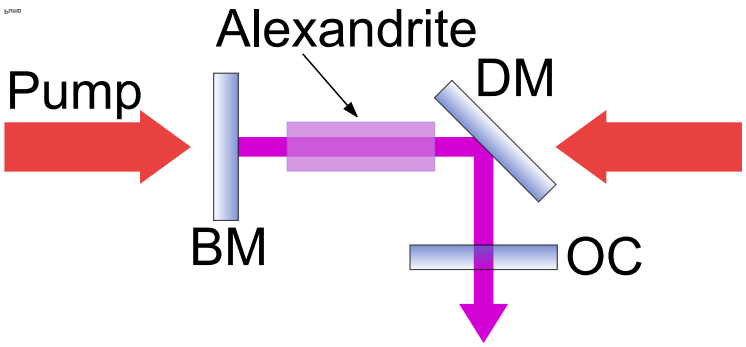

Figure 6.4: Fibre-delivered double-end-pumped compact L-shaped Alexandrite laser.

The laser cavity was pumped using both the Gaussian and top-hat pump profile. For the Gaussian pump-profile two aspheric lenses of focal length $f_p = 50\,\text{mm}$ were used to focus the pump beam to a waist radius of $w_p = 150\,\mu\text{m}$ with a Rayleigh

range of around $z_R = 1\,\text{mm}$. Almost all of the pump was absorbed at each end of the crystal (>98 % absorbed power). The temperature of the crystal was set to 60 °C and the OC had a reflectivity of $R_{OC} = 98.0\,\%$.

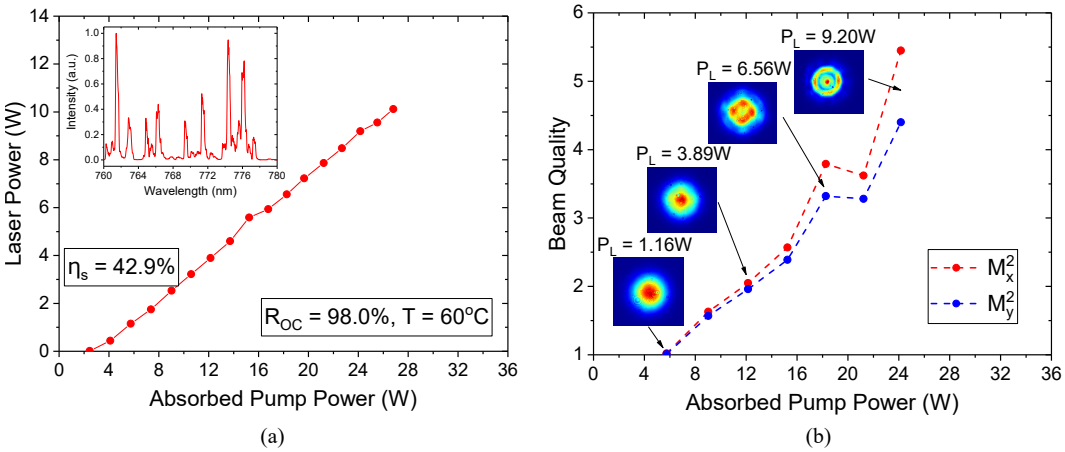

Figure 6.5: Double-end-pumped Gaussian pumping results of Alexandrite laser: (a) laser power, and (b) laser beam quality as a function of absorbed pump power.

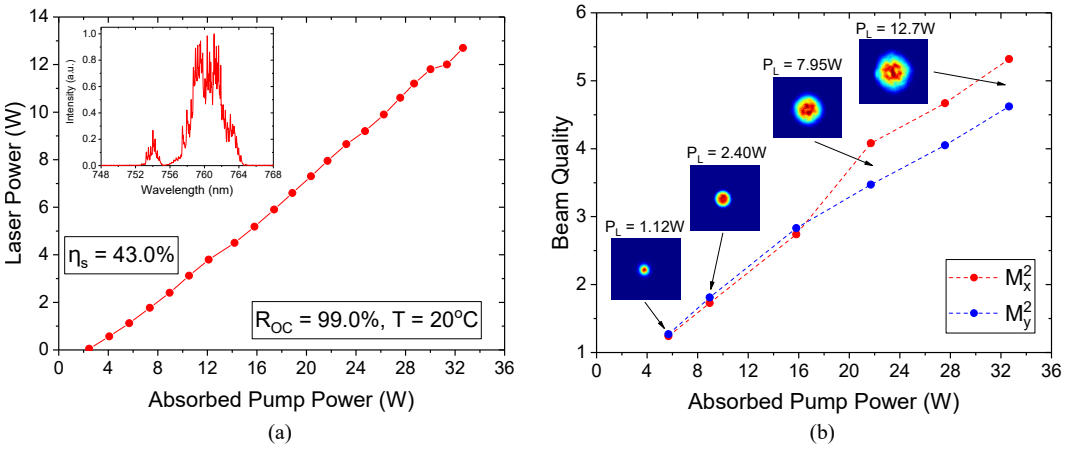

Figure 6.6: Double-end-pumped top-hat pumping results of Alexandrite laser: (a) laser power, and (b) laser beam quality as a function of absorbed pump power.

Figure 6.5(a) shows the laser power as a function of the absorbed pump power using the Gaussian pump configuration. 10.1 W of laser power was obtained at an absorbed pump power of 26.8 W with an overall slope efficiency of 42.9 % and no indication of thermal roll-over. The inset in Fig. 6.5(a) shows the laser spectrum at maximum power, which was highly modulated, though the spectrum was typically

broad and shifted to longer wavelengths with increased pump power.

Figure 6.5(b) shows the laser beam quality as a function of the absorbed pump power which was measured at seven pump powers. The beam profile and laser power is shown for four measurements. At an absorbed pump power of 5.8 W the laser power was 1.2 W and the beam quality $M_x^2 = 1.02$ and $M_y^2 = 1.01$. This result is similar to those obtained previously for compact plane-plane cavities (e.g. [90, 104]). At higher pump powers however, the laser beam quality rapidly degrades to $M_x^2 = 2.05$, $M_y^2 = 1.96$ at 3.9 W of laser power and $M^2 \sim 5$ at 9.2 W.

The degradation in laser beam quality is due to the increase in pump-induced lensing which decreases the laser mode size at the crystal. For optimal mode-matching higher order modes are preferential at higher power therefore leading to an increase in the measured beam quality. At high pump power, the effect of spherical aberration is also manifest in the appearance of Laguerre-Gaussian modes, demonstrating the excellent cylindrical symmetry of the pump beam.

Spherical aberration can be mitigated using a top-hat pump profile. To investigate the effect of improving the laser beam profile with minimised spherical aberration the experiment was repeated except with the pump delivery changed to an ashperic lens of focal length $f_p = 79$ mm that was placed at $d = 114$ mm to relay image the fibre output. The measured waist radius and Rayleigh distance were $w_p = 225$ µm and $z_R = 2.5$ mm, respectively. The cavity setup was the same as that shown in Fig. 6.4 except with $R_{\mathrm{OC}} = 99.0\,\%$ and with the water temperature at 20 °C.

Figure 6.6(a) shows the laser power as a function of the absorbed pump power for the top-hat profile pump. A maximum 12.7 W of laser power was obtained at an absorbed pump power of 32.6 W (increased drive current compared to previous setup) with an overall slope efficiency of 43.0 %. Figure 6.6(b) shows the laser beam quality measured at six different pump powers. At an absorbed pump power of 5.8 W the laser power was 1.1 W and the beam quality $M_x^2 = 1.24$, $M_y^2 = 1.27$ - similar to the previous setup. With increased pump power the beam quality also degraded with $M_x^2 = 5.32$, $M_y^2 = 4.62$ at 12.7 W of laser power. The laser beam profile at high pump power suggests that Laguerre-Gaussian modes were no longer present (with elimination of spherical aberration). This therefore demonstrates the improved performance in minimising aberrations. However, the degradation in beam quality remained. Both results demonstrate the limitation in the use of the plane-plane cavity regardless of the pump-profile due to the limitation in mode size control

for TEM_{00} operation at the multi-watt power level. It is therefore essential to design a compact and simple cavity design providing mode size control and mitigation of strong pump-induced lensing.

6.3 Single-end-pumped TEM_{00} Alexandrite Laser

Efficient TEM_{00} operation requires the matching of the pump and TEM_{00} laser mode sizes at the gain medium. The pump mode size at focus is determined by the focal length of the pump lens (with the input pump beam size fixed) and the laser mode size depends on the cavity geometry - as outlined in Chapter 2. It is therefore necessary to model the laser mode size at the gain medium as a function of the cavity parameters that are varied, most importantly the variation in the pump-induced lens which cannot be avoided when power-scaling.

There are a number of ways to design a power-scaled laser cavity. A common approach is to use a thin disk gain medium which minimises the transverse temperature gradients. The nearly uniform temperature gradient has little effect on the beam propagation [27]. This technique has revolutionised the level of TEM_{00} output power from solid-state gain media but is mainly focused on Yb-doped material due to its very small quantum defect and high doping concentrations. Work on thin disk near-infrared vibronic lasers is in progress but with limited results. Laser operation has been achieved for Ti:Sapphire but only up to the 10 W-level [122, 123]. Demirbas et al. has studied the theoretical capability of thin-disk Cr:Colquiriites [124] and Alexandrite [76], proposing that up to 80 W of CW laser operation is possible but with stringent requirements on the disk thickness and requires kW-level red laser diodes which are not commercially available.

Alternatively, the use of a convex mirror has proven to be an effective method of compensating pump-induced lensing in TEM_{00} lasers and is typically used in high-power end-pumped lasers as it provides high sensitivity to changes in the pump-induced lens dioptric power [35, 125–127]. A two or three-mirror convex-plane cavity has the additional benefit of maintaining a compact setup and removes the requirement of the additional optics necessary in thin-disk laser oscillators, thereby minimising the loss which is a crucial requirement in Alexandrite lasers due to its low gain. No special care is needed in fabricating extremely low loss optics and thin-disk Alexandrite crystals, thereby making the design simpler and lower-cost.

6.3.1 TEM_{00} Cavity Model

Figure 6.7 shows the convex-plane cavity used for high-power TEM_{00} operation. A convex mirror with curvature R was used as the dichroic back mirror (BM) for laser mode size control and mitigation of the pump-induced lens. A plane output coupler (OC) was used as the other cavity mirror.

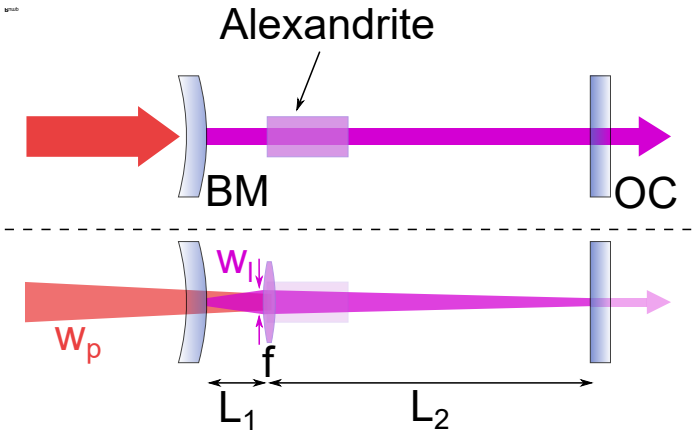

Figure 6.7: Single-end-pumped Alexandrite laser setup and model with pump-induced lens of focal length f.

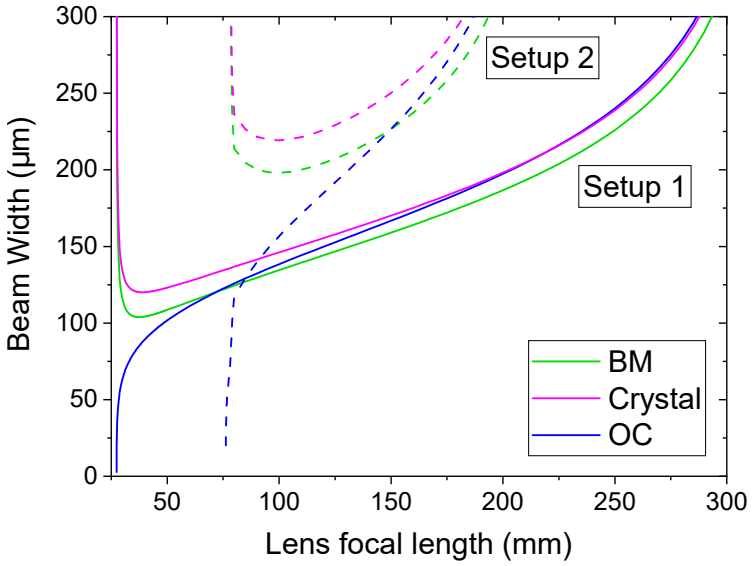

Figure 6.8: Beam width at BM, Alexandrite crystal and OC as a function of lens focal length.

Analytical expression for the stability and mode size for this cavity can be easily obtained using Eqs. (2.21)-(2.26) with $R_1 = R$, $R_2 \to \infty$ and modelling the Alexandrite crystal as a thin-lens of focal length f located at the pump-face of the crystal. Distances, L_1 and L_2 denote the spacing of each element as shown in Fig. 6.7. Two cavity configurations can be considered to visualise the dependence of the laser mode size on the cavity geometry. In Setup 1: $R = -300\,\text{mm}$, $L_1 = 20\,\text{mm}$ and $L_2 = 30\,\text{mm}$. In Setup 2: $R = -200\,\text{mm}$, $L_1 = 20\,\text{mm}$ and $L_2 = 100\,\text{mm}$.

Figure 6.8 shows the laser beam width at the BM, lens (or Alexandrite crystal) and OC as a function of lens focal length, f. Setup 1 is a relatively compact setup. The cavity is stable when $f \approx 300\,\text{mm}$ and the laser mode size is relatively collimated inside the cavity. With reducing lens focal length (increased pump-induced lens dioptric power) the laser mode size decreases. At the edge of stability (at around $f \approx 25\,\text{mm}$) the laser mode size approaches zero at the OC and maximises at the crystal and BM.

A similar behaviour is observed in Setup 2. Due to the stronger curvature of the BM, the edge of stability is at a lens focal length of $f \approx 200\,\text{mm}$. The variation in mode size with respect to the lens focal length is similar to that in Setup 1 with a couple of important exceptions. Firstly, the mode size is in general larger. This is due to the fact that the mode size is proportional to the cavity length. For longer cavity lengths it is therefore necessary to increase the pump waist size to maintain an efficient overlap of the pump and laser mode. The second difference is that the region of cavity stability is reduced (Setup 2 is unstable at around $f \approx 70\,\text{mm}$). It is therefore important to know the range of the pump-induced lens focal length to ensure that it is strong enough to enable lasing but not too strong such that the laser cavity goes unstable or that there is a detrimental change in the mode overlap at the crystal.

6.3.2 TEM_{00} Compact Cavity

For the first experimental setup a single-end-pumped compact cavity was chosen for simplicity. A $f_c = 35\,\text{mm}$ collimator and $f_p = 50\,\text{mm}$ aspheric pump lens were used to focus the pump beam onto the crystal. The collimator and pump lens were separated by around $d = 85\,\text{mm}$ to ensure the fibre output was imaged onto the crystal for a 'top-hat' pump profile as shown previously in Section 6.1. The pump waist radius was measured to be $w_p = 150\,\mu\text{m}$ with a Rayleigh range of $z_R = 1\,\text{mm}$ for optimal absorption [102] and mode-matching. A plate polariser was placed

between the collimator and pump lens to provide a linearly polarised pump beam, with the reflected beam safely dumped. The polarisation of the transmitted beam was rotated to the high absorbing b-axis using a halfwave plate.

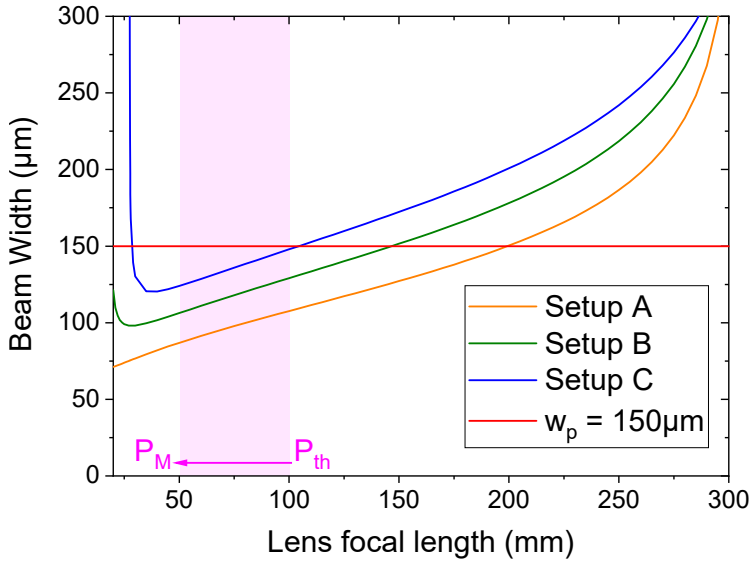

Figure 6.9: Laser beam width at the crystal as a function of lens focal length for Setup A, B and C. Shaded region indicates the range of the measured pump-induced lens focal length.

Three cavity configurations were investigated: Setup A, B and C. All are the same design shown in Fig. 6.7 with a convex mirror of curvature $R = -300\,\text{mm}$, an OC of reflectivity $R_{\text{OC}} = 98.0\,\%$ and a temperature of 10 °C. However the cavity length was varied with three different mirror separation lengths analysed. For Setup A: $L_1 = 5\,\text{mm}$, $L_2 = 10\,\text{mm}$; Setup B: $L_1 = 10\,\text{mm}$, $L_2 = 20\,\text{mm}$ and; Setup C: $L_1 = 20\,\text{mm}$, $L_2 = 30\,\text{mm}$. Figure 6.9 shows the laser mode size at the crystal as a function of f for the three configurations. For each setup, mode-matching is achieved at different focal lengths, it is therefore important to know the range of the pump-induced lens focal length over the lasing range. To precisely determine the dioptric power, the direct wavefront measurement technique with a probe beam and Shack-Hartmann wavefront sensor was used (as described in Chapter 5).

Figure 6.10 shows the measured pump-induced lens dioptric power as a function of the absorbed power under non-lasing and lasing conditions. As found previously, the measured lens dioptric power was found to be significantly weaker under lasing conditions. At laser threshold ($P_{th} = 4.35\,\text{W}$) the dioptric power was $D = 10.2\,\text{m}^{-1}$

($f \approx 100\,\mathrm{mm}$) increasing to $D = 18.3\,\mathrm{m}^{-1}$ ($f \approx 50\,\mathrm{mm}$) at a maximum absorbed pump power of $P_M = 13.4\,\mathrm{W}$. This region is indicated in Fig. 6.9 showing that optimal mode-matching is obtained for Setup C.

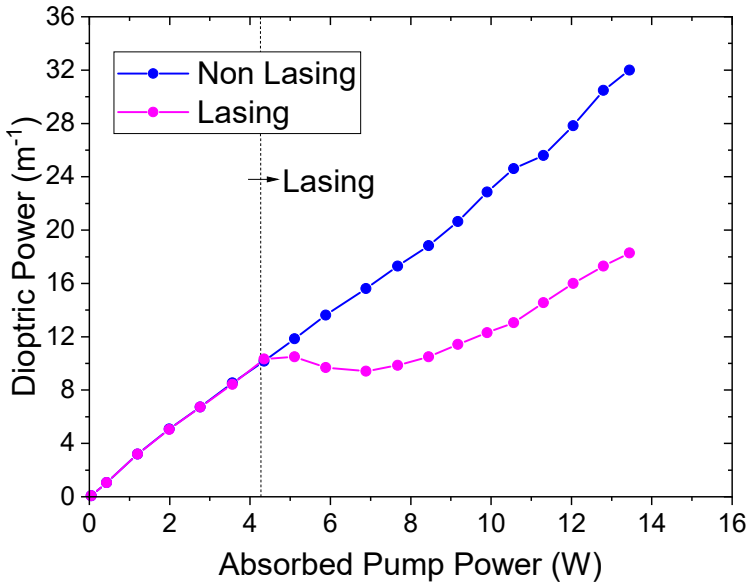

Figure 6.10: Shack-Hartmann measured lens dioptric power of pump-induced lens as a function of the absorbed pump power under both non-lasing and lasing conditions with $w_p = 150\,\mu\mathrm{m}$.

Figures 6.11-6.13 show the laser power as a function of the absorbed pump power and the laser beam quality at maximum pump power for Setup A, B and C. For Setup A, 4.4 W was obtained with the beam quality $M^2 = 2.2$. In Setup B, 4.7 W was obtained with an improved beam quality of $M^2 = 1.3$ and a record slope efficiency for a red-diode-pumped Alexandrite laser of 54.9 %. This result demonstrates the improved efficiency and mode quality obtained by improving the overlap between the pump and laser modes. In Setup B the mode quality was improved further to $M^2 = 1.2$ although with a reduced output power of 4.3 W and slightly reduced efficiency. With the drive current increased further, 5 W was obtained at an absorbed pump power of 16.0 W. The roll-over in power observed in Fig. 6.13 is due to the change in laser mode size as the increase in the pump-induced lens (at $f \leq 50\,\mathrm{mm}$) shifts the cavity toward instability as shown in Fig. 6.9.

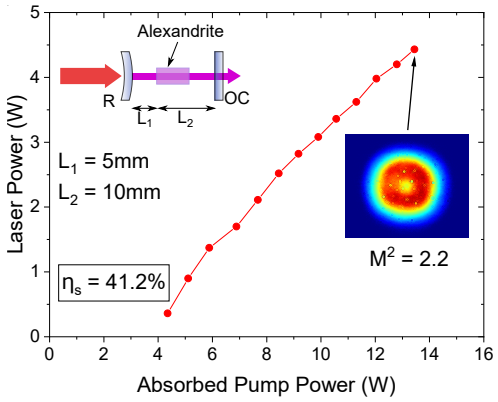

Figure 6.11: Single-end-pumped Alexandrite laser: Setup A.

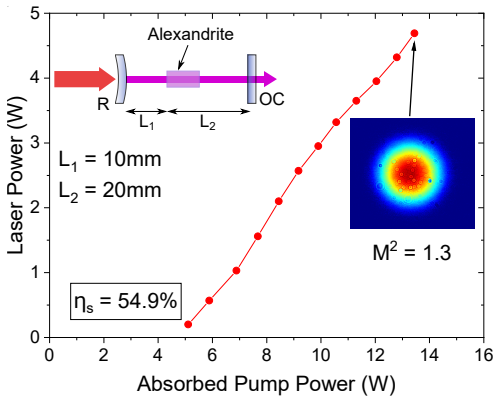

Figure 6.12: Single-end-pumped Alexandrite laser: Setup B.

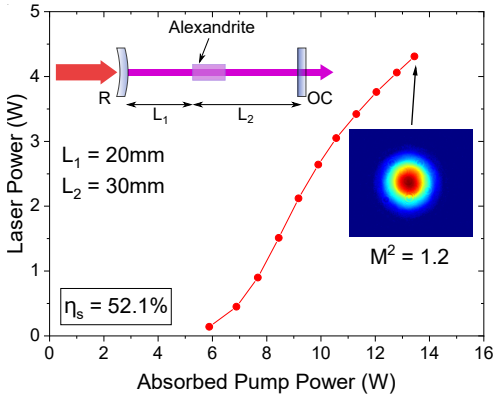

Figure 6.13: Single-end-pumped Alexandrite Laser: Setup C.

6.3.3 TEM_{00} Alexandrite Laser with Wavelength Tuning

For wavelength tuning, additional space between the crystal and OC was required for mounting the birefringent filter (BiFi). The pump waist size was increased to $w_p = 225\,\mu m$ using an aspheric pump lens of focal length $f_p = 79\,mm$ to provide better matching to the larger laser mode size. No measurement of the pump-induced lens was made with the new pump waist radius, however using the results obtained previously (Fig. 6.10) and the model in Chapter 5, an estimate was calculated. At a threshold absorbed pump power of around $P_{th} = 10.5\,W$ the lens focal length was estimated to be $f \approx 175\,mm$, and at the maximum absorbed pump power of $P_M = 16.3\,W$ the lens focal length was $f \approx 100\,mm$.

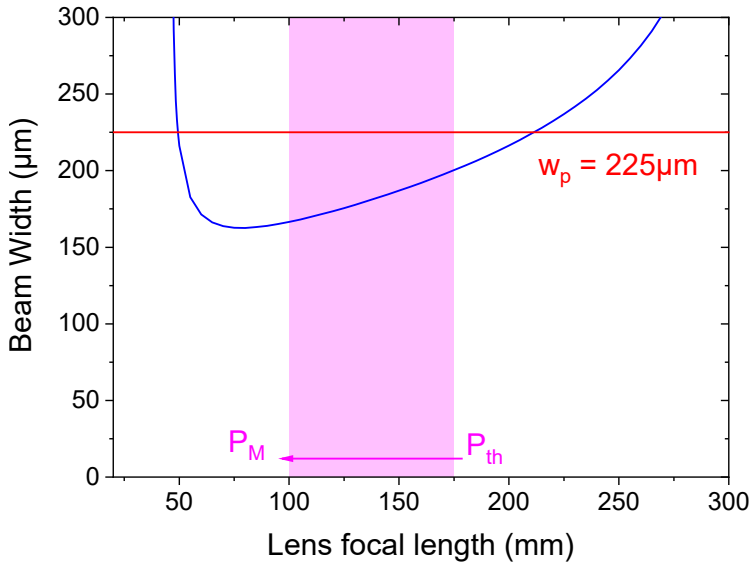

Figure 6.14: Laser beam width at the crystal as a function of lens focal length for $R = -300\,mm$, $L_1 = 5\,mm$ and $L_2 = 55\,mm$. Shaded region indicates the range of the theoretical pump-induced lens focal length.

Figure 6.14 shows the beam width at the crystal as a function of lens focal length for $R = -300\,mm$, $L_1 = 5\,mm$ and $L_2 = 55\,mm$. The theoretical range of the pump-induced lens focal length is indicated in Fig. 6.14. It shows that the laser mode under-fills that of the pump for this cavity configuration. However, the previous system showed promising results with the laser mode size slightly under-filling the pump and so the cavity was designed with $L_1 = 5\,mm$ and $L_2 = 55\,mm$.

Figure 6.15 shows the laser power as a function of the absorbed pump power

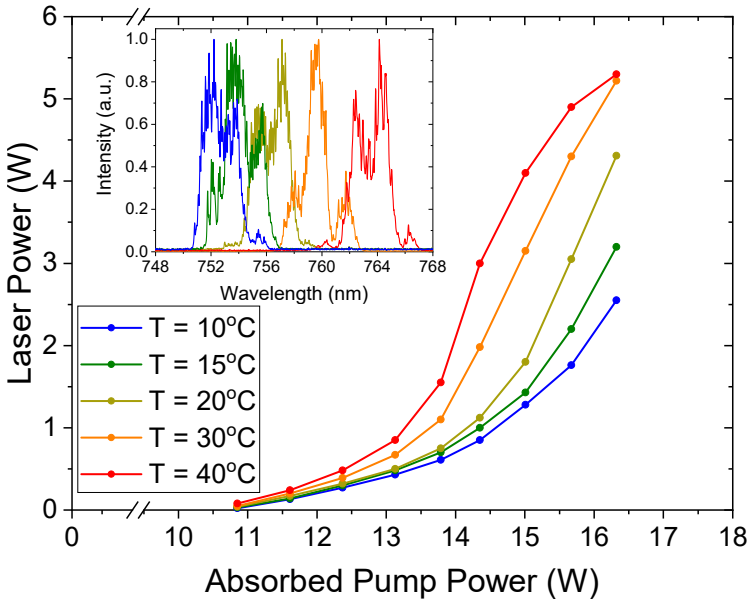

Figure 6.15: Laser power as a function of absorbed pump power for $R = -300\,\text{mm}$, $L_1 = 5\,\text{mm}$ and $L_2 = 55\,\text{mm}$ at five temperatures.

at five temperatures. Laser threshold decreased slightly with increased temperature but was roughly at an absorbed pump power of around $P_{th} = 10.5\,\text{W}$. At 10 °C, a maximum laser power of 2.55 W was obtained at 16.3 W with a beam quality of $M^2 \leq 1.2$. Increasing the temperature increased the maximum output power to 3.2 W, 4.3 W, 5.2 W and 5.3 W at 15 °C, 20 °C, 30 °C and 40 °C, respectively, with no change in beam quality. The laser spectrum at maximum power (shown in inset of Fig. 6.15) was broad with a linewidth of around 2 nm and a central peak of around 753 nm, 754 nm, 756 nm, 760 nm and 764 nm at 10 °C, 15 °C, 20 °C, 30 °C and 40 °C, respectively. Increased efficiency and a red-shift in wavelength are expected in Alexandrite due to the temperature dependence of the effective emission cross section - as outlined in Chapter 3. However, the efficiency improvement observed here is drastically greater than that expected purely based on the change in the effective emission cross section. Further analysis of the temperature effect is therefore necessary and is discussed later in Section 6.5.

A 0.5 mm quartz BiFi placed at Brewster's angle was used to tune the wavelength with the crystal temperature at 30 °C. Figure 6.16 shows the optimum laser power as a function of the absorbed pump power for the cavity with the BiFi. A maximum 4.7 W was obtained at an absorbed pump power of 16.3 W with an excellent beam

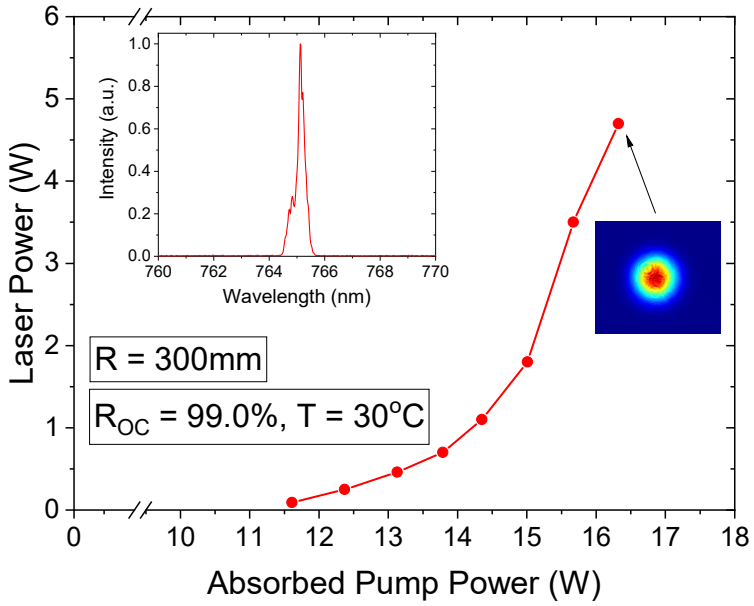

Figure 6.16: Laser power as a function of absorbed pump power for $R = -300\,\text{mm}$, $L_1 = 5\,\text{mm}$ and $L_2 = 55\,\text{mm}$ with BiFi at 30 °C.

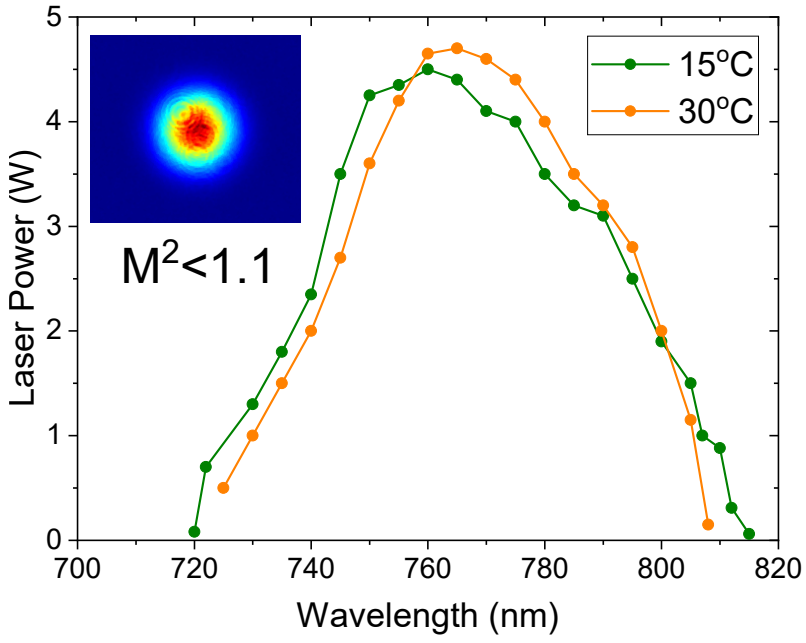

Figure 6.17: Laser power as a function of wavelength for 0.5 mm BiFi.

quality of $M_x^2 = 1.03$ and $M_y^2 = 1.07$. The spectrum was centred at 765.1 nm with a resolution-limited linewidth of 0.3 nm.

Figure 6.17 shows the laser power as a function of the laser wavelength at 15 °C and 30 °C. For the latter, continuous tuning between 725 and 808 nm was achieved with >1 W over 730-805 nm for the very first time in a red-diode-pumped Alexandrite laser, and with >4 W over the central region 755-780 nm. Near diffraction limited output ($M^2 < 1.1$) and a resolution-limited linewidth of < 1 nm were measured over the entire tuning range. Similar results were obtained at 15 °C but with slightly broader tuning at 720-815 nm. The general red-shift in the two tuning curves with increased temperature is in agreement with the emission cross-section red-shift (as shown in Fig. 3.11 in Chapter 3).

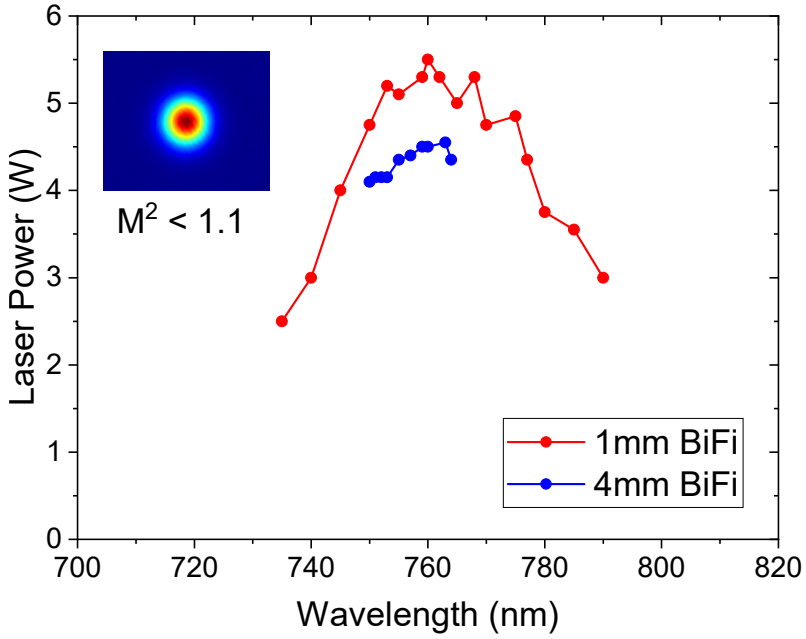

Figure 6.18: Laser power as a function of wavelength for 1 mm and 4 mm BiFi.

1 mm and 4 mm thick BiFis where also used to investigate the wavelength tuning and dual wavelength performance of the cavity. Figure 6.18 shows the laser power as a function of the wavelength for the two BiFis with the cavity setup unchanged and the temperature at 20 °C. With the 1 mm BiFi 735-790 nm continuous wavelength tuning was obtained with >5 W at 753-768 nm. Dual wavelength operation with 57 nm peak-to-peak separation was achieved with an output power of around 2.75 W.

Figure 6.19 shows the laser spectrum at dual wavelength operation.

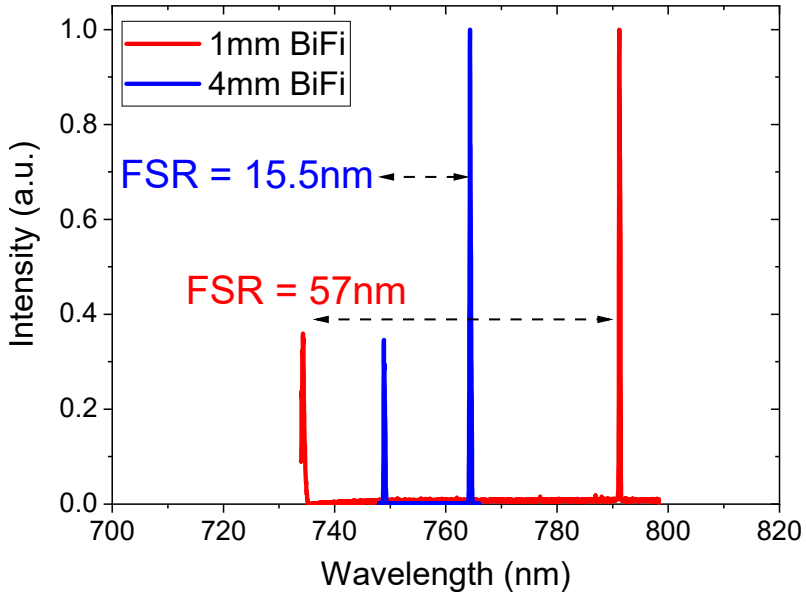

Figure 6.19: Laser spectrum at dual wavelength operation for 1 mm and 4 mm BiFi.

750-764 nm tuning with >4 W was obtained with the 4 mm thick BiFi, also shown in Fig. 6.18. Dual wavelength operation with around 4.2 W of output power was obtained with a peak-to-peak separation of 15.5 nm, as shown in Fig. 6.19. These results demonstrate an alternative method of generating dual-wavelength output using an Alexandrite laser.

6.3.4 TEM_{00} Alexandrite Laser with VBG-locked Wavelength

Narrow-linewidth and fixed wavelength laser operation was also investigated using the single-end-pumped Alexandrite laser setup. One simple method is to use a volume Bragg grating (VBG) as a high reflective mirror [128]. Figure 6.20(a) shows the single-end-pumped Alexandrite laser setup for narrow-linewidth operation. The initial cavity was identical to that used previously (see Fig. 6.9) except with the OC at a 45° angle of incidence and an additional HR mirror. The pump spot size and Rayleigh length were $w_p = 150\,\mu m$ and $z_R = 1\,mm$, respectively, and the cavity lengths $L_1 = 5\,mm$ and $L_2 = 25\,mm$. For narrow linewidth operation the HR mirror was replaced with a $2 \times 2\,mm^2$ aperture, 3.6 mm long reflective Bragg grating with >98 % diffracting efficiency and a central wavelength of around 760 nm.

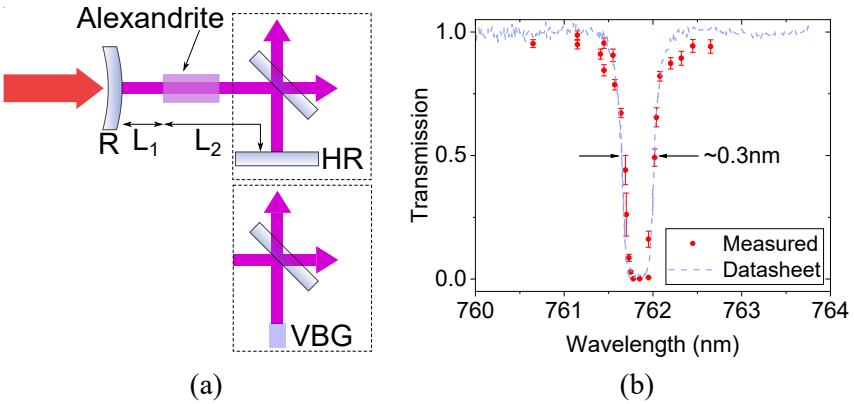

Figure 6.20: (a) Three-mirror Alexandrite laser with VBG mirror. (b) Measured VBG transmission spectrum.

The VBG reflection at around 760 nm was characterised using the birefringent tuning Alexandrite laser demonstrated in Chapter 4. The laser was focused to 80 µm radius (25 mm Rayleigh length) at an output power of around 0.5 W. The measured transmission, shown in Fig. 6.20(b), matched well to the datasheet provided confirming the VBG has a FWHM of around 0.3 nm centred at 761.8 nm. The measured transmission, however, was much lower than expected at 0.1 % making it ideal as a HR mirror.

Figure 6.21 shows the laser power as a function of the absorbed pump power for the cavity with the HR mirror. 5.2 W was obtained at 15.7 W absorbed pump power using the $R_{OC} = 97.0\,\%$ (at 45°) OC. Considerably different behaviour was observed for the different OCs - this too will be discussed in greater detail in Section 6.5. A broad laser emission was observed for each OC, as shown in the inset of Fig. 6.21.

Figure 6.22 shows the laser power as a function of the absorbed pump power with the VBG (and with $R_{OC} = 97.0\,\%$). 3.25 W was obtained at 17 W absorbed pump power and a near diffraction limited output of $M^2 = 1.1$. The laser linewidth was estimated using a Fabry-Perot etalon (FSR = 6.9 GHz). The Fabry-Perot interference pattern (see inset of Fig 6.22) showed that two longitudinal modes were lasing. The laser linewidth was estimated to be around 1 GHz.

This result further demonstrates the flexible performance of the convex-plane cavity in providing high power and high efficiency TEM_{00} lasing from an Alexandrite laser. This is the very first demonstration of a VBG-locked Alexandrite laser and can be easily adapted into configurations that provide a single output and narrow-

linewidth wavelength tuning using an angled [129] or chirped VBG [130].

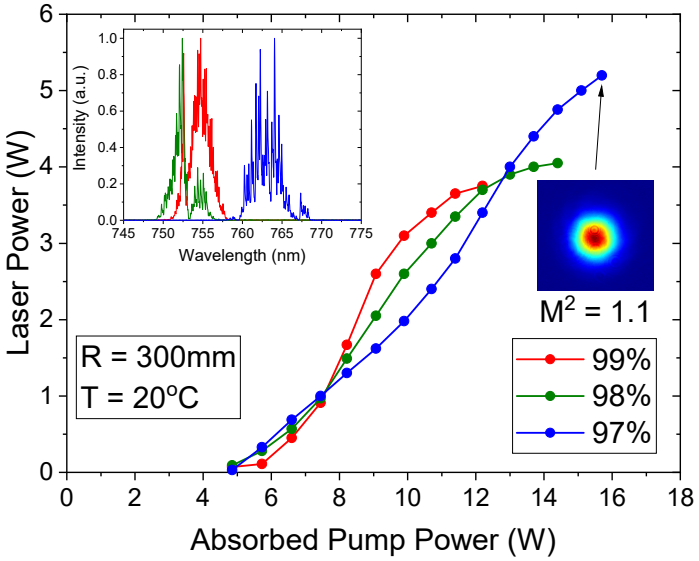

Figure 6.21: Laser power as a function of absorbed pump power with $R = -300\,\text{mm}$, $L_1 = 5\,\text{mm}$ and $L_2 = 25\,\text{mm}$ at 20 °C. OC reflectivity were measured for s-polarisation at 45°.

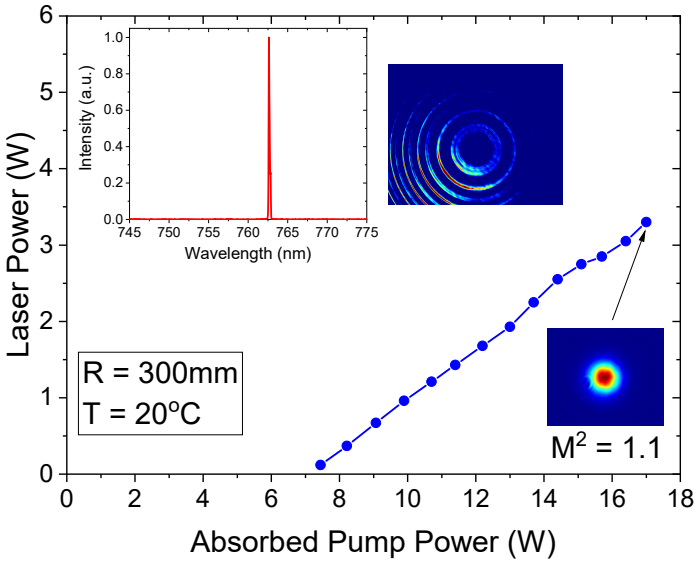

Figure 6.22: Laser power as a function of absorbed pump power for VBG-locked cavity with $R = -300\,\text{mm}$, $L_1 = 5\,\text{mm}$ and $L_2 = 25\,\text{mm}$ at 20 °C with $R_{\text{OC}} = 97.0\,\%$.

6.4 Dual-end-pumped TEM_{00} Alexandrite Laser

For further power scaling the two pump arms were used in a double-end-pumping configuration, as depicted in Fig. 6.3. This provided up to 36 W of absorbed pump power.

6.4.1 Single-Convex Mirror Design

In this setup, the cavity design was unchanged compared to that in Section 6.3.2 except for the addition of a 45° DM to produce an L-shaped cavity. For better management of the pump-induced lens a stronger convex back mirror with curvature $R = -200\,\text{mm}$ was used. The pump waist size and mirror positions were set to $w_p = 225\,\text{mm}$, $L_1 = 5\,\text{mm}$ and $L_2 = 55\,\text{mm}$. The output coupler reflectivity was $R_{\text{OC}} = 99.0\,\%$.

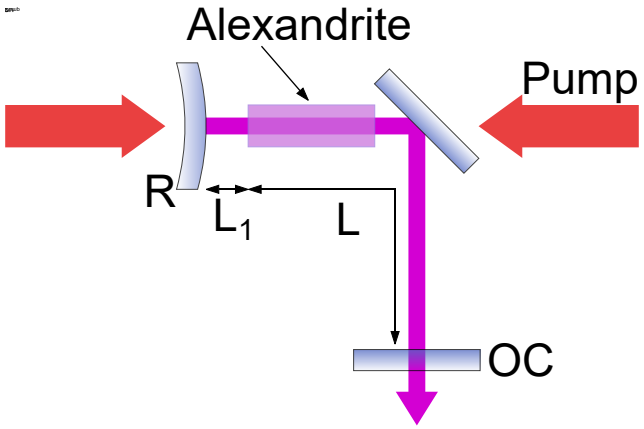

Figure 6.23: Double-end-pumped TEM_{00} Alexandrite laser setup.

Figure 6.24 shows the laser power as a function of the absorbed pump power for the dual-end-pumped TEM_{00} cavity at three temperatures. Threshold was at an absorbed pump power of around 14 W - an increase compared to the previous threshold of 10.5 W (when using $w_p = 225\,\text{mm}$) due to the stronger $R = -200\,\text{mm}$ mirror. The results show the maximum laser power achieved, beyond these values thermal roll-over was observed. A maximum laser power of 7.4 W at an absorbed pump power of 26.3 W was obtained at 10 °C. The measured beam quality was $M_x^2 = 1.12$ and $M_y^2 = 1.04$.

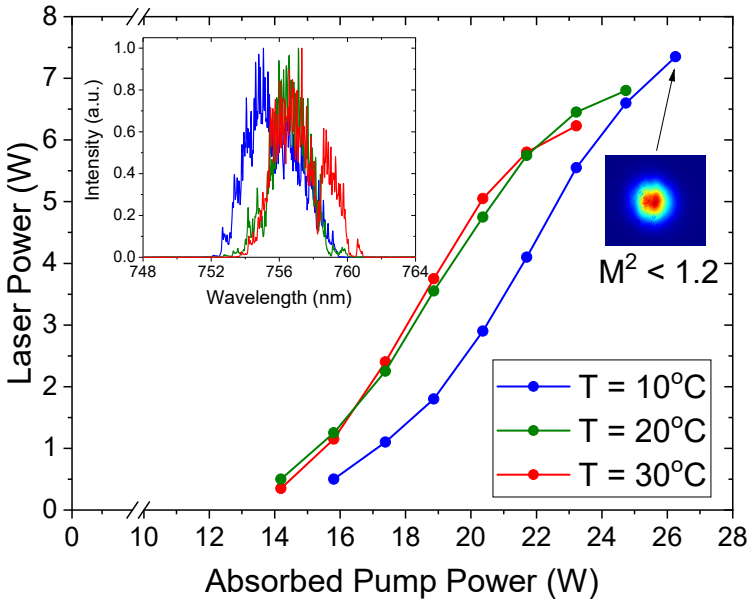

Figure 6.24: Laser power as a function of absorbed pump power for $R = -200\,\text{mm}$, $L_1 = 5\,\text{mm}$ and $L_2 = 55\,\text{mm}$ at three temperatures.

6.4.2 Double-Convex Mirror Design

An alternative design was to use two convex mirrors to compensate the pump-induced lens at either end of the crystal. Figure 6.25 shows a schematic of the experimental setup. The pump-delivery was unchanged with dual-end-pumping through one convex mirror at normal incidence and the second at an angle of incidence of around 20°. The two convex mirrors were placed at a distance of L_1 and L_{21} with respect to the left side of the crystal. The third mirror, the OC, was placed a distance L_{22} from the angled convex mirror.

The use of two convex mirrors and the lensing at both ends of the crystals make analytical modelling of the beam size difficult, therefore a numerical model was devised based on the ABCD Gaussian propagation model, as outlined in Chapter 2. Figure 6.26 shows the model for the cavity. The pump-induced lens on either side of the crystal are represented by thin lenses of focal length f and the two convex mirrors are of equal curvature $R = -300\,\text{mm}$ - the astigmatism of the second convex mirror was neglected. The mirror separations are denoted the same as in Fig. 6.25.

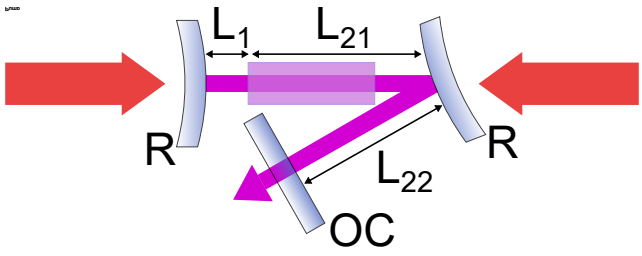

Figure 6.25: Double-end-pumped Alexandrite laser setup with two convex mirrors.

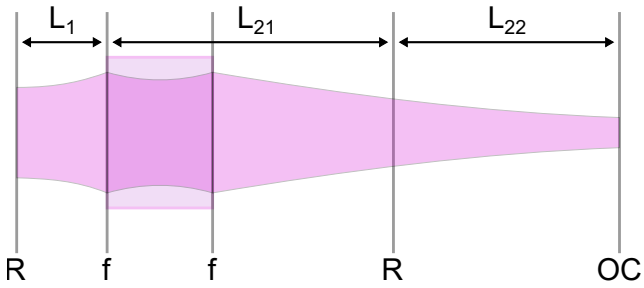

Figure 6.26: ABCD Gaussian propagation cavity model of double-convex Alexandrite laser cavity.

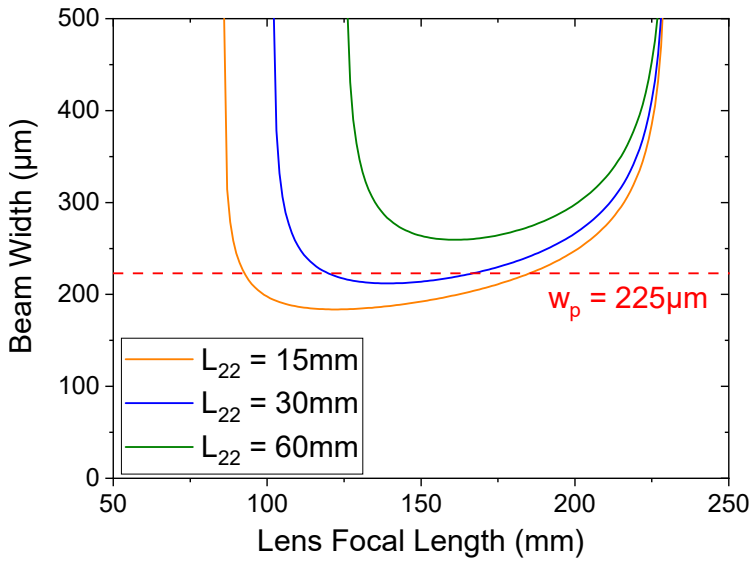

Figure 6.27: Laser beam width at the crystal as a function of lens focal length for $R = -300\,\text{mm}$, $L_1 = 5\,\text{mm}$ and $L_{21} = 35\,\text{mm}$.

For simplicity, $L_1 = 5\,\text{mm}$ and $L_{21} = 35\,\text{mm}$ were both fixed to fit the mirror and crystal mounts in-between the dual-end-pump setup, and the variation in L_{22} was investigated. Figure 6.27 shows the mode size (radius) at the crystal surface as a function the pump-induced lens focal length with $L_{22} = 15$, 30 and 60 mm. The cavity is stable from around $f = 230\,\text{mm}$ for all configurations with increasing regions of stability for shorter L_{22}.

The pump-induced lens focal length was estimated based on measurements of the laser mode size for the single-end-pumped convex-plane cavity in Fig. 6.7. This gave an estimate of a lens focal length of around 200-225 mm at 11.5 W of absorbed pump power (23 W dual-end-pumping) and around 130-180 mm at 16.5 W of absorbed pump power (33 W dual-end-pumping). The cavity geometry was therefore set to $L_1 = 5\,\text{mm}$, $L_{21} = 35\,\text{mm}$ and $L_{22} = 15\,\text{mm}$ to provide good matching to the pump size and cavity stability up beyond $f = 100\,\text{mm}$ as indicated in Fig. 6.27.

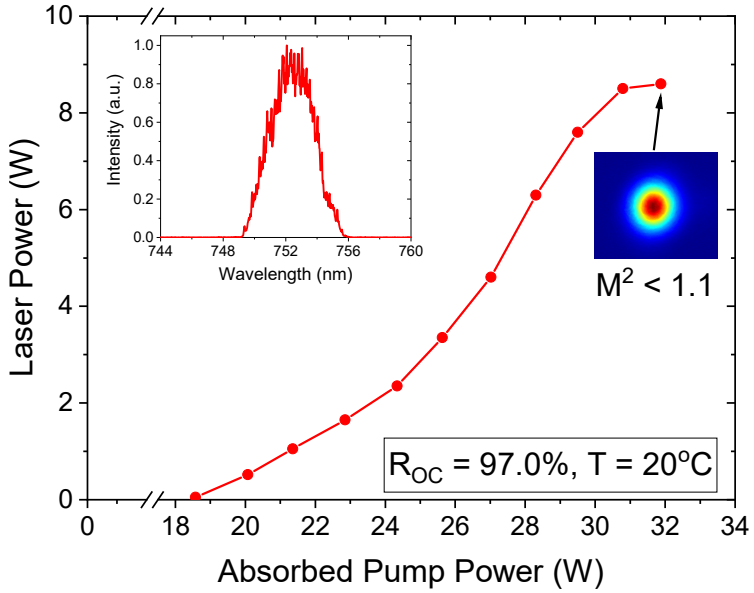

Figure 6.28: Laser power as a function of absorbed pump power for double-end-pumped Alexandrite laser with two convex mirrors.

Figure 6.28 shows the laser power as a function of the absorbed pump power for the laser cavity. Laser threshold was at an absorbed pump power of $P_{th} = 18.5\,\text{W}$. The laser power then increased at an increasing rate before settling at around 30 W of absorbed pump power and reaching a maximum of 8.6 W at 32 W with an excellent mode quality of $M^2 < 1.1$ in both directions. This result is the world-record for the

highest powered TEM_{00} diode-pumped Alexandrite laser.

The laser threshold was lower than expected (which was expected to be around 23 W), therefore suggesting the pump-induced lens focal length to be stronger than 200-225 mm. It's therefore likely that the pump-induced lens focal length at 32 W to be stronger than 100 mm which accounts for the roll-over in laser power as the cavity is approaching instability. Further optimisation in cavity geometry would therefore be possible in pushing TEM_{00} output powers to the 10 W-level.

6.5 Temperature and Output Coupling Dependence

Throughout this chapter several laser cavities using convex mirrors for mode size control have been presented. These designs have enabled record-levels of TEM_{00} output power for diode-end-pumped Alexandrite lasers. The primary advantage of these cavities is that the strong pump-induced lensing is used to its advantage by enabling large mode volumes at the gain medium. This inherent dependence on the pump-induced lens for cavity stability and efficient mode-matching tends to give non-linear power curves as the laser mode size changes at the gain medium.

Particular focus was therefore aimed at optimising the cavity configuration to produce the optimal mode-matching conditions at the highest pump power. This required an understanding of the focal length of the pump-induced lens which was obtained using the technique covered in Chapter 5 or using direct measurements of the laser mode size. The laser cavity was then optimised experimentally by varying the crystal temperature and using different OCs. The temperature dependence of Alexandrite lasers has been extensively recorded in the literature as discussed in Chapter 3 and has been studied recently in detail for diode-end-pumped systems by Kerridge-Johns et al. [90]. Variation in output coupling has also been studied by Kerridge-Johns et al. in [131]. In general, at wavelengths of around 750-770 nm peak performance is obtained at elevated temperatures (around 60 °C) and low output coupling (typically $R_{OC} \geq 99\,\%$). However, in this chapter there has been no consensus in the optimal temperature and output coupling as illustrated in Fig. 6.29 which shows power curves for various systems (some have already been presented) with the OC reflectivity and water temperature shown.

Figure 6.29(a) shows the power curve for the convex-plane laser cavity with $w_p = 150\,\mu m$. Optimal performance was achieved with $T = 10\,°C$ and $R_{OC} = 98.0\,\%$. However when increasing to $w_p = 225\,\mu m$, as shown in Fig. 6.29(b), optimal

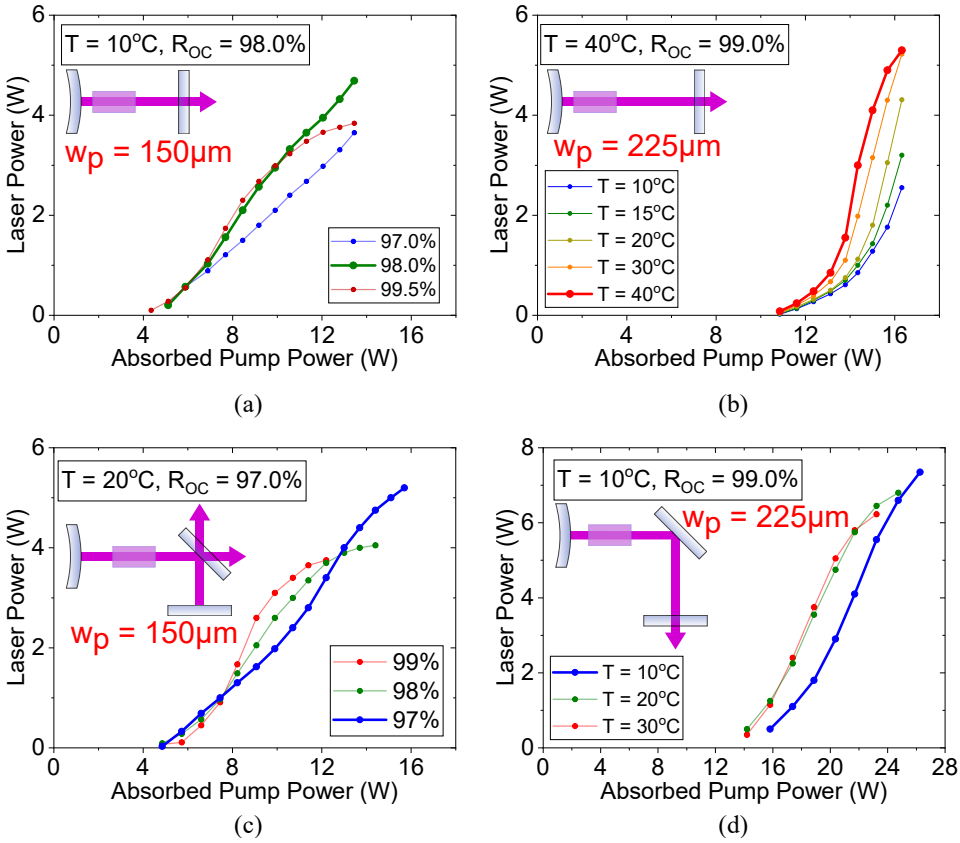

Figure 6.29: Optimal performance for different Alexandrite lasers. Optimal temperature and OC reflectivity were: (a) $T = 10\,^{\circ}\mathrm{C}$, $R_{\mathrm{OC}} = 98\,\%$. (b) $T = 40\,^{\circ}\mathrm{C}$, $R_{\mathrm{OC}} = 99\,\%$. (c) $T = 20\,^{\circ}\mathrm{C}$, $R_{\mathrm{OC}} = 97\,\%$. (d) $T = 10\,^{\circ}\mathrm{C}$, $R_{\mathrm{OC}} = 99\,\%$.

performance was at higher temperature and lower output coupling with $T = 40\,^{\circ}\mathrm{C}$ and $R_{\mathrm{OC}} = 99.0\,\%$. Here the onset of roll-over can be seen and under higher pump power, which is the case in Fig. 6.29(d), roll-over is mitigated by decreasing the temperatures down to $T = 10\,^{\circ}\mathrm{C}$. A similar effect is observed when comparing Figs. 6.29(a) and 6.29(c) where roll-over is observed when increasing the power with $R_{\mathrm{OC}} = 98.0\,\%$, and higher power can be obtained by increasing the output coupling.

Roll-over can be attributed to the cavity approaching instability or the laser mode size under-filling the pump region - both of which arise from the change in the pump induced lens. These results therefore suggest that the temperature and output coupling have a significant effect on the pump-induced lens. To test this,

a convex-plane cavity was built and the pump-induced lens measured using the Shack-Hartmann wavefront sensor (SH-WFS). The cavity was a single-end-pumped convex-plane cavity with $w_p = 300\,\mu m$, $R = -300\,mm$, $L_1 = 5\,mm$, $L_2 = 70\,mm$ and $R_{OC} = 99.0\,\%$.

Figure 6.30 shows the laser power as a function of the absorbed pump power at $T = 10\,^{\circ}C$ (blue) and $T = 40\,^{\circ}C$ (red). Threshold was at around 13.0 W and 12.5 W at $T = 10\,^{\circ}C$ and $T = 40\,^{\circ}C$, respectively. At $T = 10\,^{\circ}C$ the power grew gradually to a maximum power of 2.60 W, whereas the power at $T = 40\,^{\circ}C$ grew rapidly to a maximum power of 4.05 W. The measured beam quality at both temperatures was $M^2 < 1.2$ and the laser spectrum is shown in the inset of Fig. 6.30 - the red-shift in wavelength with increased temperature is again indicative of the shift in emission cross section with increased temperature.

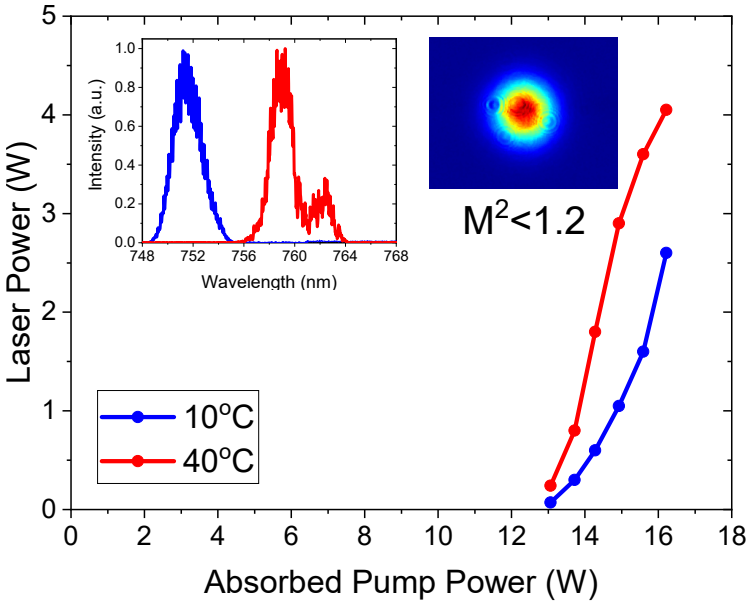

Figure 6.30: Laser power as a function of absorbed pump power with $w_p = 300\,\mu m$, $R = -300\,mm$, $L_1 = 5\,mm$, $L_2 = 70\,mm$ and $R_{OC} = 99.0\,\%$ at $T = 10\,^{\circ}C$ and $T = 40\,^{\circ}C$. Inset shows mode quality and laser wavelength at maximum power.

Figure 6.31 shows an overview of the SH-WFS results obtained for the cavity. Figure 6.31(a) shows the measured dioptric power as a function of the absorbed power under non lasing (grey) and lasing (blue) conditions at $T = 10\,^{\circ}C$. As with previously the dioptric power under lasing conditions is weaker than that under

non-lasing conditions. Under lasing conditions, the dioptric power is $5.3\,\mathrm{m}^{-1}$ ($f = 188\,\mathrm{mm}$) at maximum pump power. At $T = 40\,^{\circ}\mathrm{C}$ (Fig. 6.31(b)) the dioptric power is stronger both under non-lasing and lasing conditions compared to that at $T = 10\,^{\circ}\mathrm{C}$ with a dioptric power of $5.9\,\mathrm{m}^{-1}$ ($f = 169\,\mathrm{mm}$) at maximum pump power.

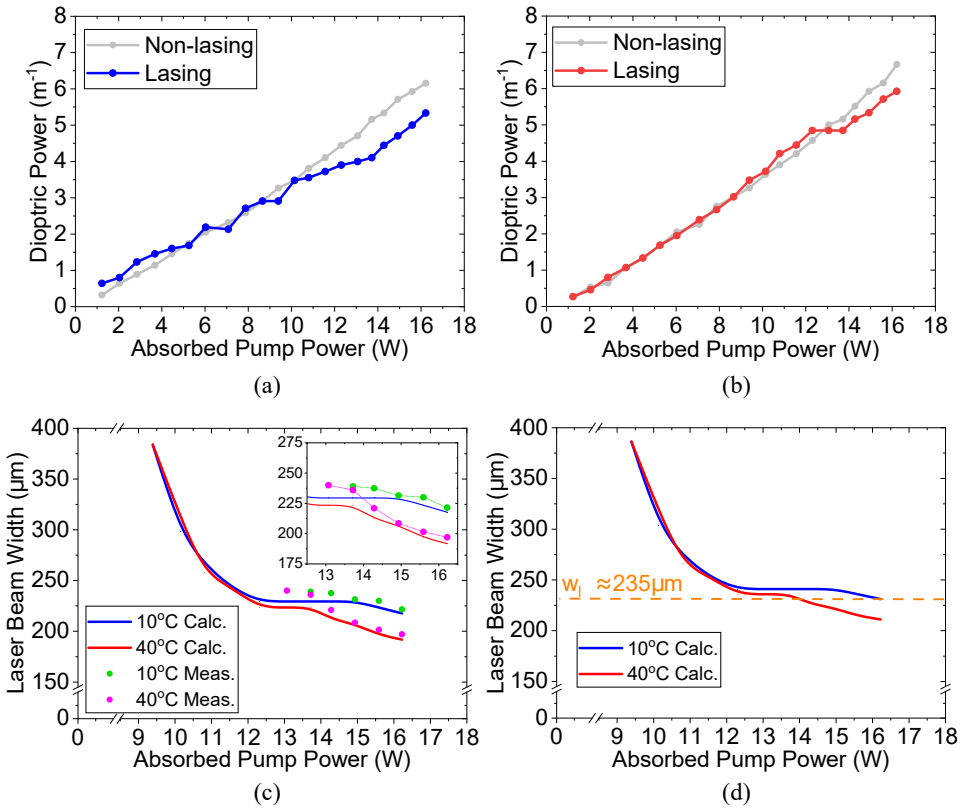

Figure 6.31: Shack-Hartmann measured lens dioptric power of pump-induced lens as a function of absorbed pump power with $w_p = 300\,\mu\mathrm{m}$ at: (a) $10\,^{\circ}\mathrm{C}$ (b) $40\,^{\circ}\mathrm{C}$. Calculated and measured laser beam width as a function of absorbed pump power at: (c) output coupler (d) crystal.

This result verifies that the pump-induced lens is temperature dependent. Its impact on the mode size is shown in Figs. 6.31(c) and 6.31(d) which show the laser beam width as a function of the absorbed pump power at the OC and crystal, respectively. In Fig. 6.31(c) the solid lines indicate the laser beam width at the OC based on the measured values of the dioptric power and calculated using Eqs. (2.25) and (2.26). The results show that the beam width at the OC is about the same for the two temperatures at around threshold (12-13.5 W) but then the stronger

lens at 40 °C leads to a smaller mode size with increasing pump power. The laser beam width has reduced from $w \approx 225\,\mu m$ for both temperatures at threshold to $w \approx 220\,\mu m$ and $w \approx 190\,\mu m$ at $T = 10\,°C$ and $T = 40\,°C$, respectively, at the maximum pump power. To further verify this, the laser beam width at the OC was imaged using a 4f-system. The measured results are indicated in Fig. 6.31(c) as solid points and show good agreement to the calculated values.

The impact of the temperature dependent lens is illustrated in Fig. 6.31(d) which shows the calculated laser beam width at the crystal. The key point here is relating the beam width at the crystal to the output power in Fig. 6.30. At $T = 40\,°C$, the greatest rate of increase in laser power occurs at around 14 W of absorbed pump power when the laser beam width at the crystal is $w \approx 235\,\mu m$. Further increase in absorbed pump power decreases the laser beam width to such an extent that the mode-matching efficiency reduces and so the power begins to roll-over. At $T = 10\,°C$, the greatest rate of increase in laser power occurs not at the same power but rather at the same lens power which is clear in Fig. 6.31(d) where $w \approx 235\,\mu m$ at around 16 W - matching to that in Fig. 6.30.

The cause of the temperature dependence of the pump-induced lens is not immediately clear. When considering the theoretical expression for the dioptric power of the pump induced lens (given by Eqs. (5.20) and (5.21) in Chapter 5) there are a number of temperature dependent terms, however the most dominant is the saturation power, P_s, due to the temperature dependence of the fluorescence lifetime (shown in Fig. 3.5 in Chapter 3). Its impact however, is to reduce the dioptric power at increased temperature. The output coupling dependence which can be significant is also not clear. While changing the output coupling impacts inversion and therefore the heating contribution from laser excited state absorption, analysing this impact is quite complex and requires a detailed investigation in its own right. Further work is therefore needed to fully understand the cause of the temperature and output coupling dependence of the pump-induced lens and with it even better performance can be expected by operating the cavity at elevated temperatures with optimal output coupling.

6.6 Summary

In this chapter record levels of output power has been demonstrated for a diode-pumped Alexandrite laser in TEM_{00} operation. It's worth noting that since the

publication of some of this work in [121], other high-power TEM_{00} Alexandrite lasers have been demonstrated. These include a 6.5 W system by Walochnik et al. which has a respectable optical efficiency of 26 % but a complex nine-mirror cavity and an output mode that was sensitive to the pump power [132]. More recently, Guan et al. demonstrated 5.5 W from a compact diode-pumped Alexandrite laser but at a reduced optical efficiency of around 16 % [133]. Therefore at the time of writing this work still stands as the highest powered TEM_{00} diode-pumped Alexandrite laser.

The results of this work can also be compared to other directly-diode-pumped infrared laser sources. Over the last decade there has also been development in red-diode-pumped Cr:LiSAF and Cr:LiCAF [85] and blue and green-diode-pumped Ti:Sapphire [134]. Diode-pumped Cr:LiSAF and Cr:LiCAF has so far been limited to the 1-1.5 W level in TEM_{00} operation with further power scaling limited by its poor thermo-mechanical properties [85].

Output powers up to 11 W in multimode operation have been achieved in diode-pumped Ti:Sapphire lasers, though this required a cryogenically cooled system [135]. In TEM_{00} mode, output power is still relatively low at around the 1 W-level, and while there is the commercial availability of high-power blue-laser-diodes, parasitic issues have hindered progress in power-scaling [88]. >1 W has recently been reported with green-diode-pumping by Miao et al. and with a respectable beam quality of $M^2 \sim 1.4$, though with a low optical efficiency of around 8 % [136].

Besides its superior performance compared to other direct-diode pumped vibronic lasers, its worth noting that the brightness levels achieved here are on-par with commercially available green-laser-pumped Ti:Sapphire lasers which provide 5 W of output power in TEM_{00} mode - though of course these laser typically operate in single-longitudinal-mode which will be explored in the following chapter.

It's worth noting other potential applications of this work. One such application, is in the growing interest in the eye-safe 2 µm region where Ti:Sapphire lasers are frequently used as high-brightness pump sources at around 780-800 nm for ultrafast Tm:doped bulk lasers [137, 138]. The diode-pumped Alexandrite laser shown here is capable of meeting such demands with better efficiency, compactness and power-scalability. The cavity design and modelling used in this chapter could also be applied to the power-scaling of blue-diode-pumped Pr-doped lasers operating in the visible region which has achieved significant attention over the last decade [48]. It is believed that the cavity design shown here could be used to achieve TEM_{00} output at the multi-watt level which has so far had limited success [139].

Chapter 7

Alexandrite Ring Lasers

Applications in the near-infrared such as quantum technologies utilising atomic transitions (e.g. Rb, K, Sr), vegetation lidar at the red-edge band and atmospheric remote sensing of the absorption lines of K, O_2 and H_2O require high-precision laser sources with TEM_{00} mode quality and narrow spectral linewidth.

Single-longitudinal-mode (SLM) operation is the best strategy for providing a narrow spectral linewidth. As outlined in Chapter 2, this can be achieved by use of an intra-cavity etalon, microchip cavity design or using a unidirectional ring resonator to eliminate spatial hole burning. In the case of Alexandrite the high insertion losses of an intra-cavity etalon has a significant impact on the overall efficiency, and a SLM microchip laser would require a cavity length of the order of $\sim 0.1\,\mathrm{mm}$. Unidirectional ring resonators with low-loss optical components therefore provide the most effective means of achieving SLM operation using Alexandrite.

Unidirectional laser operation is achieved using an optical diode which provides a preferential direction for the light propagation. A common method is to use a Faraday rotator (FR) in combination with a half-waveplate (HWP), as depicted in Fig. 7.1. Its operation can be described by considering the light propagation in the two directions (electric field shown in green and red). For the electric field propagating from left to right (shown in green), it is rotated an angle α by the FR. The HWP is positioned such that the electric field is then rotated again by an angle α so that the net polarisation rotation of the optical diode is zero. Light propagating from right to left (shown in red) is rotated by an angle α by the HWP and then again by an angle α but in the opposite direction to previously (anti-clockwise as opposed to clockwise) such that the net polarisation rotation of the

optical diode is 2α. This is because the FR is a non-reciprocal element. The FR is formed of a transparent medium, typically Terbium gallium garnet (TGG), inside a magnet such that the magnetic field lines (strength B) are along the beam direction. Linearly polarised light will experience a polarisation rotation of $\alpha = \pm VBl$ where V and l are the Verdet constant and length of the medium, respectively, and the sign accounts for the magnetic field line being along or opposed to the direction of propagation. Light propagation in one direction will therefore experience no change in polarisation rotation, whereas for light propagation in the opposite direction the rotation of 2α will lead to loss at a polarisation element such as a Brewster surface. For low-gain material such as Alexandrite a small rotation ($\alpha \sim 5°$) is sufficient for enabling unidirectional operation.

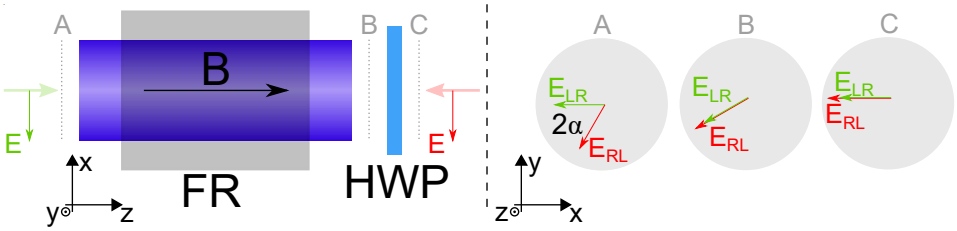

Figure 7.1: Optical diode formed of Faraday rotator (FR) and half-waveplate (HWP). Light moving from left to right is initially polarised along the x-axis (A) is then rotated by an angle α (B) and then rotated again by α back to the x-axis (C). Light moving from right to left is initially polarised along the x-axis (C) is then rotated by an angle α (B) and then rotated again by an angle α to a final angle of 2α to the x-axis. Image adapted from [37].

SLM Alexandrite lasers have been previously demonstrated, for example an injection-seeded Q-switched Alexandrite laser with a 40 MHz linewidth and over 40 mJ pulse energy intended for differential absorption lidar has been shown by Wulfmeyer et al. [61]. However, one of the major disadvantages of such systems was its flashlamp pump source, which despite its high energy, has low efficiency and more importantly requires regular service, often at remote locations. Recently, the development of diode-pumped Q-switched SLM Alexandrite lasers for resonance lidar systems (led by the Fraunhofer Institute for Laser Technology) has led to <10 MHz, mJ-level SLM systems [69, 140].

This chapter covers the very first demonstration of diode-pumped continuous-wave SLM Alexandrite lasers. Two SLM experimental systems are covered in this

chapter as well as two ring laser designs for further power scaling. Sections 7.1 and 7.2 cover Alexandrite ring lasers based on a "displaced mode" design where the laser mode size was minimised and offset to the focused pump waist for efficient mode matching at a displaced position. The output power of these systems was at the 1 W-level. The results of this work have been published in Optics Express [141] and in JOSA B [142]. Section 7.3 the power-scaled Alexandrite ring laser designs at the >1 W-level. One ring laser design has a negative intra-cavity lens to compensate the strong pump-induced lensing similar to the cavity design in Chapter 6, and the second looks at a simple and low-loss ring laser design without any intra-cavity lens achieving >5 W of output power with a beam quality of $M^2 = 1.1$.

7.1 Astigmatic Alexandrite Ring Laser

7.1.1 Cavity Model

This first diode-pumped Alexandrite ring laser was designed as a four-mirror bow-tie resonator which is the common design used in commercial single-longitudinal-mode (SLM) Ti:Sapphire lasers [143]. Figure 7.2 shows the cavity model which incorporates two curved mirrors of curvature R for mode size control, a Brewster-cut gain medium of physical length L_c and two plane mirrors, one being the output coupler (OC). The advantage of this design is that the two curved mirrors provide a small laser mode size for efficient matching to a tightly focused pump which is particularly useful for Ti:Sapphire's long absorption depth and high brightness pump source. Though the use of curved mirrors at an angle introduces astigmatism, it can be offset with the astigmatism of the Brewster-cut crystal [144].

The aim of this first demonstration was therefore to adapt the astigmatic bow-tie resonator for low-brightness diode-pumping. The limitation of the low-brightness pump ($M^2 \gtrsim 30$) is that the minimal waist size possible for achieving a suitable confocal parameter (~ 2 mm) is around $w_p \sim 75\,\mu$m. For an input pump beam radius of the order of 10 mm, a short focal length lens of $f_p \approx 50$ mm is required. Therefore, the radius of curvature of the curved mirrors has to be $R \leq 50$ mm to enable a small laser mode size ($w_l \approx 20\,\mu$m). Efficient mode-matching cannot occur at the position of the laser waist but instead at a displaced position where the laser mode size has expanded to match the pump size, as depicted in Fig. 7.3 which shows the location of the laser and pump waists.

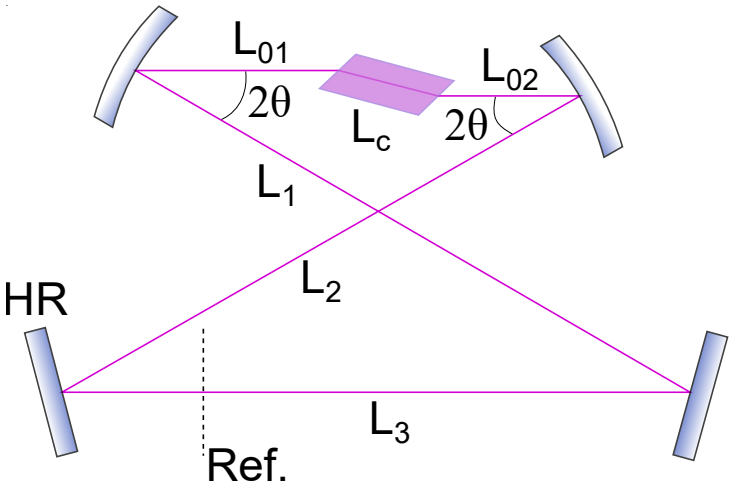

Figure 7.2: Astigmatic ring laser model in horizontal plane.

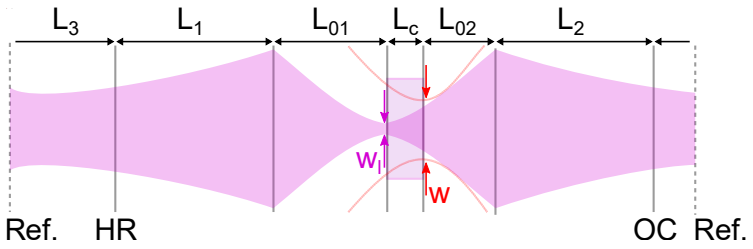

Figure 7.3: ABCD Gaussian propagation model of astigmatic ring laser cavity and "displaced mode" design.

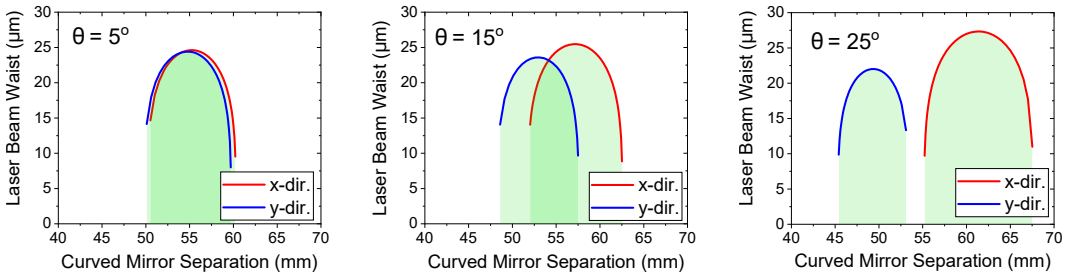

Figure 7.4: Laser beam waist size as a function of curved mirror separation at three angles. $R = 50\,\text{mm}$, $L_1 = L_2 = L_3 = 100\,\text{mm}$.

Another advantage of this cavity design is the insensitivity to the pump-induced lens since a very strong lens strength is required to overcome the focal power of the two curved mirrors, especially when $R \leq 50\,\text{mm}$. Therefore, for modelling the laser mode size (as shown in Fig. 7.3) the effect of pump-induced lensing has been neglected. The main goal was to determine the laser waist size as a function of the curved mirror separation. To account for the astigmatism, the calculations for the horizontal, as shown in Fig. 7.2, (x-direction) and vertical (y-direction) components need to be separated. The effective mirror radius of curvature and optical crystal length in each component are adapted to [144]

$$R' = \begin{cases} R/\cos\theta, & \text{x-direction} \\ R\cos\theta, & \text{y-direction} \end{cases}$$

$$L_c' = \begin{cases} L_c/n^3, & \text{x-direction} \\ L_c/n, & \text{y-direction.} \end{cases}$$

Figure 7.4 shows the laser beam waist size as a function of the curved mirror separation ($L_{01} + L_c + L_{02}$) with $R = 50\,\text{mm}$ and $L_1 = L_2 = L_3 = 100\,\text{mm}$. Three angles are shown: $\theta = 5$, 15 and 25°. Near normal incidence the stability region of the x and y directions are well overlapped, though the mode size throughout the rest of the cavity is not necessarily equal. The cavity is stable at a curved mirror separation of around 50-60 mm with a waist size of $w_l \approx 20\,\mu\text{m}$. Increasing the angle to $\theta = 15°$ reduces the region of cavity stability (shown in darker green) to a curved mirror separation of around 52.5-57.5 mm with a similar waist size. At larger angles the stability region in the x-direction and y-direction are no longer overlapping meaning that the cavity is no longer stable. Variation in L_1, L_2 and L_3 from 50 mm to 200 mm was also investigated, with little impact on the laser waist size to be found.

For the bow-tie ring cavity with two curved mirrors of equal curvature the condition for astigmatism compensation is given by [144]

$$R\sin\theta\tan\theta = L_c\left(\frac{n^2-1}{n^3}\right). \tag{7.1}$$

where n is the refractive index of the gain medium, or in the case of Alexandrite $n = n_b$. Typically R and L_c are chosen according to the desired cavity geometry, therefore it is more convenient to have an expression for the angle of incidence

required to provide astigmatic compensation. Rearranging Eq. (7.1) and solving the quadratic equation for the positive root gives

$$\theta = \cos^{-1}\left[\frac{1}{2}\left(\sqrt{\left(\frac{L_c n'}{R}\right)^2 + 4} - \frac{L_c n'}{R}\right)\right]. \tag{7.2}$$

where $n' = (n^2 - 1)/n^3$. Once the angle is evaluated then the appropriate curved mirror separation can be chosen and then the values of L_{01} and L_{02} can be selected to provide the "displaced mode" overlap at the crystal surface.

7.1.2 Experimental Setup

The pump source used for this experiment was a water-cooled 7-bar diode-stack chosen so as to provide sufficient power in a single-end-pumped geometry. Each of the diode bars consist of 20 emitters with slow and fast axis collimation which are then stacked together internally to produce an output beam with a dimension of around 5×5 mm with the bars separated by around 0.8 mm and at a horizontal tilt angle of around 3.5°. The linear polarisation is at an angle of around 9° to the vertical. The beam and polarisation tilt were corrected using a pair of 45° mirrors and a 4° wedge. At a drive current of 14 A the laser wavelength and linewidth were 639 nm and 1.5 nm, respectively.

Figure 7.5 shows the output power of the diode-stack as a function of the drive current at a water temperature of 16 °C. At a drive current of 14 A, the maximum pump power is 64.1 W. The beam quality was measured using a 100 mm focal length lens and found to be $M_x^2 = 250$ and $M_y^2 = 30$ in the horizontal and vertical directions, respectively. This highly multimode and astigmatic property of the pump, as shown in the beam caustic in the inset of Fig. 7.5, imposes major limitations on the end-pumping capability of the diode-stack. Therefore, to improve the beam quality (to enable intense pumping with a sufficiently long confocal parameter) a beam filtering technique was used.

A pair of highly reflective mirrors arranged as a slit aperture (in the horizontal direction) was used to filter the beam. The transmitted portion of the beam was used for end-pumping and the reflected portion was dumped. Two aperture sizes (mirror separation distance) were investigated, 1.5 mm and 2.5 mm. Figure 7.6 shows the beam profile of the diode-stack with the aperture size at 1.5 mm. Figures 7.6(a) and 7.6(b) shows the focus in the horizontal and vertical direction, respectively, when

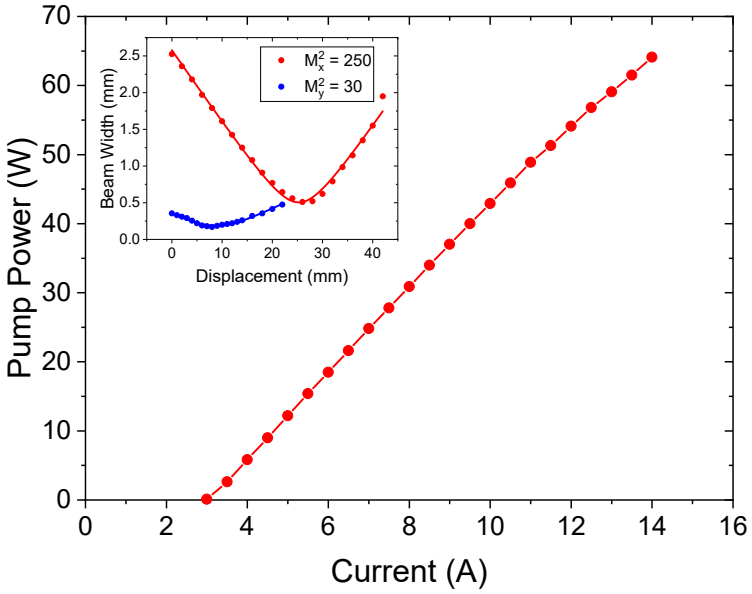

Figure 7.5: Output power as a function of drive current for the 7-bar diode stack. Inset shows beam caustic.

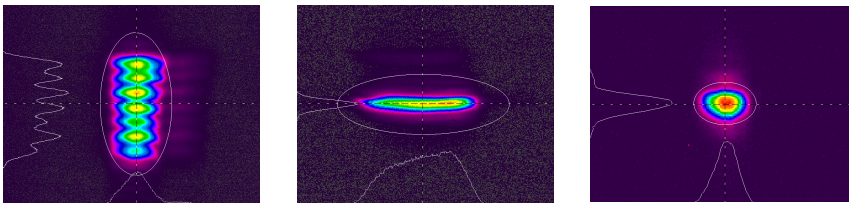

(a) (b) (c)

Figure 7.6: Spatially filtered 7-bar diode stack focus: (a) in horizontal through spherical lens; (b) in vertical through spherical lens; (c) in vertical and horizontal through cylindrical lenses.

focusing with a spherical lens. The mirror slit therefore enables tighter focusing in the horizontal direction but with the astigmatism still present, though this can be easily overcome using cylindrical lenses, as demonstrated in Fig. 7.6(c).

Figure 7.7 shows the output power as a function of the drive current with the slit aperture at 2.5 mm. The maximum transmitted power was 10.8 W at a drive current of 14 A. The beam quality of the transmitted beam was measured to be $M_x^2 = 45$ and $M_y^2 = 25$. A significant improvement in the horizontal beam quality was obtained using the two-mirror aperture, and so making a waist of $w_p \sim 75\,\mu$m and a confocal parameter of $2z_R \sim 2$ mm achievable. Though this was at the expense

of the majority of the available pump power a transmitted power of >10 W was believed to be sufficient for >1 W laser operation.

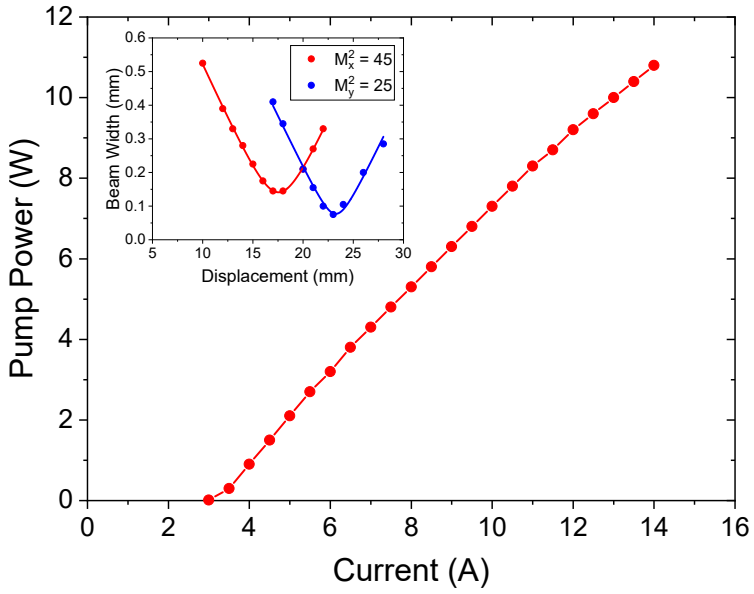

Figure 7.7: Output power as a function of drive current for the filtered 7-bar diode stack with the aperture at 2.5 mm. Inset shows beam caustic.

Figure 7.8 shows the experimental Alexandrite ring cavity configuration. The four-mirror bow-tie resonator was formed of two curved mirrors of concave curvature $R = 50$ mm. The mirrors are highly transmissive (HT) at the pump wavelength and highly reflective (HR) at the laser wavelength. The pump was directed through one of these mirrors - note that these mirrors are concave-convex so as to prevent any defocusing and astigmatism of the transmitted pump. The other two mirrors were plane mirrors, one was HR at the laser wavelength and the second was the output coupler (OC) with a reflectivity of $R_{\mathrm{OC}} = 99.0\,\%$ at the laser wavelength. The Alexandrite laser crystal was a Brewster-cut rod (similar to that used in Chapter 4) of length $L_c = 8$ mm and a diameter of 4 mm. It had a Chromium doping 0.22 at.%. The crystal was mounted in a water-cooled copper heat sink with the temperature of the water maintained at 40 °C.

For astigmatism compensation the curved mirrors were placed at an angle of $\theta = 14^\circ$ as calculated by Eq. (7.2). The cavity dimensions (as indicated in Fig. 7.2) were $L_{01} = 35$ mm, $L_{02} = 20$ mm and $L_1 = L_2 = L_3 = 105$ mm which gave a laser

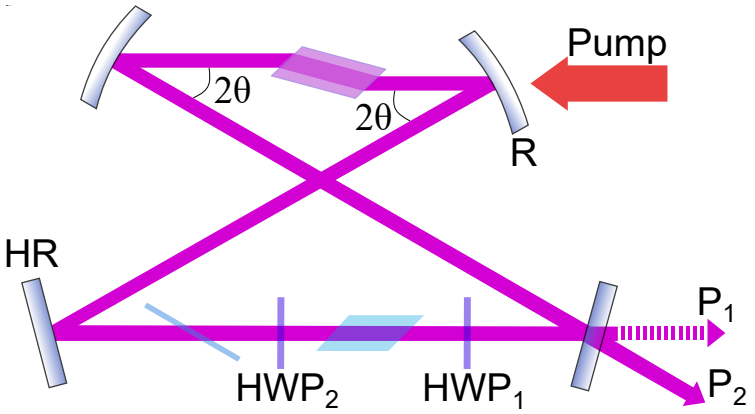

Figure 7.8: Astigmatic ring laser setup.

waist size of $w_l \approx 20\,\mu m$, a total cavity length of $\sim 380\,mm$ and a compact footprint of around $140 \times 90\,mm$.

Unidirectional operation was provided with the combination of the Brewster-cut TGG Faraday rotator (FR) and half-waveplate (HWP_1). A 0.5 mm thick intracavity quartz birefringent filter (BiFi) was later included at Brewster's angle for wavelength tuning as well as a second half-waveplate (HWP_2). The reason for the addition of HWP_2 will be discussed in Section 7.1.3.

Pumping was provided with the mirror aperture size at 2.5 mm so as to provide a total incident pump power of 10.8 W. A pair of horizontal cylindrical lenses were used to collimate the horizontal component of the pump beam and then an aspheric lens of focal length $f_p = 50\,mm$ was used to focus the pump beam to a waist size of around $w_{p_x} = 70\,\mu m$, $w_{p_y} = 65\,\mu m$.

7.1.3 Results

The initial cavity was arranged without the BiFi and HWP_2. Figure 7.9 shows the laser power (P_2) as a function of the incident pump power - note that due to the high polarisation purity of the pump, the Brewster surface and the confocal parameter, the incident pump power is likely to be approximately equal to the absorbed pump power. 1.05 W of laser power was obtained at an incident pump power of 10.8 W. This corresponds to an optical-to-optical conversion efficiency of 9.7 % and a slope efficiency (by linear fit) of 11 %. The irregular behaviour of the power curve is attributed to the variation in the astigmatic thermal lens changing the mode overlap. It is worth noting that the laser mode appeared elliptical and

was possibly higher order at some pump powers.

The beam quality was measured to be $M_x^2 = 1.12$ and $M_y^2 = 1.16$ verifying TEM_{00} output. The astigmatic compensation of the curved mirrors at an angle of $\theta = 14^\circ$ was reasonably successful, as indicated by the beam caustic in Fig. 7.10(a).

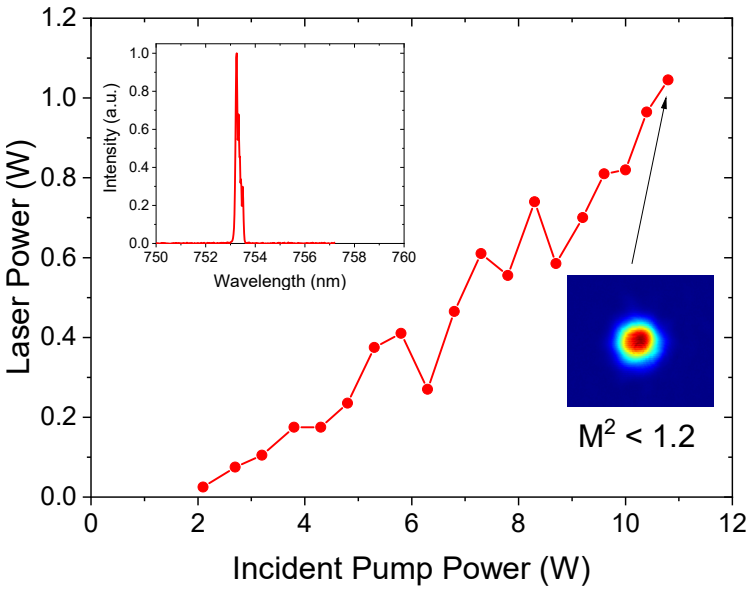

Figure 7.9: Laser power as a function of incident pump power for the astigmatic unidirectional ring laser.

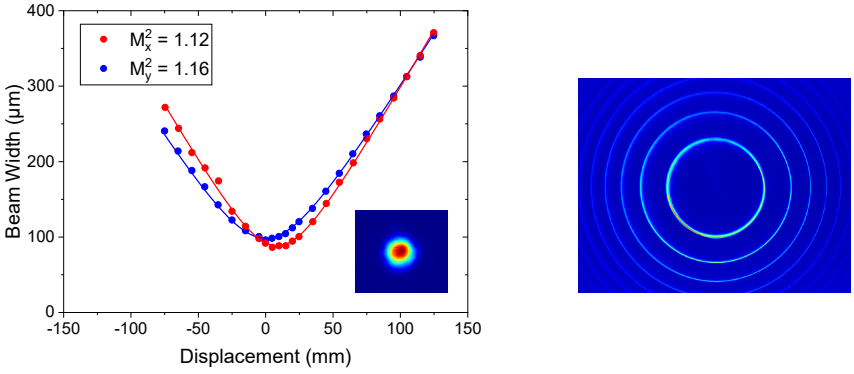

(a) (b)

Figure 7.10: (a) Laser beam caustic at 1.05 W. (b) FP interference pattern showing SLM operation.

The laser wavelength was measured to be 753.3 nm using a spectrometer with

the measured linewidth limited by the resolution of the spectrometer. A FP etalon (FSR = 6.9 GHz, Finesse = 50) was used to discern the number of longitudinal modes lasing. Figure 7.10(b) shows the interference pattern demonstrating SLM operation (see Appendix A). Due to the lack of wavelength stabilisation the wavelength would fluctuate slightly and occasionally two longitudinal modes were observed. This could be improved by using a piezoelectric control of the cavity length.

Wavelength tuning was investigated with the use of an intra-cavity birefringent filter (BiFi), as depicted in Fig. 7.8. Figure 7.11 shows the laser power as a function of the wavelength when tuning the BiFi (shown in red) at a maximum pump power of 10.8 W. Wavelength tuning at 727-792 nm was obtained with peaks at 728, 739, 751, 763 and 777 nm. This periodic modulation of around 12 nm is due to the wavelength filtering effect of the Brewster-cut Alexandrite crystal. As described in Chapter 4, the Brewster-cut Alexandrite laser crystal inside a laser resonator will act as a birefringent filter with a free-spectral range of $\Delta\lambda_{\mathrm{FSR}} = \lambda^2/\Delta nL \approx 12\,\mathrm{nm}$ for the 8 mm long crystal. Therefore at intervals of around 12 nm the transmission peaks of the crystal and BiFi are well matched providing high transmission, but elsewhere there is some loss.

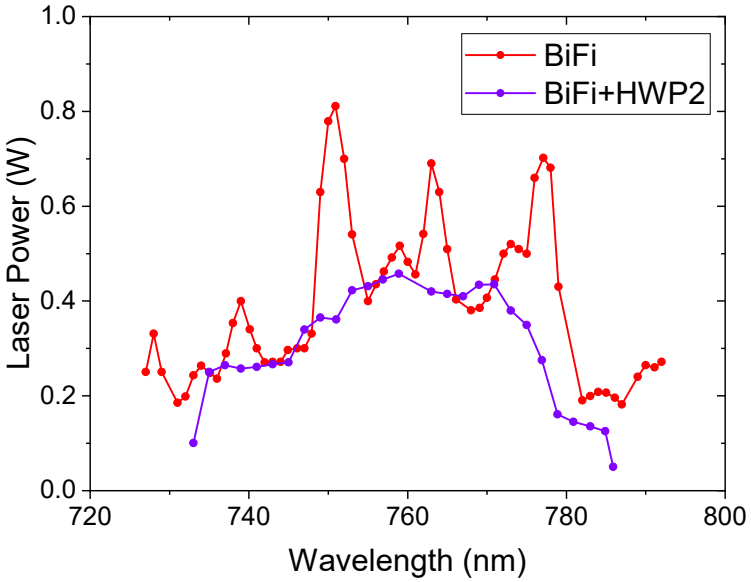

Figure 7.11: Laser power as a function of wavelength using BiFi (shown in red) and using BiFi with HWP_2 (shown in purple).

One method for "smoothing out" this effect was to introduce a secondary half-

waveplate (HWP_2) which acts to optimise the polarisation between the BiFi and the crystal. The laser power as a function of wavelength using the BiFi and HWP_2 combination is also shown in Fig. 7.11. This provided a much smoother tuning curve with stable output power, where previously wavelengths just off the peaks were not stable. However, this was at the expense of reduced power and a narrower tuning range. The modulation in wavelength tuning observed when just using the BiFi was much stronger than that observed for other Brewster-cut crystals and so it is likely that the modulation was enhanced by a mismatch between the crystal axes and the Brewster-cut. This was later verified when it was found that the angle of incidence for maximum absorption (beam travelling along c-axis) was slightly different to the angle of incidence for minimal reflection loss (Brewster's angle). Smoother tuning using the BiFi is therefore expected with a better cut crystal.

7.2 Non-astigmatic Alexandrite Ring Laser

7.2.1 Cavity Model

A simpler non-astigmatic cavity design was also considered with the aim of having a better model that included the effects of pump-induced lensing and therefore to remove the variation of the beam quality at different pump powers.

Figure 7.12 shows the cavity design for the non-astigmatic ring laser. The cavity design was similar to that of the astigmatic ring laser - a four mirror ring laser with a small laser waist size located near the gain medium and displaced to the pump waist. The cavity was designed in a rectangular geometry with two intracavity lenses of focal length $f_l = 100\,\text{mm}$ placed in the two long arms. The lenses were anti-reflection (AR) coated (<0.1 % loss) at the laser wavelength. Mirrors M1, M2 and M3 were HT at the pump wavelength and HR at the laser wavelength, and the OC had a reflectivity of R_{OC} (at 45°) at the laser wavelength.

For efficient TEM_{00} operation there were a number of factors of the cavity design to consider. The first task was to investigate the lens separation ($L_1 + L_c + L_2$) required for cavity stability. To simplify the analysis the footprint of the non-astigmatic ring laser was fixed to $L_y = 150\,\text{mm}$ and $L_x = 60\,\text{mm}$, this provided a compact setup with sufficient space for the mounted cavity optics (including the optical diode which was included later). Cavity stability and mode size analysis was performed using the ABCD Gaussian propagation formalism, as shown in Fig. 7.13.

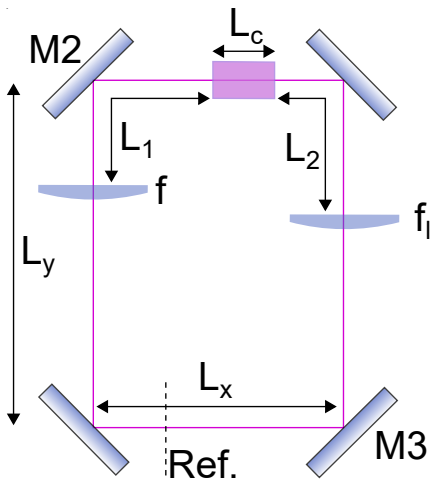

Figure 7.12: Non-astigmatic ring laser setup.

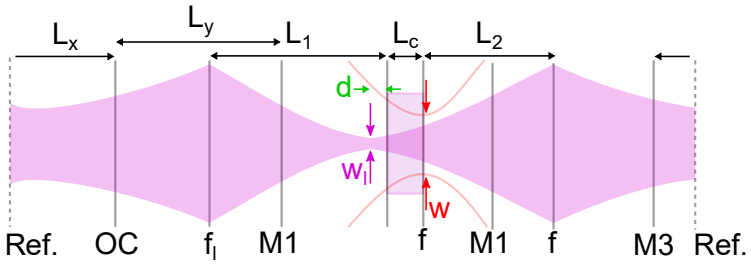

Figure 7.13: ABCD Gaussian propagation model of non-astigmatic ring laser cavity and "displaced mode" design.

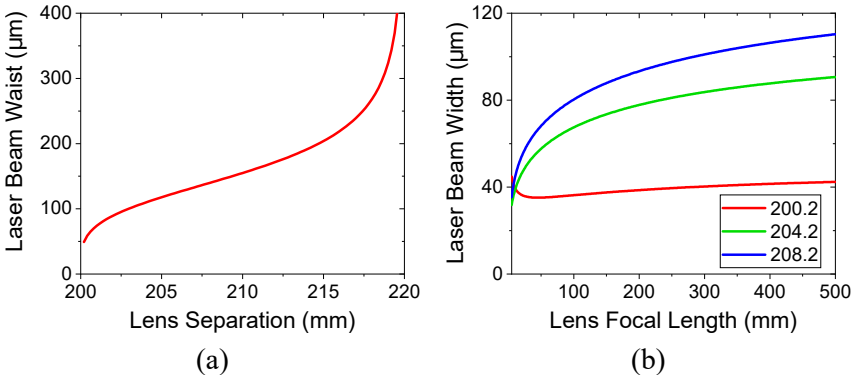

Figure 7.14: (a) Laser beam waist as a function of lens separation $L_1 + L_2 + L_c$. (b) Laser beam width at midpoint between M1 and M2 as a function of pump-induced lens focal length for three lens separation lengths.

Figure 7.14(a) shows the laser waist size as a function of the lens separation without accounting for the effects of the pump induced lensing. The cavity is only stable when the separation is around 200-220 mm with the waist symmetrically positioned between the two lenses. The impact of the pump-induced lens was analysed by calculating the laser beam width at the midpoint between M1 and M2. Figure 7.14(b) shows the laser beam width as a function of the pump-induced lens focal length for three lens separation distances. Though the change in the laser beam width varies for each lens separation, the cavity is able to tolerate strong lensing with relatively insignificant change in the laser beam width even down to a pump-induced lens focal length of 50 mm which is the estimated focal length at the maximum pump power.

The final aspect to consider were L_1 and L_2. The cavity was designed with a displaced mode, as discussed in the previous section and shown in Fig. 7.13, where the laser waist size was offset to the pump waist size. Since the reduction in the beam width was negligible, especially for a small waist size (<50 µm), the only consideration was the location of the waist relative to the crystal denoted d in Fig. 7.13. This was computed numerically and it was found that d had to be increased with increasing pump power which was achieved by increasing L_2 and also L_1 since the total lensing on the right side of the cavity is a combination of the pump-induced lensing and f_l. The value of d was calculated to be around 0 mm at threshold and 1.4 mm at the maximum pump power.

7.2.2 Experimental Setup

Figure 7.15 shows the experimental setup of the non-astigmatic Alexandrite ring laser. Pumping was provided with the same beam-filtered 7-bar diode stack as was used with the astigmatic ring laser. The setup was almost identical using the same 2.5 mm aperture and pump optics that provided a waist size of around $w_{p_x} = 70\,\mu\text{m}$, $w_{p_y} = 65\,\mu\text{m}$. The pump was focused through M1 in a single-end-pumped configuration with a maximum incident pump power of 10.8 W.

The cavity dimension were $L_y = 150$ mm and $L_x = 60$ mm giving a total cavity length of around 420 mm, and $L_1 = 100$ mm and $L_2 = 95$ mm. The Alexandrite crystal was a c-cut rod of length 10 mm, diameter of 4 mm, a Chromium-doping of 0.22 at.% and with AR coated at the laser wavelength. The crystal was mounted in a water-cooled copper heat sink at 16 °C. The OC had a reflectivity of $R_{\text{OC}} = 99.2\,\%$ at the laser wavelength. The same FR and HWP were used as in the astigmatic ring laser for unidirectional control. A 1 mm thick BiFi was used for wavelength tuning.

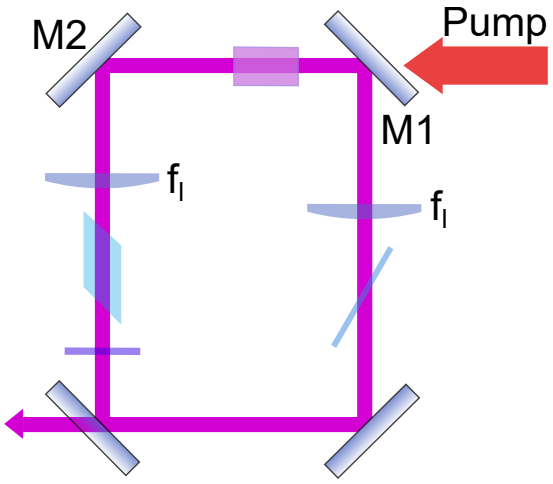

Figure 7.15: Non-astigmatic ring laser experimental setup.

7.2.3 Results

Figure 7.16 shows the laser power as a function of the incident pump power for the unidirectional ring laser without the BiFi. A maximum output power of 0.7 W was obtained at an incident pump power of 10.8 W with a near-diffraction limited beam quality of $M_x^2 = 1.07$, $M_x^2 = 1.06$. The slope efficiency was 13 %. The laser operated at a wavelength of 754.6 nm, as shown in the inset of Fig. 7.16. The longitudinal operation of the laser was again investigated with the FP etalon (FSR = 6.9 GHz and Finesse = 50) and found to operate in SLM.

Compared to the astigmatic ring laser the laser beam quality here has improved both at the maximum pump power and in maintaining TEM_{00} mode quality over the entire pump power range. It is worth noting that unlike previously the absorbed pump power is not approximately equal to the incident pump power as the crystal was not AR coated at the pump wavelength - the transmission was around 94 %. Threshold is therefore at an absorbed pump power of around 4.9 W. This increase (compared to around 2 W for the astigmatic ring laser) is likely due to the additional losses from the intracavity lenses.

With the BiFi included wavelength tuning was investigated. Figure 7.17 shows the laser power as a function of the wavelength with continuous tuning of 748-773 nm obtained. Wavelength tuning was limited by the sharp decrease in OC reflectivity which fell below 99 % at 780 nm.

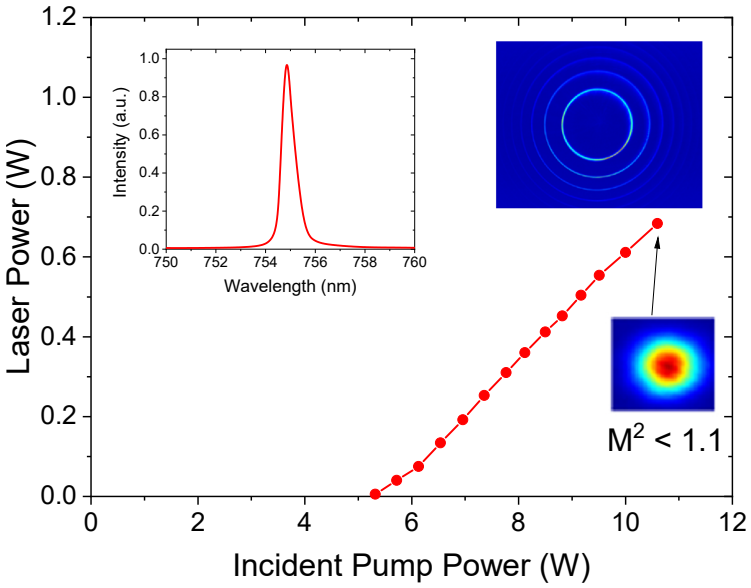

Figure 7.16: Laser power as a function of incident pump power for the non-astigmatic unidirectional ring laser.

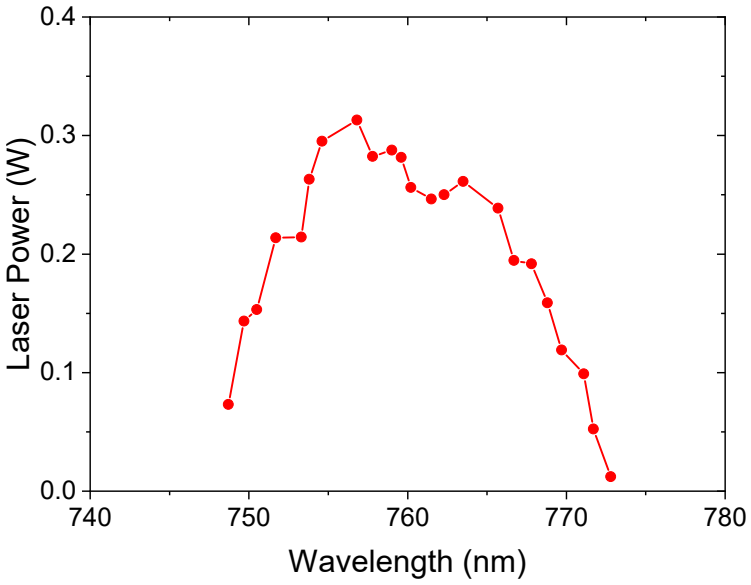

Figure 7.17: Laser power as a function of wavelength using BiFi.

7.3 Power Scaled Alexandrite Ring Lasers

Power scaling diode-pumped Alexandrite ring laser systems to >1 W with wavelength tuning imposes a number of challenges. The main challenge is dealing with the strong pump-induced lensing which at 10 W of absorbed pump power is $\sim 20\,\mathrm{m}^{-1}$ (50 mm) when $w_p = 70\,\mu\mathrm{m}$. Further increase in pumping would then push both the astigmatic and non-astigmatic cavity designs toward instability. A straightforward solution would be to increase the waist size and so alleviate the pump-induced lens strength, however this would require further optimisation in the mode-matching due to the "displaced mode" design.

For significant power scaling, alternative designs must therefore be considered. In this section two bidirectional Alexandrite laser cavities are investigated as potential platforms for multi-watt SLM Alexandrite lasers. The results of Chapter 6 showed that multi-watt-level tunable operation from Alexandrite lasers can be achieved using larger pump waist sizes ($w_p > 150\,\mu\mathrm{m}$) in combination with using a convex-curved mirror for compensating the pump-induced lensing and efficient mode-matching at the gain medium for TEM_{00} operation. Therefore, for the first power-scaled ring laser the aim was to use an intra-cavity negative lens in a four-mirror non-astigmatic ring laser.

The second design has no intra-cavity lenses for mode size control, relying solely on the cavity length for efficient mode matching and an increased pump waist size to alleviate any strong pump-induced lensing. The benefit of this setup is the reduced loss from intra-cavity components and the reduced threshold compared to using an intra-cavity negative lens.

7.3.1 Alexandrite Ring Laser with Negative Lens

Figure 7.18 shows the setup for the Alexandrite ring laser with an intra-cavity negative lens. A non-astigmatic design was chosen for simpler modelling, ease of alignment and for better spacing for intra-cavity optical elements in a compact-setup. In this preliminary cavity design a four-mirror rectangular cavity (dimensions $L_x \times L_y$) was used with two dichroic mirrors (DM) that are HT at the pump wavelength and HR at the laser wavelength, one mirror that is HR at the laser wavelength and an OC with partial reflectivity at the laser wavelength. A single intra-cavity negative lens of focal length f_- was placed in the left arm for laser mode size control at a distance L_f from the left side of the crystal.

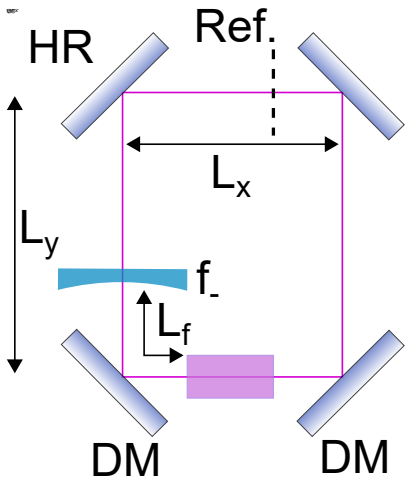

Figure 7.18: Power-scaled ring laser with negative lens setup.

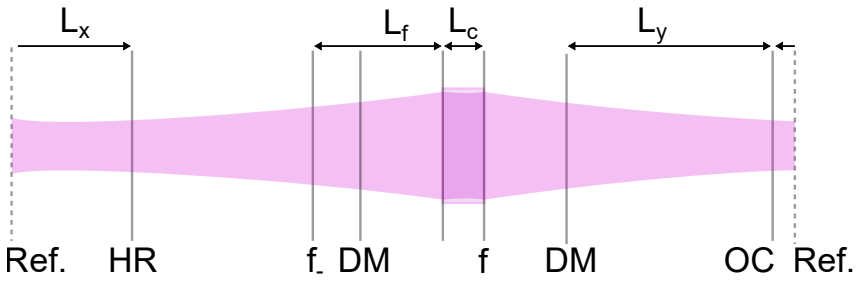

Figure 7.19: ABCD Gaussian propagation model of Alexandrite ring laser with intra-cavity negative lens for power-scaled operation.

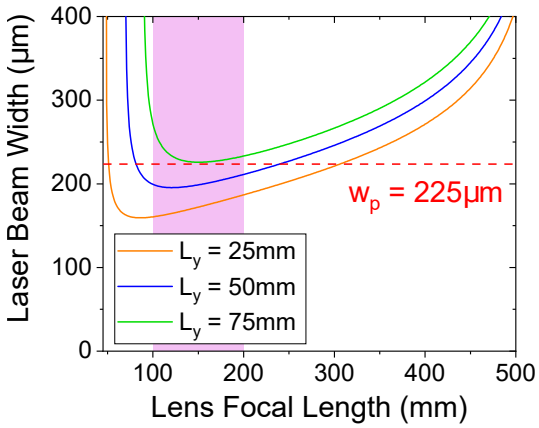

Figure 7.20: Laser beam width as a function of pump-induced lens focal length for $L_y = 25$, 50 and 75 mm. Shaded region indicates theoretical pump-induced lens range.

Mode size analysis was again performed using a numerical ABCD Gaussian propagation model, as shown schematically in Fig. 7.19. The aim of the modelling was to evaluate the laser beam width at the crystal as a function of the pump-induced lens focal length, f, under different cavity geometries. As per previous analysis this was greatly simplified by fixing all but one of the parameters. In this model, the intra-cavity lens focal length $f_{-} = -250\,\text{mm}$ and $L_x = 25\,\text{mm}$ were both fixed. The lens focal length was chosen as it was of comparable strength to the curved mirrors used in Chapter 6 and the choice of L_x was based on the minimum distance possible to fit the optical mounts of the DMs and crystal and so maximise the variation in L_y. $L_f = 30\,\text{mm}$ was also fixed for simplicity to be at the closest possible position to the crystal.

Figure 7.20 shows the laser beam width at the crystal as a function of the pump-induced lens focal length with $L_y = 25$, 50 and 75 mm. The cavity is stable at $f \approx 500\,\text{mm}$ as this is when the combined focal power of the pump-induced lens is strong enough to overcome the focal power of the intra-cavity negative lens. Increased mode sizes are obtained for longer cavities and wider stability ranges for shorter cavities.

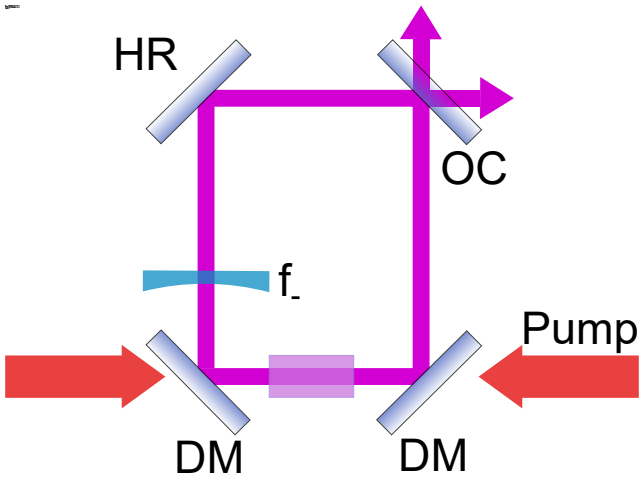

Figure 7.21: Power-scaled ring laser with negative lens experimental setup.

Figure 7.21 shows the experimental setup for the power scaled Alexandrite ring laser. For this ring laser the dual-end-pump scheme with the 200 µm fibre-coupled pump source, as shown in Chapter 6, was used. The pump waist size was $w_p = 225\,\mu\text{m}$ using an aspheric lenses of focal length $f_p = 79\,\text{mm}$. The theoretical pump-

induced lens for this pump size varies from around 200 mm to 100 mm at around 23 W to 33 W of total absorbed pump power, as indicated by the shaded region in Fig. 7.20. An arm-length of $L_y = 25 - 50$ mm is therefore a suitable range to examine as it provides good matching between the pump and laser modes and shouldn't go toward instability unless operated at the highest power. The OC had a reflectivity of $R_{\mathrm{OC}} = 98.0\,\%$ at normal incidence and a measured reflectivity of around 97 % at 45°. The Alexandrite crystal was the same as that used in Chapter 6 - a 4×4 mm aperture, 6 mm long c-cut slab with 0.2 at.% Chromium-doping and AR coatings at both the laser and pump wavelengths.

Figures 7.22 and 7.23 show the total laser power as a function of the absorbed pump power for $L_y = 50$ mm and $L_y = 25$ mm, respectively. In both cases the temperature of the crystal was initially set to $T = 20\,^{\circ}\mathrm{C}$. For $L_y = 50$ mm, 3.5 W of laser power was obtained at 24.5 W absorbed pump power with a beam quality of $M^2 = 1.1$ in both directions. Threshold was at an absorbed pump power of $P_{th} = 15.5$ W. The spectrum was relatively narrow (compared to the linear cavities in Chapter 6) even without spectral or unidirectional control. A slightly higher power of 3.6 W was obtained at 24.5 W absorbed pump power when the temperature of the crystal was lowered to $T = 12\,^{\circ}\mathrm{C}$. At both temperatures further increase in pump power led to a roll-over in laser power.

For $L_y = 25$ mm further increases in laser power was possible with 4.0 W obtained at 27.1 W absorbed pump power. The mode quality here was also diffraction limited with $M^2 = 1.1$. By comparing the two results to the theoretical model, the roll-over in laser power can be attributed to strong pump-induced lensing rather than an under-filled mode-match since improved performance was obtained by decreasing the cavity length which improves the stability range but reduces the mode size at the gain medium, as shown in Fig. 7.20. This was further proved to be the case when it was found that no lasing could be obtained with $L_y = 75$ mm.

These results show that multi-watt TEM_{00} operation from an Alexandrite ring laser can be achieved using an intra-cavity negative lens for mode size control and shows potential for multi-watt SLM operation. The disadvantage of this system is the high threshold and the relatively low optical efficiency of 15 %. Though the threshold could be lowered using a weaker intra-cavity lens it would then be less able to compensate strong thermal lensing which was the main issue in this cavity, further optimisation in cavity design is therefore required for realising improved optical efficiency and >5 W laser operation.

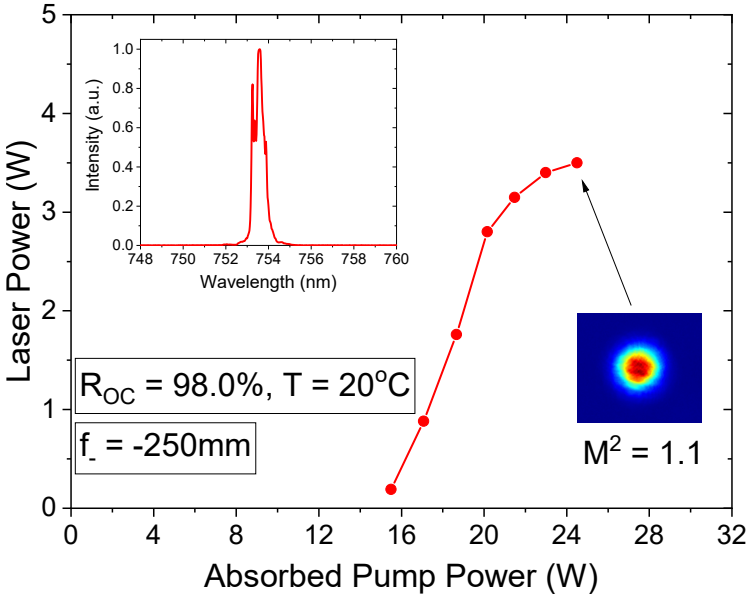

Figure 7.22: Laser power as a function of the absorbed pump power for the power scaled Alexandrite ring laser with intra-cavity lens $f_- = -250\,\mathrm{mm}$, $L_x = 25\,\mathrm{mm}$ and $L_y = 50\,\mathrm{mm}$.

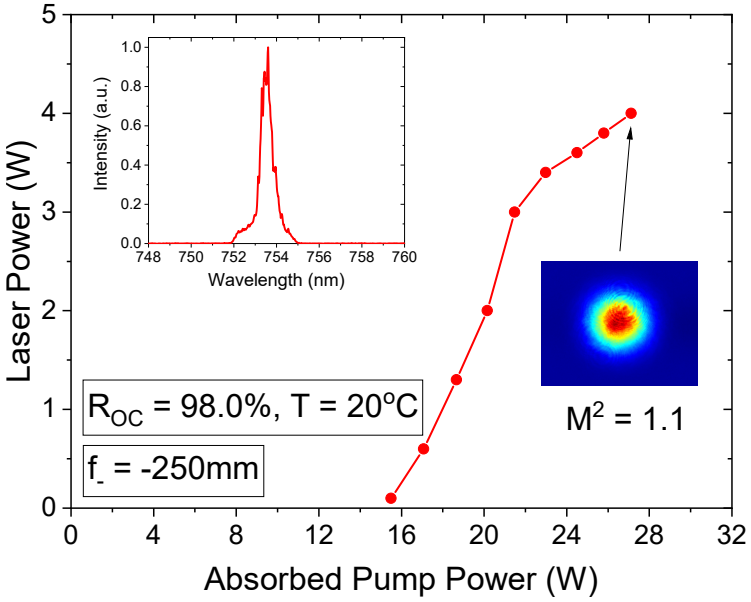

Figure 7.23: Laser power as a function of the absorbed pump power for the power scaled Alexandrite ring laser with intra-cavity lens $f_- = -250\,\mathrm{mm}$, $L_x = 25\,\mathrm{mm}$ and $L_y = 25\,\mathrm{mm}$.

7.3.2 Alexandrite Ring Laser with no Lens

An alternative design to consider is a simple four-mirror cavity without any intra-cavity lenses. Though the lack of direct mode size control will hinder TEM_{00} at the highest pump power, as demonstrated in Section 6.2, >1 W TEM_{00} output should be achievable at mid-range pump powers in a system with lower losses and a significantly lower threshold compared to that shown in the previous section.

Figure 7.24 shows the experimental setup for the compact Alexandrite ring laser. The four mirror cavity is formed of the same four plane mirrors as was used in the previous system but arranged with $L_x = 35\,\text{mm}$ and $L_y = 25\,\text{mm}$. While a more compact setup could be achieved this setup provides better mode-matching at higher pump-power at the expense of a slightly higher threshold. The same pump setup and waist size of $w_p = 225\,\mu\text{m}$ was used.

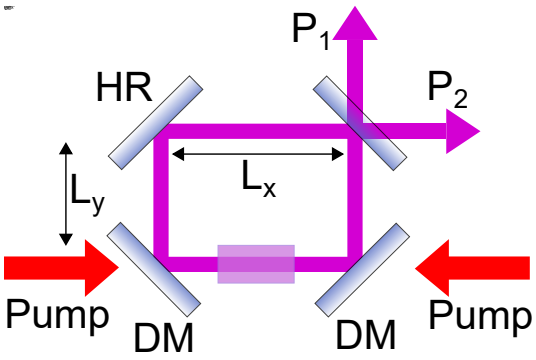

Figure 7.24: Alexandrite ring laser with no intra-cavity lens experimental setup.

The total output laser power ($P_1 + P_2$) as a function of the absorbed pump power is shown in Fig. 7.25. At an absorbed pump power of 21.5 W the laser power was 5.1 W and the mode quality was $M_x^2 = 1.07$, $M_y^2 = 1.08$. At higher pump power the mode quality slightly degraded to $M_x^2 = 1.85$, $M_y^2 = 1.60$ with a laser power of 7.4 W at an absorbed pump power of 27.1 W. This result demonstrates that the simple compact cavity performs well at mid-level pump powers with good optical and slope efficiencies of 24 % and 35 %, respectively.

Extending the cavity design to SLM operation using a Faraday rotator and half-waveplate requires careful design of the optical mounts to fit both components without having to increase the cavity length. Increasing the cavity length of Alexandrite lasers without any intra-cavity lenses or curved mirrors leads to an increase in

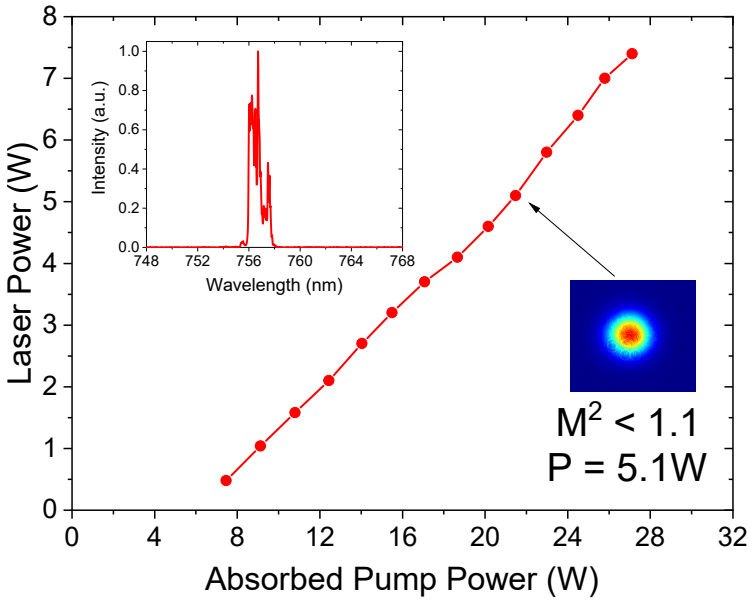

Figure 7.25: Laser power (total of both outputs) as a function of absorbed pump power for the compact Alexandrite ring laser.

threshold and reduction in overall efficiency due to the increased alignment precision [119]. Due to the compact nature of this design, proper mounting and fitting of the intra-cavity unidirectional components could not be achieved at the time but can be explored in future. This design shows potential for multi-watt level SLM operation with enhanced efficiency and overall simplicity compared to the previous designs.

7.4 Summary

In this chapter two single-longitudinal-mode (SLM) Alexandrite ring lasers have been demonstrated. The first system was based on the traditional bow-tie ring laser geometry using an optical diode for unidirectional control to eliminate spatial hole-burning and adapted for mutli-mode diode pumping using a novel "displaced-mode" design. >1 W of laser power was obtained with TEM_{00} and SLM output with an optical efficiency of 10 %. SLM operation at 727-792 nm was obtained using a birefringent filter (BiFi). This result was the first ever demonstration of a diode-pumped continuous-wave SLM Alexandrite laser.

For the second system, the cavity design was replicated but using intra-cavity lenses instead of curved mirrors in a non-astigmatic ring laser. Up to 0.7 W of

laser power was obtained in SLM and TEM_{00} operation. This was maintained at all pump powers, and so demonstrating the improved control of the pump-induced lensing provided by the non-astigmatic design. A wavelength tuning range of 748-773 nm was obtained using a BiFi.

Two alternative bidirectional ring laser designs were also investigated to explore power-scaling capabilities. The first design was a four-mirror non-astigmatic laser with an intra-cavity negative lens to offset the pump-induced lensing under fibre-coupled dual-end-pumping. With this design a significant improvement in output power was obtained with 4 W in TEM_{00} mode demonstrated with an optical efficiency of 15 %.

For improved optical efficiency, the second bidirectional ring laser design had no intra-cavity lens. This simple and low-loss design provided an improvement in output power and efficiency. A maximum TEM_{00} output power of 5.1 W was obtained with an optical efficiency of 24 % and a slope efficiency of 35 %.

These results show a promising outlook for multi-watt SLM Alexandrite with >1 W achievable over a broad wavelength range in the near-infrared capable of matching several atomic transitions. Power scaling also realises the potential to address high-precision applications in the ultra-violet at around 360-400 nm via second-harmonic-generation.

Chapter 8

Thesis Summary

The aim of this work was to develop power-scaled tunable Alexandrite lasers by improving the understanding of the properties of and pump-induced lensing effects in diode-pumped Alexandrite lasers. The modelling and optimising of tunable Alexandrite lasers at the multi-watt level was demonstrated as well as single-longitudinal-mode lasers for high precision applications including remote sensing and quantum technologies.

Before power-scaling, a novel wavelength tuning method was investigated using a Brewster-cut Alexandrite crystal in a plane-plane resonator. Continuous wavelength tuning and dual wavelength operation was obtained by tilting the Alexandrite crystal in a simple and compact system without any other wavelength selective element. This laser achieved a maximum continuous tuning range of 747-768 nm with a 15 GHz linewidth and TEM_{00} output mode quality. Wavelength tuning was limited by the FSR of the crystal, though this also enabled stable dual wavelength operation. A theoretical model for the laser wavelength and tuning range was devised and shown to match well with the experimental results. This work enhanced the understanding of the birefringent properties of Alexandrite.

Pump-induced lensing effects were investigated in detail for the very first time using a direct wavefront measurement approach with a Shack-Hartmann wavefront sensor. A significant difference in dioptric power of the pump-induced lens was measured between non-lasing and lasing conditions, with the value under lasing conditions up to 60 % of the non-lasing value. Furthermore, the dioptric power under non-lasing conditions was found to be linearly proportional to the absorbed pump power, contrary to the expected non-linear proportionality due to the non-linear

heating factor that arises from excited state absorption at the pump wavelength. It was postulated that the measured dioptric power was due to the thermal lens in combination with a population lens which arose from an electronic refractive index distribution caused by the difference in polarizability of ions in the excited and ground states. It was shown qualitatively that the clamped inversion at threshold, and therefore the clamped population lens were in agreement to the weaker dioptric power under lasing conditions. Additional support to the hypothesis was made with a value of the polarizability difference similar to that measured for other Chromium-doped media. A time dependent population lens is also a likely mechanism for self-Q-switching observed here and by others.

Using the improved understating of the pump-induced lens dioptric power in end-pumped Alexandrite lasers, power-scaled Alexandrite lasers were demonstrated using a novel convex-plane cavity design. Using fibre-coupled diode-pumping, multi-watt Alexandrite lasers in TEM_{00} mode were demonstrated. Results include: a record slope efficiency of 54.9 %; >1 W over 730-805 nm and >4 W over 755-780 nm with <1 nm linewidth; 4.2 W dual-wavelength operation; 3.3 W with 1 GHz linewidth using the first VBG-locked Alexandrite laser; and a maximum output power of 8.6 W with excellent beam quality of $M^2 < 1.1$. Detailed cavity models and designs were presented that can be applied to other diode-pumped gain media.

Single-longitudinal-mode Alexandrite lasers were demonstrated using unidirectional ring laser designs. Two cavity designs were demonstrated showing SLM operation with >1 W of output power and TEM_{00} mode quality and with 727-792 nm of wavelength tuning. Power-scaled ring laser designs were also investigated with a maximum laser power of 5.1 W with 24 % optical efficiency and 35 % slope efficiency. This result provides a promising outlook at achieving multi-watt TEM_{00} and SLM performance from a tunable diode-pumped Alexandrite laser.

Over the last decade Alexandrite lasers have become a topical area of research owing to the development of red-diode-lasers. The work in this thesis has shown significant progress in the performance of diode-pumped Alexandrite lasers and that tunable Alexandrite lasers has re-emerged as a highly promising high-power near-infrared laser source for today.

Bibliography

[1] T. Maiman, "Stimulated Optical Radiation in Ruby", Nature **187**, 493–494 (1960).

[2] J. Hecht, "A short history of laser development", Appl. Opt. **49**, F99–F122 (2010).

[3] T. H. Maiman, R. H. Hoskins, I. J. D'Haenens, C. K. Asawa, and V. Evtuhov, "Stimulated Optical Emission in Fluorescent Solids. II. Spectroscopy and Stimulated Emission in Ruby", Phys. Rev. **123**, 1151–1157 (1961).

[4] W. F. Krupke and J. Zweiback, "High efficiency gallium nitride laser diode pumped CW ruby laser", in Solid state lasers xxix: technology and devices, Vol. 11259 (International Society for Optics and Photonics, 2020), pp. 298–302.

[5] W. Koechner, *Solid-State Laser Engineering*, 6th ed., Vol. 1 (Springer-Verlag, 2006).

[6] S. Wills, "The laser at 60", Opt. Photon. News **31**, 30–39 (2020).

[7] K. Dahl, P. Cebeci, O. Fitzau, M. Giesberts, C. Greve, M. Krutzik, A. Peters, S. A. Pyka, J. Sanjuan, M. Schiemangk, T. Schuldt, K. Voss, and A. Wicht, "A new laser technology for LISA", in International conference on space optics — icso 2018, Vol. 11180, edited by Z. Sodnik, N. Karafolas, and B. Cugny (International Society for Optics and Photonics, 2019), pp. 131–137.

[8] J. Pupeikis, P.-A. Chevreuil, N. Bigler, L. Gallmann, C. R. Phillips, and U. Keller, "Water window soft x-ray source enabled by a 25W few-cycle 2.2 µm OPCPA at 100kHz", Optica **7**, 168–171 (2020).

[9] C. Sirtori, "Terahertz race heats up", Nat. Photonics **15**, 1–2 (2021).

[10] D. C. Hanna, "Some thoughts on 38 years of lasing", Journal of Physics D: Applied Physics **34**, 2373–2380 (2001).

[11] J. Walling, O. Peterson, H. Jenssen, R. Morris, and E. O'Dell, "Tunable alexandrite lasers", IEEE Journal of Quantum Electronics **16**, 1302–1315 (1980).

[12] J. Walling, D. Heller, H. Samelson, D. Harter, J. Pete, and R. Morris, "Tunable alexandrite lasers: Development and performance", IEEE Journal of Quantum Electronics **21**, 1568–1581 (1985).

[13] X. Peng, A. Marrakchi, J. C. Walling, and D. F. Heller, "Watt-level red and UV output from a CW diode array-pumped tunable alexandrite laser", in Conference on lasers and electro-optics/quantum electronics and laser science and photonic applications systems technologies (2005), CMAA5.

[14] M. J. Damzen, "Diode-pumped Alexandrite laser: a bright prospect for future space Lidar missions", in, Vol. 8534 (International Society for Optics and Photonics, 2012), p. 81.

[15] M. J. Damzen, G. M. Thomas, A. Teppitaksak, and A. Minassian, "Progress in diode-pumped alexandrite lasers as a new resource for future space lidar missions", in International conference on space optics — icso 2014, Vol. 10563, edited by Z. Sodnik, B. Cugny, and N. Karafolas (International Society for Optics and Photonics, 2017), pp. 934–942.

[16] M. Strotkamp, A. Munk, B. Jungbluth, H.-D. Hoffmann, and J. Höffner, "Diode-pumped Alexandrite laser for next generation satellite-based earth observation lidar", CEAS Space J. **11**, 413–422 (2019).

[17] L. Lukoševičius, P. Wessels, S. Unland, S. Spiekermann, I. Balasa, S. Kramprich, L. Jensen, D. Kracht, J. Neumann, M. Lorrai, P. G. Lorrai, M. Hmidat, and J. Butkus, "Alexandrite laser crystal treatment and coatings for high LIDT space applications", in Laser-induced damage in optical materials 2020, Vol. 11514, edited by C. W. Carr, V. E. Gruzdev, D. Ristau, and C. S. Menoni (International Society for Optics and Photonics, 2020).

[18] M. P. A. Jones, L. G. Marcassa, and J. P. Shaffer, "Special Issue on Rydberg atom physics", Journal of Physics B: Atomic, Molecular and Optical Physics **50**, 060202 (2017).

[19] E. C. Cook, P. J. Martin, T. L. Brown-Heft, J. C. Garman, and D. A. Steck, "High passive-stability diode-laser design for use in atomic-physics experiments", Review of Scientific Instruments **83**, 043101 (2012).

[20] S. S. Sané, S. Bennetts, J. E. Debs, C. C. N. Kuhn, G. D. McDonald, P. A. Altin, J. D. Close, and N. P. Robins, "11W narrow linewidth laser source at 780nm for laser cooling and manipulation of Rubidium", Opt. Express **20**, 8915–8919 (2012).

[21] G. Huber, C. Kränkel, and K. Petermann, "Solid-state lasers: status and future [Invited]", J. Opt. Soc. Am. B **27**, B93–B105 (2010).

[22] K. Takeno, T. Ozeki, S. Moriwaki, and N. Mio, "100W, single-frequency operation of an injection-locked Nd:YAG laser", Opt. Lett. **30**, 2110–2112 (2005).

[23] M. Frede, R. Wilhelm, and D. Kracht, "250W end-pumped Nd:YAG laser with direct pumping into the upper laser level", Opt. Lett. **31**, 3618–3619 (2006).

[24] J. J. Kasinski, W. Hughes, D. DiBiase, P. Bournes, and R. Burnham, "One joule output from a diode-array-pumped Nd:YAG laser with side-pumped rod geometry", IEEE Journal of Quantum Electronics **28**, 977–985 (1992).

[25] G. T. Maker and A. I. Ferguson, "Frequency-modulation mode locking of a diode-pumped Nd:YAG laser", Opt. Lett. **14**, 788–790 (1989).

[26] T. J. Kane and R. L. Byer, "Monolithic, unidirectional single-mode Nd:YAG ring laser", Opt. Lett. **10**, 65–67 (1985).

[27] A. Giesen and J. Speiser, "Fifteen Years of Work on Thin-Disk Lasers: Results and Scaling Laws", IEEE Journal of Selected Topics in Quantum Electronics **13**, 598–609 (2007).

[28] P. F. Moulton, "Spectroscopic and laser characteristics of Ti:Al2O3", J. Opt. Soc. Am. B **3**, 125–133 (1986).

[29] R. Ell, U. Morgner, F. X. Kärtner, J. G. Fujimoto, E. P. Ippen, V. Scheuer, G. Angelow, T. Tschudi, M. J. Lederer, A. Boiko, and B. Luther-Davies, "Generation of 5-fs pulses and octave-spanning spectra directly from a ti:sapphire laser", Opt. Lett. **26**, 373–375 (2001).

[30] Y. Wei, H. Lu, P. Jin, and K. Peng, "Self-injection locked cw single-frequency tunable ti:sapphire laser", Opt. Express **25**, 21379–21387 (2017).

[31] M. N. Cizmeciyan, H. Cankaya, A. Kurt, and A. Sennaroglu, "Kerr-lens mode-locked femtosecond Cr2+:ZnSe laser at 2420 nm", Opt. Lett. **34**, 3056–3058 (2009).

[32] S. Vasilyev, I. Moskalev, M. Mirov, S. Mirov, and V. Gapontsev, "Multi-Watt mid-IR femtosecond polycrystalline Cr2+:ZnS and Cr2+:ZnSe laser amplifiers with the spectrum spanning 2.0-2.6µm", Opt. Express **24**, 1616–1623 (2016).

[33] I. Moskalev, S. Mirov, M. Mirov, S. Vasilyev, V. Smolski, A. Zakrevskiy, and V. Gapontsev, "140W Cr:ZnSe laser system", Opt. Express **24**, 21090–21104 (2016).

[34] D. W. Hughes and J. R. M. Barr, "Laser diode pumped solid state lasers", Journal of Physics D: Applied Physics **25**, 563–586 (1992).

[35] W. A. Clarkson, R. Koch, and D. C. Hanna, "Room-temperature diode-bar-pumped Nd:YAG laser at 946 nm", Opt. Lett. **21**, 737–739 (1996).

[36] A. Siegman, *Lasers* (University Science Books, 1986).

[37] O. Svelto, *Principles of Lasers*, 5th ed. (Springer, 2010).

[38] Y. Shen, X. Wang, Z. Xie, C. Min, X. Fu, Q. Liu, M. Gong, and X. Yuan, "Optical vortices 30 years on: OAM manipulation from topological charge to multiple singularities", Light: Sci. Appl. **8**, 90 (2019).

[39] L. Sun, Y. Guo, C. Shao, Y. Li, Y. Zheng, C. Sun, X. Wang, and L. Huang, "10.8kW, 2.6 times diffraction limited laser based on a continuous wave Nd:YAG oscillator and an extra-cavity adaptive optics system", Opt. Lett. **43**, 4160–4163 (2018).

[40] Y. Guo, Q. Peng, Y. Bo, Z. Chen, Y. Li, L. Zhang, C. Shao, L. Yuan, B. Wang, J. Xu, J. Xu, H. Gao, Y. Xu, B. Lai, C. Su, S. Ma, and T. Cheng, "24.6kW near diffraction limit quasi-continuous-wave Nd:YAG slab laser based on a stable–unstable hybrid cavity", Opt. Lett. **45**, 1136–1139 (2020).

[41] V. Magni, "Resonators for solid-state lasers with large-volume fundamental mode and high alignment stability", Appl. Opt. **25**, 107–117 (1986).

[42] J. J. Zayhowski and A. Mooradian, "Single-frequency microchip Nd lasers", Opt. Lett. **14**, 24–26 (1989).

[43] T. Taira, A. Mukai, Y. Nozawa, and T. Kobayashi, "Single-mode oscillation of laser-diode-pumped Nd:YVO4 microchip lasers", Opt. Lett. **16**, 1955–1957 (1991).

[44] V. Evtuhov and A. E. Siegman, "A "Twisted-Mode" Technique for Obtaining Axially Uniform Energy Density in a Laser Cavity", Appl. Opt. **4**, 142–143 (1965).

[45] W. A. Clarkson, A. B. Neilson, and D. C. Hanna, "Unidirectional operation of ring lasers via the acoustooptic effect", IEEE Journal of Quantum Electronics **32**, 311–325 (1996).

[46] U. Demirbas, "Off-surface optic axis birefringent filters for smooth tuning of broadband lasers", Appl. Opt. **56**, 7815–7825 (2017).

[47] E. Beyatli and U. Demirbas, "Widely tunable dual-wavelength operation of Tm:YLF, Tm:LuAG, and Tm:YAG lasers using off-surface optic axis birefringent filters", Appl. Opt. **57**, 6679–6686 (2018).

[48] C. Kränkel, D.-T. Marzahl, F. Moglia, G. Huber, and P. W. Metz, "Out of the blue: semiconductor laser pumped visible rare-earth doped lasers", Laser & Photonics Reviews **10**, 548–568 (2016).

[49] N. Nagl, S. Gröbmeyer, V. Pervak, F. Krausz, O. Pronin, and K. F. Mak, "Directly diode-pumped, Kerr-lens mode-locked, few-cycle Cr:ZnSe oscillator", Opt. Express **27**, 24445–24454 (2019).

[50] J. C. Walling, H. P. Jenssen, R. C. Morris, E. W. O'Dell, and O. G. Peterson, "Tunable-laser performance in BeAl2O4:Cr3+", Opt. Lett. **4**, 182–183 (1979).

[51] J. W. Kuper, T. Chin, and H. E. Aschoff, "Extended Tuning Range of Alexandrite at Elevated Temperatures", in Advanced solid state lasers (1990), p. CL3.

[52] V. N. Lisitsyn, V. N. Matrosov, V. P. Orekhova, E. V. Pestryakov, B. K. Sevast'yanov, V. I. Trunov, V. N. Zenin, and Y. L. Remigaĭlo, "Generation of 0.7-0.8μm picosecond pulses in an alexandrite laser with passive mode locking", Sov. J. Quantum Electron **12**, 368–370 (1982).

[53] S. Imai, T. Yamada, Y. Fujimori, and K. Ishikawa, "Third-harmonic generation of an alexandrite laser in β-BaB2O4", Applied Physics Letters **54**, 1206–1208 (1989).

[54] S. T. Lai and M. L. Shand, "High efficiency cw laser-pumped tunable alexandrite laser", Journal of Applied Physics **54**, 5642–5644 (1983).

[55] R. Scheps, B. M. Gately, J. F. Myers, J. S. Krasinski, and D. F. Heller, "Alexandrite laser pumped by semiconductor lasers", Applied Physics Letters **56**, 2288–2290 (1990).

[56] R. Scheps, J. F. Myers, T. R. Glesne, and H. B. Serreze, "Monochromatic end-pumped operation of an alexandrite laser", Optics Communications **97**, 363–366 (1993).

[57] J. W. Kuper and D. C. Brown, "High-efficiency CW green-pumped alexandrite lasers", in Solid state lasers xv: technology and devices, Vol. 6100, edited by H. J. Hoffman and R. K. Shori (International Society for Optics and Photonics, 2006), pp. 208–215.

[58] M. Fibrich, J. Šulc, and H. Jelínková, "Alexandrite microchip lasers", Opt. Express **27**, 16975–16982 (2019).

[59] P. Pichon, A. Barbet, J.-P. Blanchot, F. Druon, F. Balembois, and P. Georges, "LED-pumped alexandrite laser oscillator and amplifier", Opt. Lett. **42**, 4191–4194 (2017).

[60] M. Lando, Y. Shimony, R. M. Benmair, D. Abramovich, V. Krupkin, and A. Yogev, "Visible solar-pumped lasers", Optical Materials **13**, 111–115 (1999).

[61] V. Wulfmeyer and J. Bösenberg, "Single-mode operation of an injection-seeded alexandrite ring laser for application in water-vapor and temperature differential absorption lidar", Opt. Lett. **21**, 1150–1152 (1996).

[62] U. von Zahn and J. Höffner, "Mesopause temperature profiling by potassium lidar", Geophysical Research Letters **23**, 141–144 (1996).

[63] P. Gurnani, N. Williams, G. AL-Hetheli, O. Chukwuma, R. Roth, F. Fajardo, and K. Nouri, "Comparing the efficacy and safety of laser treatments in tattoo removal: a systematic review", Journal of the American Academy of Dermatology (2020).

[64] P. Crump, J. Wang, S. Patterson, D. Wise, A. Basauri, M. DeFranza, S. Elim, W. Dong, S. Zhang, M. Bougher, J. Patterson, S. Das, M. Grimshaw, J. Farmer, M. DeVito, and R. Martinsen, "Diode laser efficiency increases enable >400-W peak power from 1-cm bars and show a clear path to peak powers in excess of 1-kW", in High-power diode laser technology and applications iv, Vol. 6104, edited by M. S. Zediker (International Society for Optics and Photonics, 2006), pp. 77–86.

[65] I. Yorulmaz, E. Beyatli, A. Kurt, A. Sennaroglu, and U. Demirbas, "Efficient and low-threshold Alexandrite laser pumped by a single-mode diode", Opt. Mater. Express **4**, 776–789 (2014).

[66] A. Teppitaksak, A. Minassian, G. M. Thomas, and M. J. Damzen, "High efficiency >26 W diode end-pumped Alexandrite laser", Opt. Express **22**, 16386–16392 (2014).

[67] G. M. Thomas, A. Minassian, X. Sheng, and M. J. Damzen, "Diode-pumped Alexandrite lasers in Q-switched and cavity-dumped Q-switched operation", Opt. Express **24**, 27212–27224 (2016).

[68] U. Parali, X. Sheng, A. Minassian, G. Tawy, J. Sathian, G. M. Thomas, and M. J. Damzen, "Diode-pumped Alexandrite laser with passive SESAM Q-switching and wavelength tunability", Optics Communications **410**, 970–976 (2018).

[69] A. Munk, B. Jungbluth, M. Strotkamp, H.-D. Hoffmann, R. Poprawe, J. Höffner, and F.-J. Lübken, "Diode-pumped alexandrite ring laser in single-longitudinal mode operation for atmospheric lidar measurements", Opt. Express **26**, 14928–14935 (2018).

[70] S. Ghanbari, R. Akbari, and A. Major, "Femtosecond Kerr-lens mode-locked Alexandrite laser", Opt. Express **24**, 14836–14840 (2016).

[71] S. Ghanbari, K. A. Fedorova, A. B. Krysa, E. U. Rafailov, and A. Major, "Femtosecond Alexandrite laser passively mode-locked by an InP/InGaP quantum-dot saturable absorber", Opt. Lett. **43**, 232–234 (2018).

[72] C. Cihan, A. Muti, I. Baylam, A. Kocabas, U. Demirbas, and A. Sennaroglu, "70 femtosecond Kerr-lens mode-locked multipass-cavity Alexandrite laser", Opt. Lett. **43**, 1315–1318 (2018).

[73] C. Cihan, C. Kocabas, U. Demirbas, and A. Sennaroglu, "Graphene mode-locked femtosecond Alexandrite laser", Opt. Lett. **43**, 3969–3972 (2018).

[74] E. F. Farell, J. H. Fang, and R. E. Newnham, "Refinement of the Chrysoberyl Structure", The American Mineralogist **48**, 804–810 (1963).

[75] C. E. Forbes, "Analysis of the spin-Hamiltonian parameters for Cr3+ in mirror and inversion symmetry sites of alexandrite (Al2xCrxBeO4). Determination of the relative site occupancy by EPR", The Journal of Chemical Physics **79**, 2590–2599 (1983).

[76] U. Demirbas and F. X. Kärtner, "Alexandrite: an attractive thin-disk laser material alternative to Yb:YAG?", J. Opt. Soc. Am. B **37**, 459–472 (2020).

[77] E. Anashkina and O. Antipov, "Electronic (population) lensing versus thermal lensing in Yb:YAG and Nd:YAG laser rods and disks", J. Opt. Soc. Am. B **27**, 363–369 (2010).

[78] P. Cheo, ed., *Handbook of Solid-State Lasers*, no. 18 in Optical Science and Engineering (CRC Press, 1988).

[79] S. A. Payne, L. K. Smith, R. J. Beach, B. H. T. Chai, J. H. Tassano, L. D. DeLoach, W. L. Kway, R. W. Solarz, and W. F. Krupke, "Properties of Cr:LiSrAlF6 crystals for laser operation", Appl. Opt. **33**, 5526–5536 (1994).

[80] T. Südmeyer, C. Kränkel, C. R. E. Baer, O. H. Heckl, C. J. Saraceno, M. Golling, R. Peters, K. Petermann, G. Huber, and U. Keller, "High-power ultrafast thin disk laser oscillators and their potential for sub-100-femtosecond pulse generation", Appl. Phys. B **97**, 281–295 (2009).

[81] A. Steimacher, O. A. Sakai, A. C. Bento, M. L. Baesso, A. N. Medina, S. M. Lima, and T. Catunda, "Angular dependence of the thermal-lens effect on LiSrAlF6 and LiSrGaF6 single crystals", Opt. Lett. **33**, 1720–1722 (2008).

[82] P. Loiko, S. Ghanbari, V. Matrosov, K. Yumashev, and A. Major, "Dispersion and anisotropy of thermo-optical properties of Alexandrite laser crystal", Opt. Mater. Express **8**, 3000–3006 (2018).

[83] R. D. Peterson, A. T. Pham, H. P. Jenssen, A. Cassanho, and V. Castillo, "Thermo-Optical Comparison of LiSAF, LiCAF, and LiSGaF", in Advanced solid state lasers (1999), TuB6.

[84] P. Loiko and A. Major, "Dispersive properties of alexandrite and beryllium hexaaluminate crystals", Opt. Mater. Express **6**, 2177–2183 (2016).

[85] U. Demirbas, "Cr:Colquiriite Lasers: Current status and challenges for further progress", Progress in Quantum Electronics **68**, 100227 (2019).

[86] V. Pilla, P. R. Impinnisi, and T. Catunda, "Measurement of saturation intensities in ion doped solids by transient nonlinear refraction", Applied Physics Letters **70**, 817–819 (1997).

[87] N. Passilly, E. Haouas, V. Ménard, R. Moncorgé, and K. Aı¨t-Ameur, "Population lensing effect in Cr:LiSAF probed by Z-scan technique", Optics Communications **260**, 703–707 (2006).

[88] P. F. Moulton, J. G. Cederberg, K. T. Stevens, G. Foundos, M. Koselja, and J. Preclikova, "Optimized InGaN-diode pumping of Ti:sapphire crystals", Opt. Mater. Express **9**, 2131–2146 (2019).

[89] M. Born and E. Wolf, *Principles of Optics*, 6th ed. (Pergamon Press, 1980).

[90] W. R. Kerridge-Johns and M. J. Damzen, "Temperature effects on tunable cw Alexandrite lasers under diode end-pumping", Opt. Express **26**, 7771–7785 (2018).

[91] Z. Zhang, K. T. V. Grattan, and A. W. Palmer, "Thermal characteristics of alexandrite fluorescence decay at high temperatures, induced by a visible laser diode emission", Journal of Applied Physics **73**, 3493–3498 (1993).

[92] G. V. Bukin, S. Y. Volkov, V. N. Matrosov, B. K. Sevast'yanov, and M. I. Timoshechkin, "Stimulated emission from alexandrite (BeAl2O4:Cr3+)", Sov. J. Quantum Electron. **8**, 671–672 (1978).

[93] R. C. Powell, L. Xi, X. Gang, G. J. Quarles, and J. C. Walling, "Spectroscopic properties of alexandrite crystals", Phys. Rev. B **32**, 2788–2797 (1985).

[94] D. E. McCumber, "Theory of Phonon-Terminated Optical Masers", Phys. Rev. **134**, 299–306 (1964).

[95] M. Fibrich, J. Šulc, D. Vyhlídal, H. Jelínková, and M. Čech, "Alexandrite spectroscopic and laser characteristic investigation within a 78–400K temperature range", Laser Physics **27**, 115801 (2017).

[96] E. Beyatli, I. Baali, B. Sumpf, G. Erbert, A. Leitenstorfer, A. Sennaroglu, and U. Demirbas, "Tapered diode-pumped continuous-wave alexandrite laser", J. Opt. Soc. Am. B **30**, 3184–3192 (2013).

[97] B. Sevast'yanov, "Excited-state absorption spectroscopy of crystals doped with Cr3+, Ti3+, and Nd3+ ions. Review.", Crystallogr. Rep. **48**, 989–1011 (2003).

[98] M. L. Shand, J. C. Walling, and R. C. Morris, "Excited-state absorption in the pump region of alexandrite", Journal of Applied Physics **52**, 953–955 (1981).

[99] W. R. Kerridge-Johns and M. J. Damzen, "Analysis of pump excited state absorption and its impact on laser efficiency", Laser Physics Letters **12**, 125002 (2015).

[100] M. Shand and H. Jenssen, "Temperature dependence of the excited- state absorption of alexandrite", IEEE Journal of Quantum Electronics **19**, 480–484 (1983).

[101] M. Shand and J. Walling, "Excited-state absorption in the lasing wavelength region of alexandrite", IEEE Journal of Quantum Electronics **18**, 1152–1155 (1982).

[102] E. A. Arbabzadah and M. J. Damzen, "Fibre-coupled red diode-pumped Alexandrite TEM00 laser with single and double-pass end-pumping", Laser Physics Letters **13**, 065002 (2016).

[103] Shirin Ghanbari and Arkady Major, "High power continuous-wave dual-wavelength alexandrite laser", Laser Physics Letters **14**, 105001 (2017).

[104] G. Tawy and M. J. Damzen, "Tunable, dual wavelength and self-Q-switched Alexandrite laser using crystal birefringence control", Opt. Express **27**, 17507–17520 (2019).

[105] G. Tawy and M. J. Damzen, "Narrow linewidth tunable and dual wavelength compact Alexandrite laser", in Solid state lasers XXIX: technology and devices, Vol. 11259 (International Society for Optics and Photonics, 2020), 112590J.

[106] W. A. Clarkson, "Thermal effects and their mitigation in end-pumped solid-state lasers", Journal of Physics D: Applied Physics **34**, 2381–2395 (2001).

[107] M. E. Innocenzi, H. T. Yura, C. L. Fincher, and R. A. Fields, "Thermal modeling of continuous-wave end-pumped solid-state lasers", Applied Physics Letters **56**, 1831–1833 (1990).

[108] S. Chenais, F. Druon, S. Forget, F. Balembois, and P. Georges, "On thermal effects in solid-state lasers: The case of ytterbium-doped materials", Progress in Quantum Electronics **30**, 89–153 (2006).

[109] D. C. Burnham, "Simple Measurement of Thermal Lensing Effects in Laser Rods", Appl. Opt. **9**, 1727–1728 (1970).

[110] B. Neuenschwander, R. Weber, and H. P. Weber, "Determination of the thermal lens in solid-state lasers with stable cavities", IEEE Journal of Quantum Electronics **31**, 1082–1087 (1995).

[111] S. Chenais, F. Balembois, F. Druon, G. Lucas-Leclin, and P. Georges, "Thermal lensing in diode-pumped ytterbium Lasers-Part II: evaluation of quantum efficiencies and thermo-optic coefficients", IEEE Journal of Quantum Electronics **40**, 1235–1243 (2004).

[112] G. Tawy, J. Wang, and M. J. Damzen, "Pump-induced lensing effects in diode pumped Alexandrite lasers", Opt. Express **27**, 35865–35883 (2019).

[113] W. A. Clarkson, N. S. Felgate, and D. C. Hanna, "Simple method for reducing the depolarization loss resulting from thermally induced birefringence in solid-state lasers", Opt. Lett. **24**, 820–822 (1999).

[114] T. Godin, R. Moncorgé, J.-L. Doualan, M. Fromager, K. Ait-Ameur, R. A. Cruz, and T. Catunda, "Optically pump-induced athermal and nonresonant refractive index changes in the reference Cr-doped laser materials: Cr:GSGG and ruby", J. Opt. Soc. Am. B **29**, 1055–1064 (2012).

[115] E. Beyatli, A. Sennaroglu, and U. Demirbas, "Self-Q-switched Cr:LiCAF laser", J. Opt. Soc. Am. B **30**, 914–921 (2013).

[116] O. L. Antipov, D. V. Bredikhin, O. N. Eremeykin, A. P. Savikin, E. V. Ivakin, and A. V. Sukhadolau, "Electronic mechanism for refractive-index changes in intensively pumped Yb:YAG laser crystals", Opt. Lett. **31**, 763–765 (2006).

[117] S. Chenais, F. Balembois, F. Druon, G. Lucas-Leclin, and P. Georges, "Thermal lensing in diode-pumped ytterbium Lasers-Part I: theoretical analysis and wavefront measurements", IEEE Journal of Quantum Electronics **40**, 1217–1234 (2004).

[118] M. J. Damzen, G. M. Thomas, and A. Minassian, "Diode-side-pumped Alexandrite slab lasers", Opt. Express **25**, 11622–11636 (2017).

[119] W. Kerridge-Johns, *Diode-pumped alexandrite laser development and vortex mode generation* (PhD Thesis, Imperial College London, 2018).

[120] A. Coney, *Development of diode-pumped alexandrite laser systems for atmosheperic remote sensing* (PhD Thesis, Imperial College London, 2019).

[121] G. Tawy, A. Minassian, and M. J. Damzen, "High-power 7.4W TEM00 and wavelength-tunable alexandrite laser with a novel cavity design and efficient fibre-coupled diode-pumping", OSA Continuum **3**, 1638–1649 (2020).

[122] J.-H. Wolter, M. A. Ahmed, and T. Graf, "Thin-disk laser operation of Ti:sapphire", Opt. Lett. **42**, 1624–1627 (2017).

[123] J.-H. Wolter, R. Balmer, S. Ricaud, M. Antier, C. Simon-Boisson, T. Graf, and M. A. Ahmed, "Ti:sapphire thin-disk laser symmetrically cooled by curved single crystal diamond heat spreaders", Laser Physics Letters **17**, 015802 (2019).

[124] U. Demirbas, "Power scaling potential of continuous-wave Cr:LiSAF and Cr:LiCAF lasers in thin-disk geometry", Appl. Opt. **57**, 10207–10217 (2018).

[125] R. Chesler and D. Maydan, "Convex-Concave Resonators for TEM_{00} Operation of Solid-State Ion Lasers", Journal of Applied Physics **43**, 2254–2257 (1972).

[126] L. McDonagh and R. Wallenstein, "Low-noise 62 W CW intracavity-doubled TEM_{00} Nd:YVO_4 green laser pumped at 888 nm", Opt. Lett. **32**, 802–804 (2007).

[127] P. H. Tuan, C. C. Chang, C. Y. Lee, C. Y. Cho, H. C. Liang, and Y. F. Chen, "Exploiting concave-convex linear resonators to design end-pumped solid-state lasers with flexible cavity lengths: Application for exploring the self-mode-locked operation", Opt. Express **24**, 26024–26034 (2016).

[128] T. Chung, A. Rapaport, V. Smirnov, L. B. Glebov, M. C. Richardson, and M. Bass, "Solid-state laser spectral narrowing using a volumetric photothermal refractive Bragg grating cavity mirror", Opt. Lett. **31**, 229–231 (2006).

[129] M. Hemmer, Y. Joly, L. Glebov, M. Bass, and M. Richardson, "Sub-5-pm linewidth, 130-nm-tuning of a coupled-cavity Ti:sapphire oscillator via volume Bragg grating-based feedback", Applied Physics B **106**, 803–807 (2012).

[130] K. Seger, N. Meiser, C. Canalias, V. Pasiskevicius, and F. Laurell, "Tunable, passively Q-switched single-longitudinal-mode Nd:YVO_4 laser using a chirped volume Bragg grating", Applied Physics B **109**, 99–103 (2012).

[131] W. R. Kerridge-Johns and M. J. Damzen, "Analytical model of tunable Alexandrite lasing under diode end-pumping with experimental comparison", J. Opt. Soc. Am. B **33**, 2525–2534 (2016).

[132] M. Walochnik, B. Jungbluth, H. Huber, J. Ammersbach, A. Munk, M. Strotkamp, M. Traub, D. Hoffmann, and R. Poprawe, "Diode-pumped cw Alexandrite laser with temporally stable 6.5W in TEM_{00} operation with prospect of power scaling", Opt. Express **28**, 15761–15769 (2020).

[133] G. Chen, C. Zhenhua, L. Zhaojun, Z. Xingyu, W. Shiwu, N. Yi, and Z. Zhigang, "10.5W Laser Output at 760nm From LD Pumped Alexandrite Crystal", Chinese Journal of Lasers **47**, 1015001 (2020).

[134] J. C. E. Coyle, J.-M. Hopkins, A. A. Lagatsky, and A. J. Kemp, "Titanium sapphire: a decade of diode-laser pumping", in 2019 Conference on Lasers and Electro-Optics Europe and European Quantum Electronics Conference, OSA Technical Digest (Optical Society of America, 2019), paper ca_7_1.

[135] S. Backus, M. Kirchner, R. Lemons, D. Schmidt, C. Durfee, M. Murnane, and H. Kapteyn, "Direct diode pumped Ti:sapphire ultrafast regenerative amplifier system", Opt. Express **25**, 3666–3674 (2017).

[136] Z. Miao, H. Yu, J. Zhang, S. Zou, P. Zhao, B. Lou, and X. Lin, "Watt-Level CW Ti: Sapphire Oscillator Directly Pumped With Green Laser Diodes Module", IEEE Photonics Technology Letters **32**, 247–250 (2020).

[137] Y. Wang, Y. Zhao, Z. Pan, J. E. Bae, S. Y. Choi, F. Rotermund, P. Loiko, J. M. Serres, X. Mateos, H. Yu, H. Zhang, M. Mero, U. Griebner, and V. Petrov, "78fs SWCNT-SA mode-locked Tm:CLNGG disordered garnet crystal laser at 2017nm", Opt. Lett. **43**, 4268–4271 (2018).

[138] Y. Zhao, W. Chen, L. Wang, Y. Wang, Z. Pan, X. Dai, H. Yuan, H. Cai, Y. Zhang, J. E. Bae, T. G. Park, F. Rotermund, P. Loiko, J. M. Serres, X. Mateos, D. Shen, U. Griebner, and V. Petrov, "Graphene mode-locked Tm,Ho-codoped crystalline garnet laser producing 70-fs pulses near 2.1µm", OSA Continuum **2**, 2593–2600 (2019).

[139] H. Tanaka, S. Fujita, and F. Kannari, "High-power visibly emitting Pr3+:YLF laser end pumped by single-emitter or fiber-coupled GaN blue laser diodes", Appl. Opt. **57**, 5923–5928 (2018).

[140] A. Munk, M. Strotkamp, M. Walochnik, B. Jungbluth, M. Traub, H.-D. Hoffmann, R. Poprawe, J. Höffner, and F.-J. Lübken, "Diode-pumped Q-switched Alexandrite laser in single longitudinal mode operation with Watt-level output power", Opt. Lett. **43**, 5492–5495 (2018).

[141] X. Sheng, G. Tawy, J. Sathian, A. Minassian, and M. J. Damzen, "Unidirectional single-frequency operation of a continuous-wave Alexandrite ring laser with wavelength tunability", Opt. Express **26**, 31129–31136 (2018).

[142] J. Sathian, G. Tawy, X. Sheng, A. Minassian, and M. J. Damzen, "Nonastigmatic alexandrite ring laser design with wavelength-tunable single-longitudinal-mode operation", J. Opt. Soc. Am. B **37**, 2185–2192 (2020).

[143] SolsTiS Datasheet, [https://www.m2lasers.com/solstis-details.html?file=SolsTiS-datasheet.pdf] (Accessed: February 2021).

[144] H. Kogelnik, E. Ippen, A. Dienes, and C. Shank, "Astigmatically compensated cavities for CW dye lasers", IEEE Journal of Quantum Electronics **8**, 373–379 (1972).

Appendices

Appendix A

Laser Diagnostics

A.1 Power

The laser power was measured using various power meters depending on the power range of the laser. Table A.1 shows an overview of the power meters used.

Table A.1: Overview of different power meters used.

Make & Model	Power Range	Resolution	Detector Type
Thorlabs PM160	10 nW-2 mW	100 pW	Si Photodiode
Thorlabs PM16-401	10 µW-1 W	1 µW	Thermopile
Coherent LM45	0.1-45 W	0.1 W	Thermopile
Coherent PM300F-50	0.1-300 W	0.1 W	Thermopile

A.2 Beam Quality

The laser beam quality was measured using CINOGY's beam profiler with the beam profiling software RayCi according to ISO Standard 11146, as depicted in Fig. A.1. An overview of the camera's properties is shown in Table A.2. The camera was also used to measure the laser mode size via the $4f$-imaging technique and in measuring the laser linewidth (A.4).

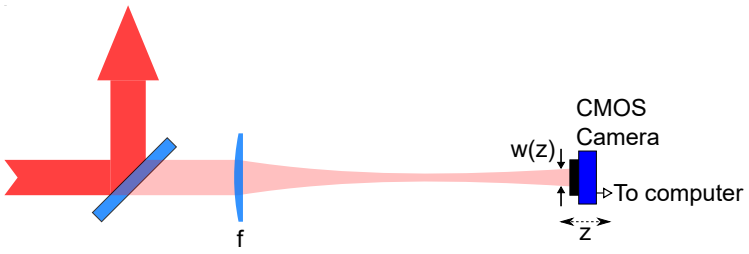

Figure A.1: Setup for beam quality measurement. The CINOGY CMOS 1202 camera is used together with the RayCi software. M^2 value is computed by inputting position z and wavelength λ.

Table A.2: Properties of CINOGY CMOS-1202.

Spectral Response	400-1320 nm
Number of pixels	1.3MPixel
Pixel size	$5.3 \times 5.3\,\mu$m

A.3 Wavelength

Two fibre-coupled grating spectrometers were used to measure the laser wavelength. These were typically used by placing the fibre end near a power meter so as to pick up a small amount of the beam via scatter. Table A.3 gives an overview of the properties of the two spectrometers.

Table A.3: Overview of different spectrometers used.

Make & Model	Wavelength Range	Resolution
Thorlabs CCS175/M	500-1000 nm	< 0.6 nm
Lasertack LR2H	733-797 nm	< 0.1 nm

A.4 Laser Linewidth

For assessing the number of longitudinal modes and measuring the laser linewidth when limited by the spectral resolution of the grating spectrometer ($\lesssim 0.1$ nm), a Fabry-Perot (FP) interferometer in combination with the CMOS camera was used.

Figure A.2 shows the experimental measurement technique for measuring the laser linewidth and assessing the number of lasing longitudinal modes. The FP

interferometer is formed of two partially reflective surfaces separated by a thickness L. The transmission of the FP interferometer depends on the angle of incidence θ and is maximum when $2\pi\nu L\cos\theta/c = m\pi$, where m is an integer, and the highest order fringe is when $m' = 2L\nu/c$.

A diverging lens is used to provide a range of angles θ and a focusing lens is placed after the FP interferometer to reveal the interference pattern as concentric rings separated by the FSR of the interferometer which is given by $\text{FSR} = c/2L\cos\theta$. A high resolution can be obtained provided the finesse, $\mathfrak{F} = \pi\sqrt{R}/(1-R)$, is high, which can be obtained with a high reflectivity and allows frequency components at an order of magnitude less than the FSR to be resolved.

Since $\theta^2 \propto m' - m$ for small angles, the radial distance squared can be calibrated to the frequency scale knowing the FSR of the FP interferometer, as shown in Fig. A.3, which shows how the square of the cross section gives the laser linewidth using the CMOS camera. When viewing the interference pattern, single-longitudinal-mode operation can be verified by observing single fringes separated by the FSR.

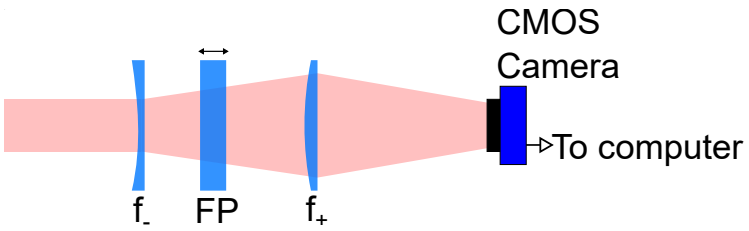

Figure A.2: Setup for resolving longitudinal mode pattern and calculating laser linewidth using a Fabry-Peror interferometer.

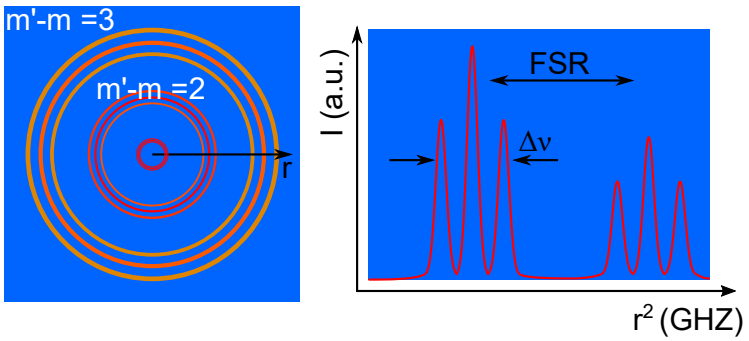

Figure A.3: Typical image on CMOS camera of concentric ring interference pattern and cross section of r^2 enabling laser linewdith measurement. Here three longitudinal modes are present.

Appendix B

Population Lens Dioptric Power Derivation

The dioptric power of the population lens due to the change in wavefront caused by the spatial variation in refractive index (Eq. (5.16) in Chapter 5) is given by

$$D_P = \frac{2}{r^2} C \left(F\left(0\right) - F\left(r\right) \right). \tag{B.1}$$

The radial form of the integrated inversion factor (using Eq. (5.9) in Chapter 5) is given by

$$F\left(r\right) \approx \frac{1}{\sigma_0 N} \left[\frac{I\left(r\right)}{I_s} - \frac{\gamma}{2} \left(\frac{I\left(r\right)}{I_s} \right)^2 \right]. \tag{B.2}$$

For a Gaussian pump profile $I(r) = (2P_0/\pi w_p^2) \exp(-2r^2/w_p^2)$ with $P_s = I_s(\pi w_p^2/2)$ Eq. (B.2) can be written as

$$F\left(r\right) = \frac{\gamma}{\sigma_1 N} \left[\frac{P_0}{P_s} e^{-2r^2/w_p^2} - \frac{\gamma}{2} \left(\frac{P_0}{P_s} e^{-2r^2/w_p^2} \right)^2 \right]. \tag{B.3}$$

Approximating $\exp(-2r^2/w_p^2) \approx 1 - 2r^2/w_p^2$ and $\exp(-4r^4/w_p^4) \approx 1 - 4r^2/w_p^2$ then

$$F\left(0\right) = \frac{1}{\sigma_0 N} \left[\left(\frac{P_0}{P_s} - \frac{\gamma}{2} \left(\frac{P_0}{P_s} \right)^2 \right) \right], \tag{B.4}$$

$$F(r) = \frac{1}{\sigma_0 N}\left[\left(\frac{P_0}{P_s} - \frac{\gamma}{2}\left(\frac{P_0}{P_s}\right)^2\right) - \frac{2r^2}{w_p^2}\left(\frac{P_0}{P_s}\gamma\left(\frac{P_0}{P_s}\right)^2\right)\right]. \tag{B.5}$$

Substituting Eqs. (B.4) and (B.5) into Eq. (B.2) gives the population lens dioptric power in terms of the absorbed pump power (to second order) assuming $P_0 = P_{abs}$

$$D_P = \frac{4C}{\alpha_0 w_p^2}\left[\frac{P_{abs}}{P_s} - \gamma\left(\frac{P_{abs}^2}{P_s}\right)^2\right]. \tag{B.6}$$